ALMA MATER STUDIORUM · UNIVERSITÀ DI BOLOGNA

School of Science
Department of Physics and Astronomy
Master Degree in Astrophysics and Cosmology

Simulations and experimental tests of the X/Gamma-ray Imaging Spectrometer for THESEUS and other mission opportunities

Presented by:
Giulia Mattioli

Supervisor:
Prof. Cristian Vignali

Co-supervisor:
Dr. Enrico Virgilli
Dr. Lorenzo Amati
Dr. Claudio Labanti

Academic year 2022 / 2023

Contents

Abstract

Gamma-Ray Bursts (GRBs) are short, energetic bursts of γ-rays and are the manifestation of the most violent explosions in the Universe. Although they were first discovered over half a century ago, many questions about them still need to be addressed. Since the successful launch of GRB dedicated missions such as *Swift* and *Fermi*, multi-wavelength ground-based observations have provided a new approach to better characterize these events and their host galaxies, and understand the physics behind GRBs. Because of their brightness, GRBs are unique and irreplaceable tools for investigating the Early Universe and for advancing Multi-Messenger Astrophysics. It is then crucial to study all classes of GRBs in a broad energy range band.

Several experiments and space missions have been proposed and finalized worldwide in the past 50 years in order to study such energetic events.

The Transient High-Energy Sky and Early Universe Surveyor (THESEUS) has been proposed in recent years not only to shed light on these still misterious explosions, but also to fully exploiting their potential as cosmic probes. THESEUS is a space mission developed in response to the calls for M-class missions by the European Space Agency (ESA). The study of the mission has been conducted by the ESA study Team and the THESEUS consortium, an entity comprising several ESA members, and primarily Italy, which has a leading role, including the PI-ship of the project. The high level of scientific advancement that this space mission can bring places THESEUS as a competitive candidate. This is demonstrated by the fact that it was selected in the M5 ESA call, completing a 3 year Phase A assessment study. Even if it was not selected as final mission for M5, it was selected again for the ESA M7 call, starting a new Phase A in 2023.

The THESEUS payload is composed by two GRB monitors and a telescope, respectively the Soft X-ray Imager (SXI), the X/Gamma-ray Imaging Spectrometer (XGIS) and the InfraRed Telescope (IRT).

The combination of these instruments allows to fully exploit GRBs for investigating the Early Universe and advancing Multi-Messenger Astrophysics from identification of electromagnetic (IR/Optical/X-ray) counterparts of gravitational wave events, thus providing a fundamental synergy with the next-generation of gravita-

tional wave detectors. This will be achieved through a step change in capability of detection and characterisation of GRBs, exploiting an unprecedented wide energy band (0.3 keV - 10 MeV) and a wide Field of View size.

In this Thesis, particular attention was put on XGIS and on the scientific and technological requirements that it should fulfill in order to be suitable for the THESEUS science case. The detection plane of XGIS is composed by an hybrid Si/CsI(Tl) detector, coupled to advanced and specific electronics. XGIS detection array is made by 8×8 elements (two Silicon Drift Detectors and a CsI(Tl) scintillator bar in between); for electronic and functional tests, also smaller arrays can be adopted, due to the modularity of the plane. Therefore, the study and optimization of an XGIS prototype (detection array of 2×2) has been carried out, focusing on the requirements concerning the science data production, the full scale energy range and the energy resolution. Functional, performance and environmental tests have been conducted on the prototype through both radioactive sources and synthetic electric signals, in order to characterize experimentally the read-out electronics (ORION) specifically developed for the XGIS detector.

In the first Chapter of this Thesis, the fundamental properties in the GRB prompt and afterglow phases and the most promising progenitor models for GRBs are introduced. In Chapter 2, the THESEUS mission is described, with special focus on the instruments onboard and, in particular, on the XGIS instrument, which is being developed within the Italian participation in the THESEUS Consortium. In Chapter 3, the characterization activity performed for the XGIS instrument is described.

Due to its compact and flexible design and its unprecedented energy pass-band, XGIS is an ideal tool which could be also adopted for other mission opportunities, with different instrument configuration and size, based on the size of the mission and thus on the budget. An exploratory simulation has been developed to evaluate the performance of an alternative experiment based on the same instrument concept as XGIS. This study has been reported in Chapter 4 of this Thesis. We have called this instrument *alternative-XGIS* (aXGIS) and have evaluated its GRB detection capabilities. These preliminary results have been obtained by developing a localization algorithm for the triangulation of GRB events, producing localization maps that could be employed in synergy with other space facilities.

Finally, I have reported in the Conclusions the future activities foreseen for further development of the XGIS instrument and the prospects for its use as a hard X-ray monitor for THESEUS or for other missions opportunities.

Chapter 1

High energy transient phenomena in Astrophysics: Gamma-Ray Bursts

In this chapter the focus is set on the general description of Gamma-Ray Bursts, transient events with high energy, capable of suddenly light up the γ-ray sky.

In order to detect these wide-interest events, a large amount of technological studies are being carried and new space facilities developed. In fact, these astrophysical phenomena are chosen as target for several space missions funded by space agencies worldwide, as HiZ-GUNDAM (JAXA; Daisuke et al., 2020), Gamow (NASA; White et al., 2021) and the candidate ESA M7 mission THESEUS (ESA; Amati et al., 2021), therefore an introduction is needed to understand what type of science can be done and what research-goals the mission may be willing to achieve by searching and observing these bursts. After a listing of the general observational properties, two different types of burst are introduced, putting attention on the respective different progenitors, the common physical mechanism originated by a central engine and the spectral and temporal properties of the emission. Such features have been detected and studied by past satellites, with instruments onboard satisfying very specific scientific and technological requirements, taken as starting point for future facility developments, as it will be further described in Chapter 2.

1.1   Generalities

Gamma-Ray Bursts (GRBs) are the most luminous events currently known, characterized by bright and short flashes of radiation with spectral energy distributions peaking in the hard X-ray/soft γ-ray band (e.g., Gehrels et al., 2009; Longair, 2011; Vedrenne & Atteia, 2009), capable of overshining any other γ-ray source.

One of the main scientific goals of past and recent high-energy facilities is to populate the GRB sample: the extension of the sample offers a statistical opportunity
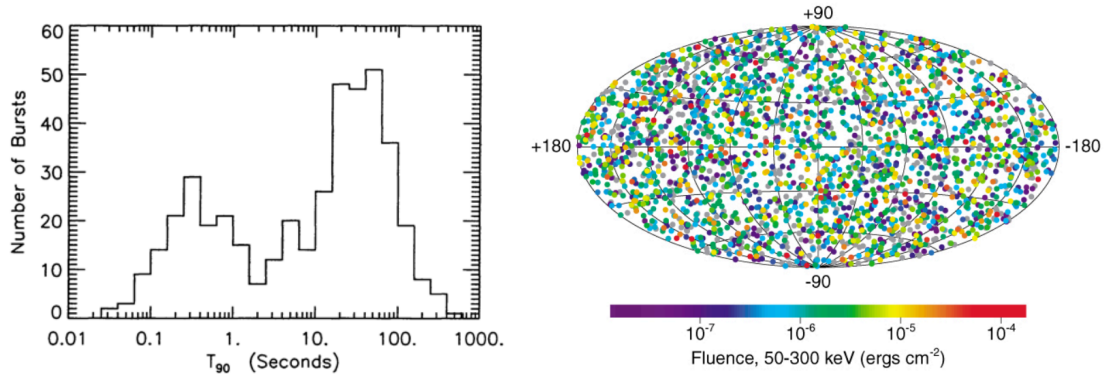
(a) *Distribution of duration for 427 GRBs from the 3rd BATSE Catalog (Vedrenne & Atteia, 2009).*

(b) *Distribution of 2704 γ-ray bursts over the sky as observed by the BATSE experiment of the Compton Gamma-Ray Observatory (Longair, 2011).*

Figure 1.1: *Bimodal duration distribution (left) and isotropic spatial distribution (right) of two GRBs samples from BATSE.*

to achieve a general description of the underlying physics and the main properties of this kind of objects. Thus, an historical overview of the most important results reached in this scientific field during the last decades is now presented, mostly referencing Vedrenne & Atteia (2009).

During the 1990s, thanks to the Burst and Transient Source Experiment (BATSE), the first properties of GRBs were established:

- GRBs time of occurrence and location is not predictable;

- GRBs duration (from fraction of seconds to minutes) shows a bimodal behaviour: they can be distinguished in "short" and "long", by a threshold in duration equal to 2 s (Fig. 1.1a);

- GRBs present a non-thermal spectrum and variability at the level of ms;

- GRBs are uniformly distributed over the sky, suggesting a cosmological distribution (Fig. 1.1b).

It was difficult to localize and identify these events due to their random occurrence in the sky, a lack of repetitions of the sources and their short duration, especially without an adequate positional accuracy. Thus, triangulation methods were implemented (e.g., spacecrafts cooperating in the Interplanetary Network), as well as large Field of View detectors covering the entire sky.
The isotropic distribution first induced to think about a Galactic origin in our

close proximity, but also the indications coming from extragalactic and cosmological models were taken into account: thanks to BATSE, the deficit of faint bursts were demonstrated (i.e. non-homogeneous distribution of the sources regarding their intensity), leading to the necessity of rejecting a Galactic origin and putting constrains about their energy budget.

In fact, for a galaxy disk population at 100 pc, the energy required to detect a burst is 10^{38} erg, but with BATSE the minimum distance scale compatible with the constrain of isotropy became 100 kpc, implying galactic halo models, with an energy release of 10^{44} erg, that however could not be consistent with the BATSE energetic results. Hence a compatible model for the description of such bursts was the cosmological origin (order of Gpc) with an energy budget beyond 10^{52} erg.

Cosmological sources would explain isotropy and non-homogeneous distribution of sources, but the non-thermal nature of the emission and the huge energy release were still issues to be addressed.

Assuming that GRBs were extragalactic phenomena implied extreme energy densities during the event, with the subsequent creation of an ultra-relativistic shock wave, in which electrons were accelerated to very high energies. These electrons would emit synchrotron radiation, consistent with the observed power-law spectra of the bursts. Although the intense γ-ray emission lasts only a short time at γ-ray energies (the so called "prompt emission"), the emission would be expected to last much longer at lower energies, so an "afterglow" emission was predicted, which would appear in the X-ray, optical, infrared and radio wavebands (e.g., Longair, 2011). This new possibility of carrying out multi-wavelength observations of GRBs paved the way to a deeper comprehension of the physics underlying these events, but, in the early stage of GRB studies, despite the results of BATSE, the absence of observed counterparts at other wavelengths did not allow GRB sources identification, a task later taken over by *BeppoSAX*.

In 1997, *BeppoSAX* made it possible to detect and locate GRBs at the level of arcminutes, to perform deep X-ray observations, discovering their X-ray afterglow (Fig. 1.2, the discovery of GRB90228 afterglow), allowing also optical and radio detection of the afterglows from ground-based facilities. Therefore, counterparts were finally found thanks to *BeppoSAX*, allowing distance measurements and an identification of their hosts, confirming that the bursts take place at cosmological distances. If one assumes an isotropic emission, the possibility of detecting GRBs at high redshift translates into a huge energy release. This lead to the possibility of GRB collimated emission: if the beaming is significant, it can reduce the amount of emitted energy by some orders of magnitudes. Further afterglows observations located GRB sources in star forming regions of galaxies, implying the emission of relativistic jets from newly born stellar black holes and thus confirming the hypothesis of collimation.

7
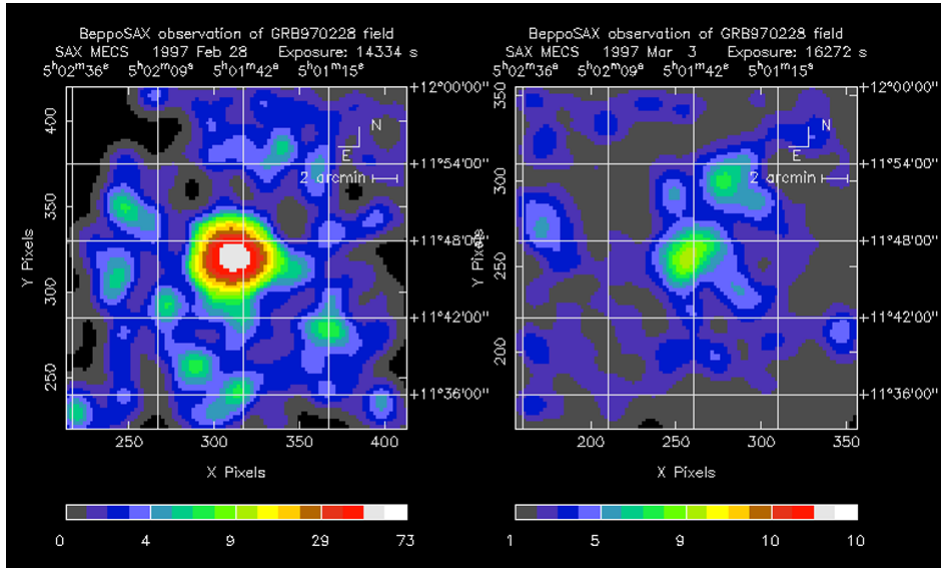
Figure 1.2: *Images of the source 1SAX J0501.7+114 detected with BeppoSAX Medium Energy Concentrator Spectrometer (2 - 10 keV) in the error box of GRB90228 during a first and a second BeppoSAX Target of Opportunity observation. The probability that the source detected during the second pointing is coincident by chance with the position of 1SAX J0501.7+1146 is of the order of 1×10^{-3}. From one pointing to the other the source is faded by a factor 20 in three days (Costa et al., 1997).*

In 1998, *BeppoSAX* provided the first clue of a possible connection between a GRB and a supernova (SN 1998bw), whose time of explosion was compatible with the time of occurrence of the GRB, a connection later confirmed by *Swift*, that supported the origin of GRBs from collapsar model (Iwamoto et al., 1998).

However, with *BeppoSAX* it was not possible to localize short GRBs, a task later assigned to *Swift*. The search for the afterglows was carried by the latter satellite, obtaining the position of the bursts and confirming the association of these events with extragalactic objects. The localization through afterglow emission allowed the measurement of bursts distance scale thanks to their redshift.

The sample of GRBs with measured redshift progressively increased in number with a major advancement imprinted by the *Swift* satellite which detected the first short GRB afterglow and revealed the temporal structure of the early X–ray afterglow, thus providing a new picture of the transition between the prompt and the afterglow phase.

Since 2008, the *Fermi* satellite revealed the emission of GRBs in the 10 keV – 100 GeV energy range, enabling a systematically study of the shape of the prompt emission of long and short GRBs. Moreover, recently the ground-based Cherenkov telescope MAGIC clearly detected the inverse Compton peak $(0.2 - 1$ TeV$)$ of the afterglow emission in the nearby GRB190114C (Acciari, 2019), enabling GRB

studies toward higher ranges of energies, hoping to unveil a more detailed physics of the prompt emission.

While the observational picture of GRBs was enriched by both the progressively larger sample of GRBs with measured redshifts (less than 500, with redshift spanning the range $0.04 \leq z \leq 9.4$; Tsvetkova et al., 2021, and Poolakkil et al., 2021) and by the study of the emission in the MeV–GeV energy range, the sample of high-redshift GRBs comprises only 6 events at z > 6 (Ghirlanda et al., 2021). The task of expanding the high-z GRB sample is matter of nowadays research, and will be discussed in Chapter 2.

1.2 GRB progenitors and central engine mechanism

At cosmological distances, the energy releases of GRBs are enormous and liberated in few seconds. It is conventional to write the energy emitted as $E = E_{iso}(\Omega/4\pi)$, where E_{iso} refers to the energy emitted isotropically and Ω is the solid angle within which the energy is emitted. The most energetic bursts have isotropic energies that span between 10^{50} and 10^{54} erg. However, the radiation is likely to be strongly beamed and so the energy requirement can be very significantly reduced.

Theories to address the origin of GRBs were developed, taking into account several observational evidences. Firstly, this range of energy is smaller than the rest-mass energy of a compact stellar object and also the variability timescale suggests that the energy is deposited in a small volume by a central engine, as the energy is not completely released instantaneously. Moreover, due to the lack of repetition of the phenomena, it seems that the progenitor gets destroyed, leading to the conclusion that GRBs seems to be associated to mass accreting disks onto compact objects (e.g., Longair, 2011).

Such scenario is compatible both with the explosion at the end of life of a massive star and with the merger of binary compact stellar remnants, such as black holes and neutron stars. The remnant of these catastrophic events is in any case a spinning black hole with an accretion disk or torus formed by the debris (Fig. 1.3). This material can feed the GRB with gravitational energy of the in-falling matter of the disk or torus onto the black hole. Moreover, the spinning black hole is needed to create a region free of matter, where a jet is able to form and escape. An alternative accretion can involve magnetars: a spinning compact object, with strong magnetic field (B up to 10^{14-15} G) and pulsar-like activity (e.g., Vedrenne & Atteia, 2009).
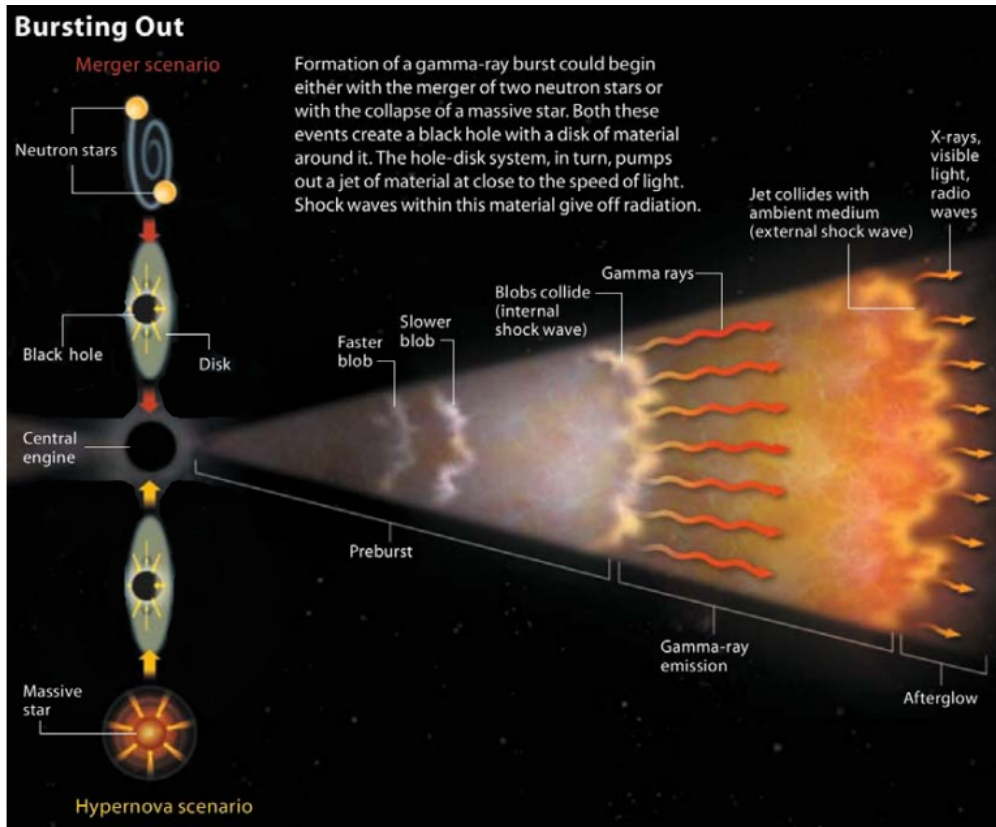
Figure 1.3: *Illustration of the two main scenarios for the production of a GRB: both collapsar and merger of compact objects lead to a central black hole surrounded by a disk (Vedrenne & Atteia, 2009).*

1.2.1 Standard model for GRBs

As already mentioned, GRBs imply huge energies that are released in few seconds from compact objects, i.e. really small volumes. As explained in Vedrenne & Atteia (2009), these features imply the formation of an e^+, e^- and γ fireball that power a jet, exploding from a source that is extremely opaque. The fireball is formed thanks to the annihilation of neutrino and antineutrino pairs above the accretion disk of a newly born black hole because, in the hottest inner part of the disk, neutrino cooling is expected to become very efficient. Initially, the fireball has electron-positron pairs in equilibrium, that after the expansion fall out of equilibrium and recombine.

Two problems arise in the explanation of GRBs assuming this simple model: first, the radiation emitted when the outflow becomes optically thin should be thermal, instead a non-thermal power-law spectrum is observed; second, the timescales at which the photons escape would be comparable to the timescales at which the

10

outflow becomes optically thin, matter of milliseconds instead of the observed GRBs durations.

These issues are solved assuming the fireball to expand relativistically and baryon contamination: the interaction of the baryons with the fireball medium takes place in relativistic shocks, that allow an emission of energy producing a non-thermal spectrum, because shocks can convert the bulk kinetic energy back to internal energy of non-thermal radiation and particles. A high number of electrons is also needed to accelerate the shock and then to radiate through synchrotron or synchrotron-Inverse Compton (IC) emission.

Therefore, the introduction of external and internal shocks in the model is a direct consequence of what previously said and is better explained by focusing on the mechanisms leading the evolution of the fireball. This theoretical model featuring shocks has been proposed by Meszaros & Rees (1993).

Inside the radius of the fireball, particles have random isotropic velocities. The radial expansion by the external medium is at first accelerated, by converting the internal thermal energy into bulk kinetic energy adiabatically.

As the fireball expands and accelerates, a rarefaction wave propagates inward.

Then the fireball becomes optically thin to Compton scattering and the radiation can escape through the burst. The external matter is swept outside the contact discontinuity in a shock wave (well describing the multi-wavelength afterglow radiation) and, under the effect of accumulation, it stars to decelerate the fireball matter, concentrated in a thin shell. This leads to a second, but more energetic, burst. Between the fireball material interface and the external shock the gas is heated, but once the deceleration starts, a reverse compression wave propagates inward into the fireball material. These shocks occur in the fast moving ejecta, when the time varying outflow from the the central engine leads to the ejection of successive shells; multiple shocks are present when multiple shells interacts. The main burst occurs when the matter in the blast wave shell cools. This behaviour explains well the rapidly varying light-curve of the prompt emission.

1.2.2   Origin of long GRBs: collapsar model

Collapsar are defined as rotating massive stars whose iron core will collapse directly in a black hole, which will accrete matter and emit a powerful relativistic jet, i.e. the GRB (e.g, Gehrels et al., 2009; Vedrenne & Atteia, 2009; Meszaros, 2019). The collapsar model, described in Vedrenne & Atteia (2009), requires three main components:

1. a star with a massive core;

2. the removal of the hydrogen envelope;
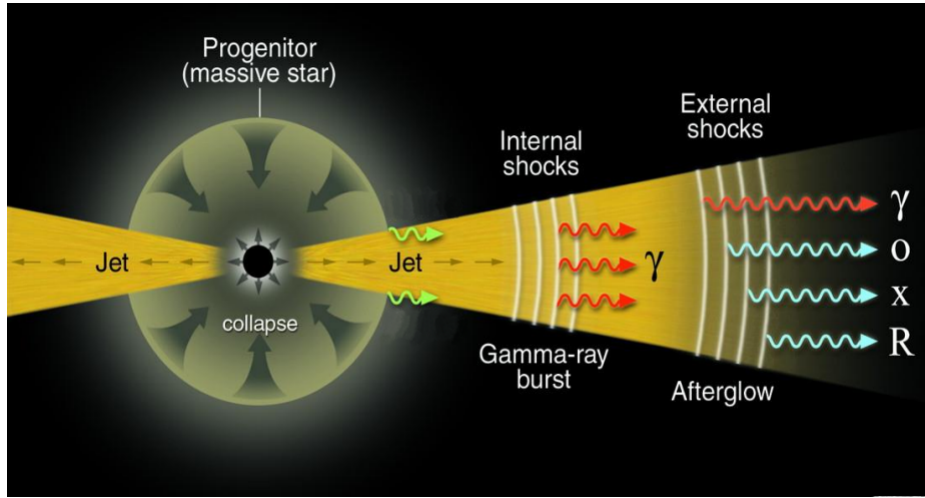
Figure 1.4: *The standard GRB model from a collapsar. The photosphere, internal shock and external shock resulting in the afterglow are shown (Meszaros, 2019).*

3. a high angular momentum in the core, to support the temporarily torus around the remnant.

These features are compatible with Wolf-Rayet stars, so closely related to progenitors of type Ib/c supernovae. The black hole may form either promptly, since an outgoing shock fails to be launched by the collapsed iron core (collapsar type I), or, in a mild explosion, by fallback (collapsar type II).

In collapsar type I scenario, long GRB progenitors are stars with masses above 35-40 $M_\odot$, that lost their H envelope before their death (Fig. 1.4). This kind of stars, during their Main Sequence phase, can have He core of 9-14 $M_\odot$ and will result in "failed supernovae": there is a two-step collapse of the Fe core of a rapidly rotating He star first into a neutron star, then directly into a black hole with a massive accretion disk, a gravitational energy reservoir powering a GRB. The supernova is not produced, prior the disk formation, because the outward shock is not launched by the collapsed Fe core.

As a consequence of in-falling matter in the area along the rotational axis and of stagnating matter in the equatorial area, a void region along polar direction is created, allowing a reversal of the flow: energy is dissipated in the disk by neutrino annihilation, which can power relativistic polar outflows of radiation into jets. Also strong magnetic fields are expected inside the disk, so magneto hydrodynamical energy dissipation is expected.

During the jet drilling of the star, the material in front of the jet head is heated and moved aside, forming a hot structure called "cocoon", which exerts a transverse pressure that confines and further collimates the jet. As the jet breaks through
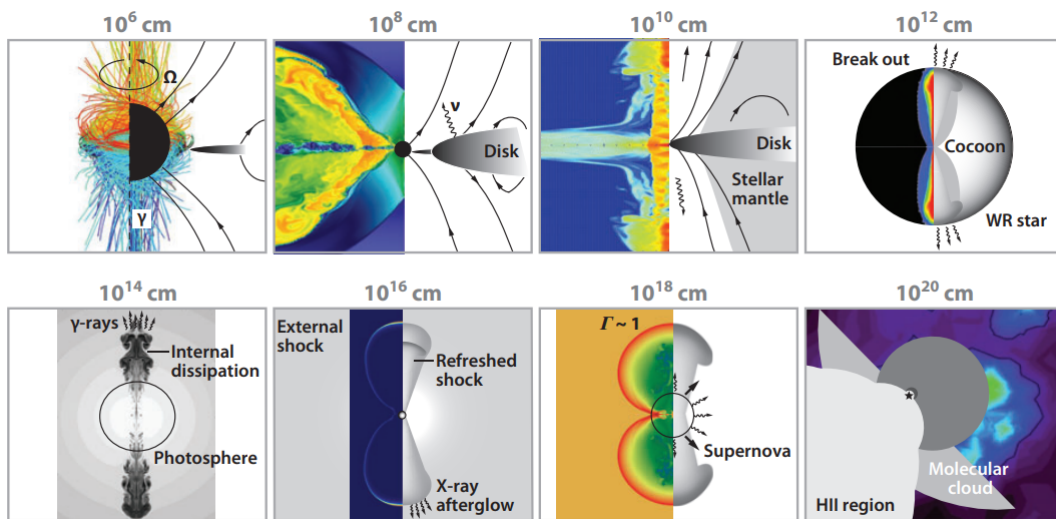
Figure 1.5: *Model for the production of a GRB from collapsar. (10^6 cm) The GRB nucleus and its magnetosphere. (10^8 cm) The accretion flow is likely to be embedded in a very active corona. Relativistic outflow from the black hole is focused into two jets. (10^{10} cm) Some beaming is expected because energy would be channeled preferentially along the rotation axis. The majority of stellar progenitors will not collapse entirely during the typical duration of a GRB. A stellar envelope will thus remain to impede the advance of the jet. (10^{12} cm) This is the typical size of an evolved massive star progenitor. A thermal break-out signal should precede the softer γ-rays observed in GRBs. (10^{14} cm) Velocity differences across the jet profile provide the most favorable region for shocks, producing highly variable γ-ray light curves. (10^{16} cm) The external shock becomes important when the inertia of the swept-up external matter starts to produce an appreciable slowing down of the ejecta. (10^{18} cm) End of the relativistic phase. This happens when the mass E/c^2 has been swept-up. Illustration from Gehrels et al. (2009).*

the star, relativistic matter is ejected, running into previously ejected winds, originating a soft GRB. The GRB itself appears only after the jet has broken out the star, cleaning the outer region for the relativistic plasma. Typically, the GRB is produced at $10^{14} - 10^{15}$ cm far from the star and starts $\sim$10 s after the formation of the black hole, when the jet dissipates part of its kinetic energy by powering an energetic γ-ray radiation known as the GRB prompt emission. Later on, the jet decelerates, shocking the interstellar medium and powering a fading synchrotron emission from X-ray to radio, the afterglow ($10^{16} - 10^{17}$ cm).

Variability rises due to a not steady accretion rate during the burst, reflecting disk instabilities into variable energy deposition, favouring the production of GRBs by internal shocks.

The succession of the main phases for the production of a GRB are summarized in Fig. 1.5.
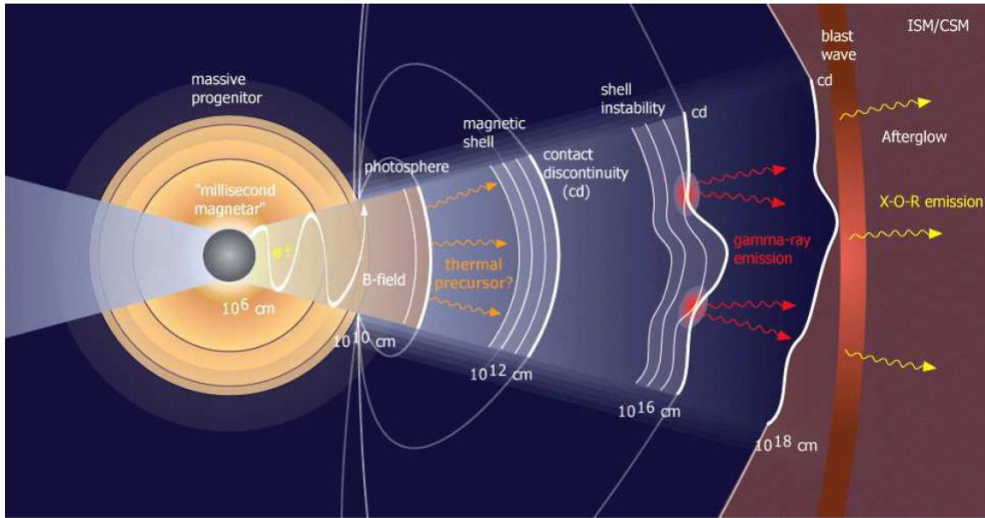
Figure 1.6: *GRB model for a magnetar: γ-ray and afterglow emission are shown, as well as magnetically driven winds (Lyutikov & Blandford, 2003).*

In collapsar type II scenario, the black hole is produced in a mild explosion: a supernova is created, in which the ejected shock cannot expel He and metals outside the neutron star, so the ejected material decelerates and falls back, leading to a delayed formation of a black hole with a torus of matter as in type I collapsar. This happens for stars with masses in range 20-40 $M_\odot$, so a large population of stars is involved, implying that this kind of scenario is actually more frequent.
The energy of the jet depends now on the efficiency of magneto hydrodynamic processes in extracting energy from disk and black hole.

An alternative scenario, cited in Vedrenne & Atteia (2009), is a GRB model which includes a pulsar like activity of the inner engine: in this case, the outflow is not dominated by neutrinos which annihilate to produce pairs of e^+/e^- and radiation, but is magnetically driven, carrying large amount of energy through vacuum, providing a mechanism of transport without matter involved. For that to occur, magnetic fields need to be of the order of 10^{15} G, obtained at the formation of a rapidly rotating neutron star. In these stars (magnetars, Fig. 1.6), the very fast rotation and the wrapping of magnetic field lines allow the formation of magnetic structure over large scales, and can generate strongly magnetized relativistic winds.

To conclude, collapsar progenitors should be associated with star forming regions, where massive stars can form and die. Moreover, this type of collapsars are unable to produce bursts with durations shorter than $\sim$5 s (Vedrenne & Atteia, 2009).
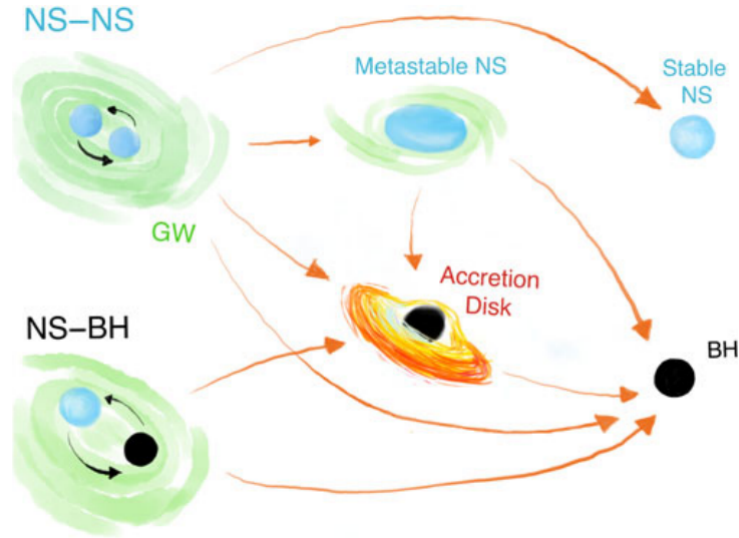
Figure 1.7: *Different scenarios for an NS–NS and an NS–BH merger and the merger remnant. The electromagnetic radiation is expected when an accretion disk and unbound mass are left outside the merger remnant (Ascenzi et al., 2021).*

1.2.3 Origin of short GRBs: compact binaries merger

The statistics of short bursts are much smaller than those of the long bursts and there is a clear relation with regions of low star-formation, both in elliptical galaxies and in regions of low star-formation rate within star-forming galaxies (e.g., Longair, 2011).

A black hole surrounded by a temporaneous accretion disk or torus is the common result of both collapsar and mergers of binary systems. Coalescing compact binaries with an electromagnetic counterpart include neutron star - neutron star (NS-NS) and neutron star - black hole (NS-BH) systems (Vedrenne & Atteia, 2009).

Fig. 1.7 shows that NS–BH mergers can only result in the formation of a more massive BH, with an accretion disk if the NS is disrupted outside the black hole innermost stable circular orbit, whilst an NS–NS merger can result in the formation of a BH, a stable NS or, in most cases, a metastable NS then collapsing to a BH. Electromagnetic emission may be suppressed when a BH is promptly formed and leaves no accretion disk nor ejected material in NS binary mergers, and when the NS is swallowed by the BH without being disrupted in NS–BH mergers (Ascenzi et al., 2021). As for long GRBs (Section 1.2.2), an accreting BH central engine can power a relativistic jet. This kind of system represents a huge reservoir of gravitational binding energy and, as a consequence of strong centrifugal forces, a clean region along the polar direction is formed: an energy release in the clean area

transforms into a radiation dominated plasma, that drills through the circumburst medium (constituted by the material previously expelled by the merger).

In this system, the two main reservoir of energy are the binding energy of the disk/torus and the spin energy of the black hole (Vedrenne & Atteia, 2009).

It is important to highlight that compact binary coalescences (CBCs) emit a variety of bright electromagnetic signals over the entire spectrum, from radio to γ-rays, but they are also sources of gravitational waves. Since the first detection of GWs in 2015 from coalescing binary BH-BH systems, tens of additional stellar-mass black hole coalescences, as well as two confirmed binary NS mergers and two confirmed (plus one possible) NS-BH mergers have been detected so far with Advanced LIGO and Advanced Virgo. These observations have confirmed the expectation that CBCs would represent the most common GW sources at the high frequencies where ground-based GW detectors are sensitive (i.e. from ~ 10Hz up to a few kHz), offering opportunities for a multi-messenger investigation.

The first GW detection of a NS-NS coalescence on August 17th 2017 (Fig. 1.8), accompanied by the observation of the short GRB (GRB170817A), the optical / infrared kilonova (AT2017gfo), and further X-ray, optical, infrared, and radio emission, provided a first striking example of what can be accomplished by combining together the information from GW and EM counterparts (Ciolfi et al., 2021). Hence, a major astrophysical implication of a joint detection of a short GRB and of GWs from a BH-NS merger is the confirmation that these binaries are indeed the progenitors of at least some GRBs (Abbott et al., 2017).
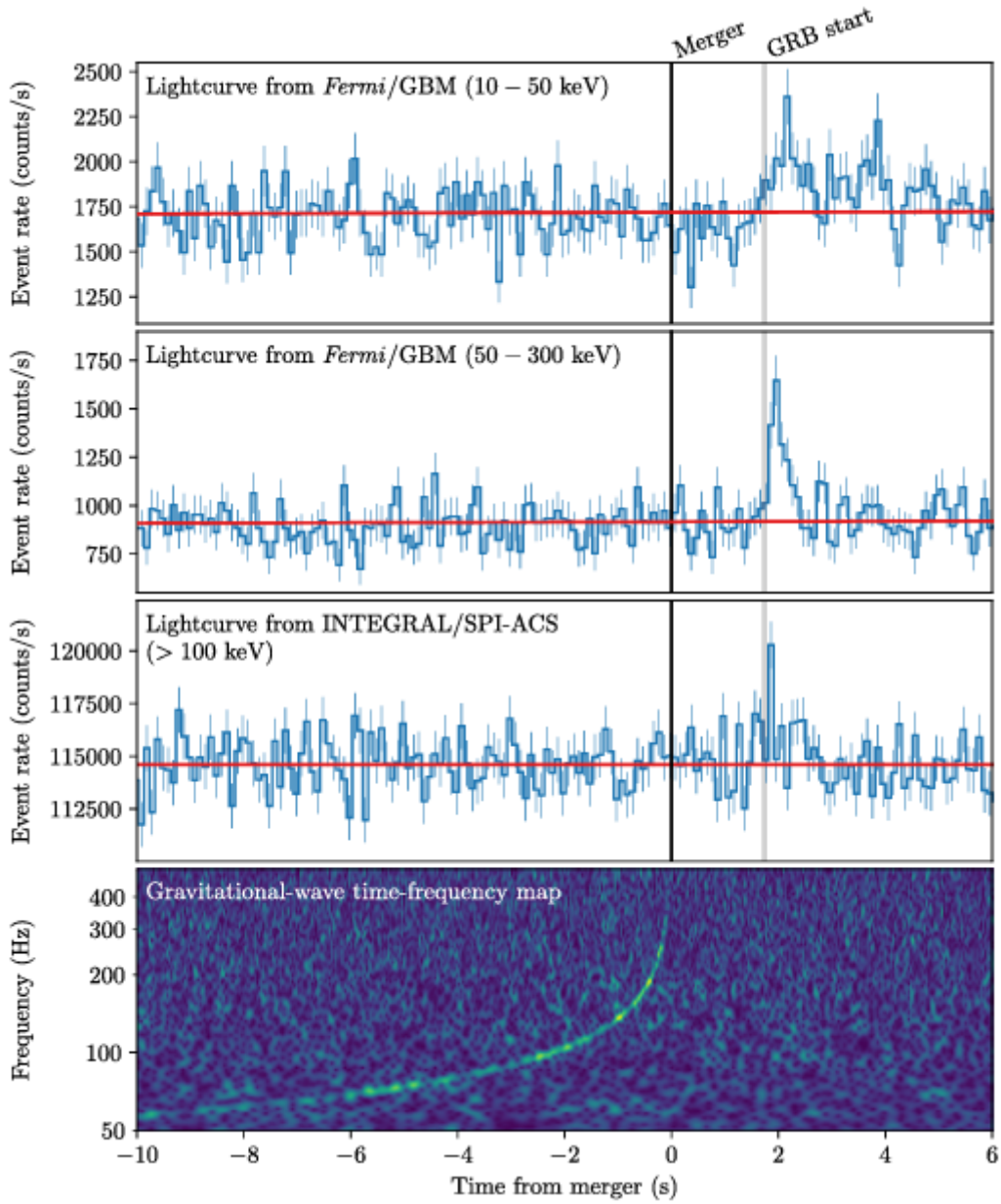
Figure 1.8: *Joint multi-messenger detection of GW170817 and GRB170817A. First: the summed GBM lightcurve for GRB170817A between 10 and 50 keV. The background estimate is overlaid in red. Second: the same as the top panel but in the 50–300 keV energy range. Third: lightcurve with the energy range starting approximately at 100 keV and with a high energy limit of least 80 MeV. Fourth: the time-frequency map of GW170817 was obtained by coherently combining LIGO-Hanford and LIGO-Livingston data. All times here are referenced to the GW170817 trigger time (Abbott et al., 2017).*

17

1.3 Prompt emission

Today, GRBs are observed throughout the electromagnetic spectrum, from radio to γ-ray energy band, but they were known predominantly as bursts of γ-rays, a feature independent from the progenitor generating the burst.

From spectral observations obtained by BATSE, the main property of GRBs spectra is their high-energy prompt emission: the emitted power per energy decade $E^2 \, dN_E(E)$ has a maximum around hundreds of keV, i.e. the observed peak energy E_P (Fig. 1.9). Band et al. (1993) described the time-averaged spectra with the following function:

$$
N_E(E) = \begin{cases} A\left(\frac{E}{100 \; keV}\right)^{\alpha} \exp\left(-\frac{E}{E_0}\right) & (\alpha - \beta)E_0 \geq E \\ A\left[\frac{(\alpha-\beta)E_0}{100 \; keV}\right]^{\alpha-\beta} \exp\left(\beta - \alpha\right)\left(\frac{E}{100 \; keV}\right)^{\beta} & (\alpha - \beta)E_0 \leq E \end{cases} \tag{1.1}
$$

where A is a normalization constant, α and β are the two photon spectral indices and $E_0 = E_P/(2 + \alpha)$.

This means that the spectra are well described at low energies by a power-law continuum with an exponential cutoff, $N_E(E) \propto E^{\alpha} exp(-E/E_0)$, smoothly joined to a steeper power-law at high energy, $N_E(E) \propto E^{\beta}$ (with $\alpha > \beta$). The transition between the two functions occurs at $E_{break} = E_0(\alpha - \beta)$.
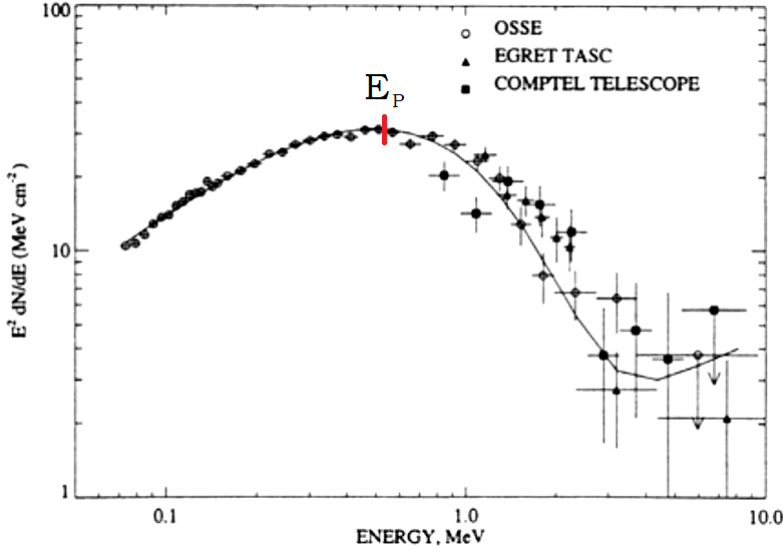
Figure 1.9: *Spectra of GRB 910601 taken as an example of high-energy spectra, extending to $\sim$10 MeV and showing the feature E_P. GRB 910601 was simultaneously observed with BASTE, OSSE, Comptel and Egret (Vedrenne & Atteia, 2009).*

18

The typical values of the parameters that appears in eq. 1.1 are centered in $\alpha = -1$, $\beta = -2.3$, $E_0 = 150$ keV, but an average GRB spectrum does not exist due to the wide parameters range of variability: besides, there is no correlation between the values that the parameters can have and the underlying physical process, i.e. the type of the burst (Vedrenne & Atteia, 2009).

A great variety of prompt light curves characterize both long and short GRBs. Being each light curve unique, it is necessary to find some quantitative relations between the many spectral parameters that can describe the temporal profiles, in order to find common behaviours or recurrences.
Some correlation diagrams taken from Gehrels et al. (2009) are shown in Fig. 1.10: the variability or spikiness of the light curve is found to be correlated with peak luminosity (L_{peak}) or total isotropic energy of the burst (a); the time lag of individual peaks seen at different energy bands is observed to be anticorrelated with luminosity for long bursts, while for short bursts the lag is small or not measurable (b); the E_P is also found to be correlated with E_{iso} for long bursts, including X-ray flares, with short bursts as clear outliers (c; Amati et al., 2002); the total isotropic energy emission is correlated with duration (d), with short and long bursts on approximately the same correlation line (short bursts detected by *Swift* have lower E_{iso}, on average, than long bursts); short GRBs seem to be harder in X-rays than long (e); finally, the prompt GRB light curves can generally be dissembled into a superposition of individual pulses with rise times shorter, on average, than decay times (f).

1.4   Afterglow emission

Burst Alert Telescope (BAT) and X-Ray Telescope (XRT) on board of *Swift* revealed that X-ray emission transitions from prompt emission into the decaying afterglow. Some example of X-ray light curves are shown in Fig. 1.11: they start with a very rapid power-law decline $\sim$100 s after the GRB trigger and, after about 1000 s, the slower power-law decline of the X-ray afterglow is observed (in some cases, an increased decline rate is observed after 10^5 s). X-ray flares are also observed in both long and short bursts. The rapid rise and decay, multiple flares in the same burst, and cases of fluence comparable to the prompt emission suggest that these flares are due to the same mechanism responsible for the prompt emission, which is usually attributed to the activity of the central engine (Gehrels et al., 2009).

This observed X-ray light curve behaviour is summarized in a schematic representation, shown in Fig. 1.12, characterized by: the prompt emission, an initial steep decay, a shallower than normal decay/a plateaux, a normal decay, jet breaks and one or more X-ray flares appearing well after the prompt phase in $\sim$50% X-ray
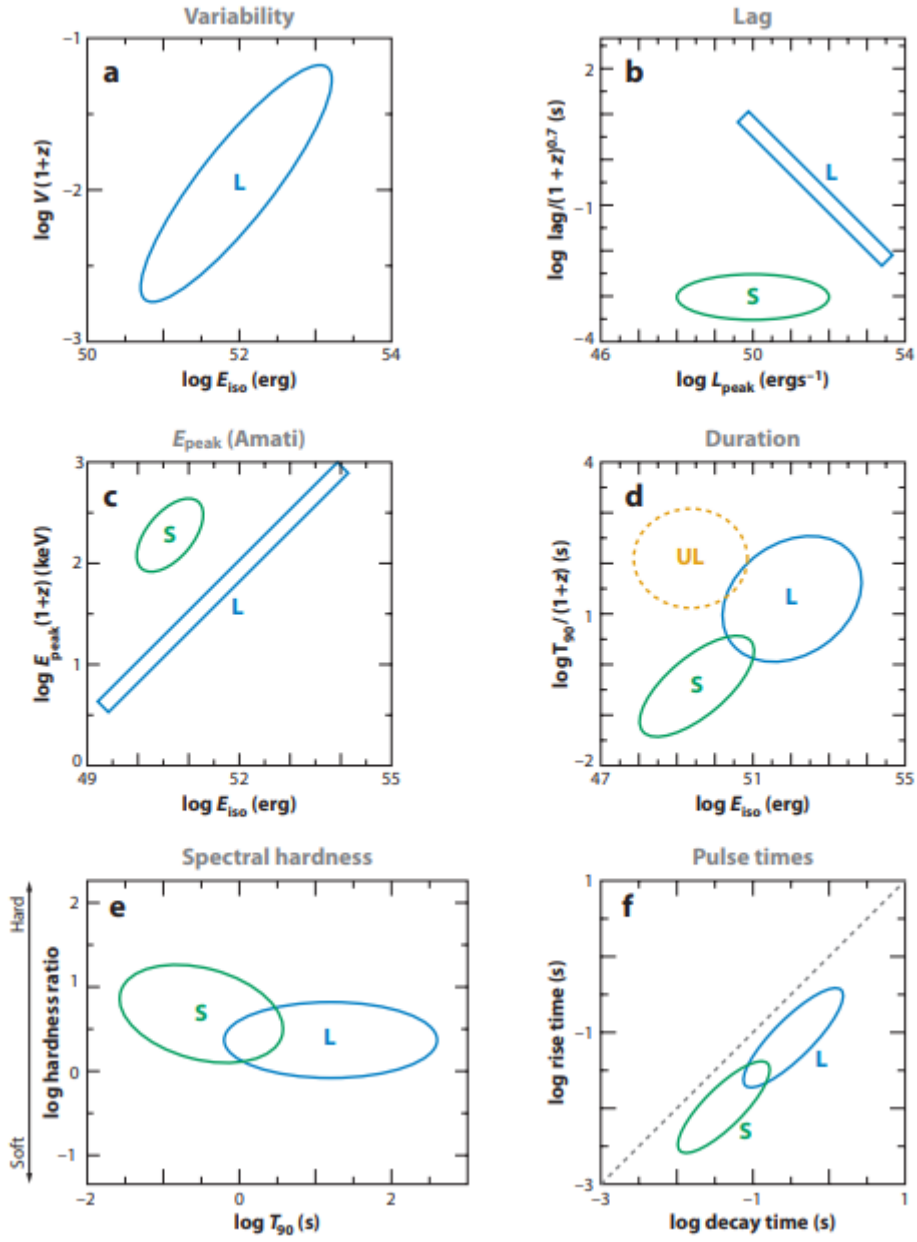
Figure 1.10: *Schematic diagrams illustrating the most widely discussed correlations between various prompt emission properties for long (L) and short (S) GRBs (Gehrels et al., 2009). T_{90} is the time interval between the instants at which 5% and 95% of the total fluence are detected.*
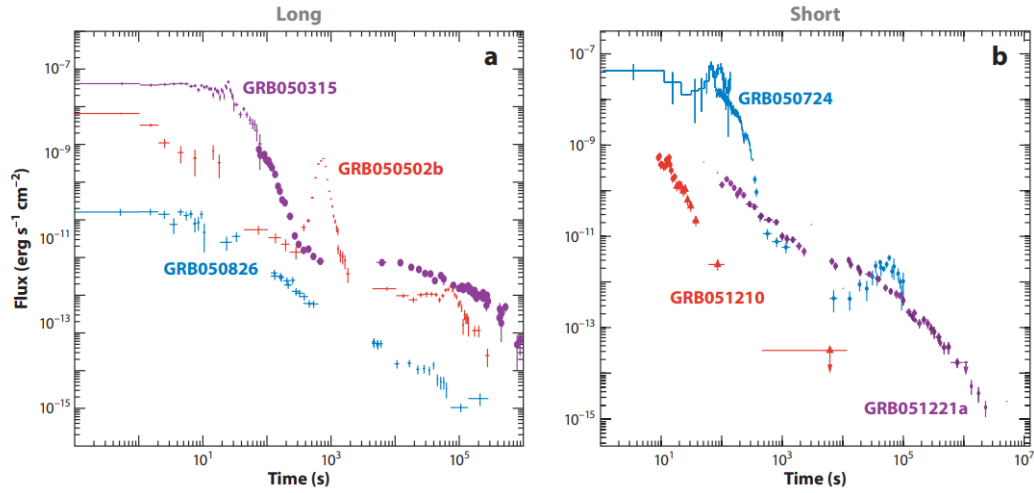
Figure 1.11: *X-ray afterglows of long (left) and short (right) Swift events with steep-to-shallow transitions (GRB050315, 050724), large X-ray flares (GRB050502b, 050724), rapidly declining (GRB051210) and gradually declining (GRB050826, 051221a) afterglows (Gehrels et al., 2009).*
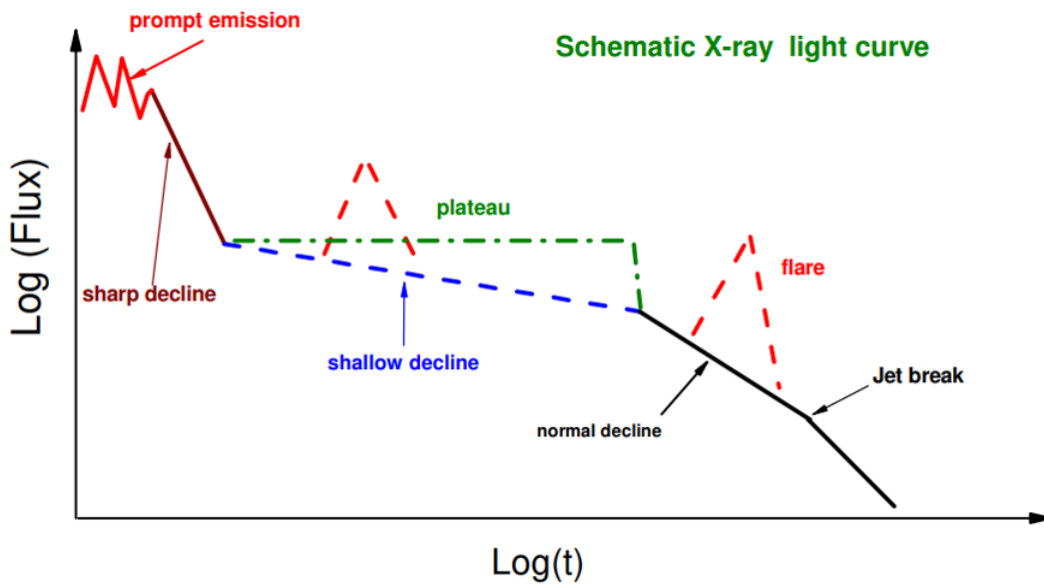
Figure 1.12: *Synthetic cartoon X-ray light curve based on the observational data from the Swift XRT. Four power-law light-curve segments together with a flaring component are identified in the afterglow phase (Fan & Piran, 2008).*

afterglows. Segments drawn as dashed lines are present only in a fraction of GRBs (Zhang et al., 2006).

As already said, afterglows are observable also in other energy bands, as optical and radio (e.g., Longair, 2011, Gehrels et al., 2009).

1.4.1 Environment

What is known about GRBs is derived from the observation of afterglows illuminating the surrounding medium (circumburst medium, CBM), allowing to characterize the environments in which these bursts take place.
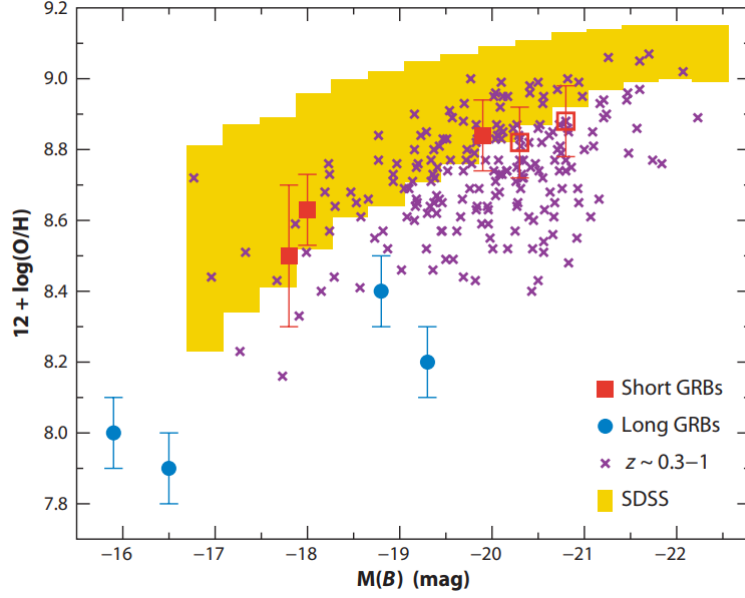
Host galaxies of long GRBs

For long GRBs, surveys established a standard picture for the GRB hosts as sub-L^* galaxies[1] (median $L \sim 0.1L^*$), with exponential-disk light profiles and high Specific Star-Formation Rates (SSFR $\sim 1 \ Gyr^{-1}$). An example is shown in Fig. 1.14a.

Thanks to *Swift*, the redshift range of these host galaxies has been expanded (from z ~ 4 to z ~ 9): due to redshift determination only via afterglow spectroscopy, it is possible to avoid mass and luminosity selection effects, thus host galaxies can be used to explore the evolution of mass-metallicity relationship (Fig. 1.13). From these studies of mass-metallicity, long GRB progenitors seem to require a low-metallicity environment, with increasing prevalence of such environments at z > 1. This would also agree with observations that the GRB rate seems to increase with redshift faster than the cosmic star-formation rate, leading to an offset between the true star-formation rate and that traced by GRBs: star-formation studies at $1 < z < 4$ confirm that the GRB redshift distribution is consistent with independent measures of star-formation, but there are signs of differential evolution of the GRB rate, where the GRB rate increases more rapidly with increasing redshift than expectation based on star-formation measures alone, providing a bias toward low-mass and low-metallicity host galaxies. Thus, if GRBs in low-metallicity environments and low-mass galaxies are more luminous, then they are likely to be overrepresented. As galaxy mass builds up through mergers, it is also possible that the highest-z GRBs could be systematically more luminous due to their lower-mass host galaxies.

---

[1] L^* is the characteristic galaxy luminosity controlling the cut-off of the Schechter function.

Figure 1.13: *Metallicity as a function of B-band absolute magnitude for the host galaxies of short (red) and long (blue) GRBs. The yellow bars mark the 14–86 percentile range for galaxies at $z \sim 0.1$ from the Sloan Digital Sky Survey, whereas crosses designate field galaxies at $z \sim 0.3\text{-}1$. Both field samples exhibit a clear luminosity-metallicity relation. The long GRB hosts tend to exhibit lower-than-expected metallicities, whereas the hosts of short GRBs are in excellent agreement with the luminosity-metallicity relation. From Gehrels et al. (2009).*

Host galaxies of short GRBs

For short GRBs, the observations of the afterglow showed an association with regions of low star-formation, either in low star-forming elliptical galaxies or in a region of a galaxy with low star-formation. Thanks to the localization of this type of GRBs, three classes of host could be identified (Gehrels et al., 2009):

1. low-redshift (z < 0.5), high-mass ($L \sim L^*$), early-type host galaxies and galaxy clusters (Fig. 1.14b);

2. low-redshift, sub-L^*, late-type galaxies;

3. faint, star-forming galaxies at z $\sim$ 1, reminiscent of the host galaxies of long bursts.
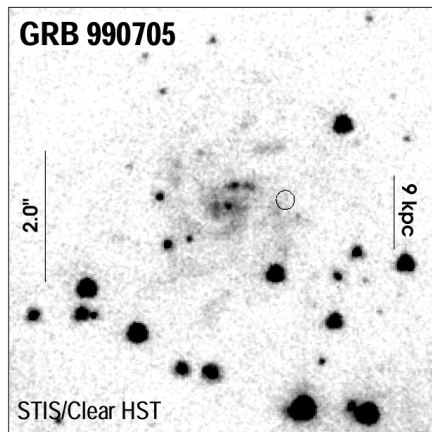
(a) *Location of GRB990705 (long-duration) in its host galaxy. The spiral structure of the host is clearly visible.*
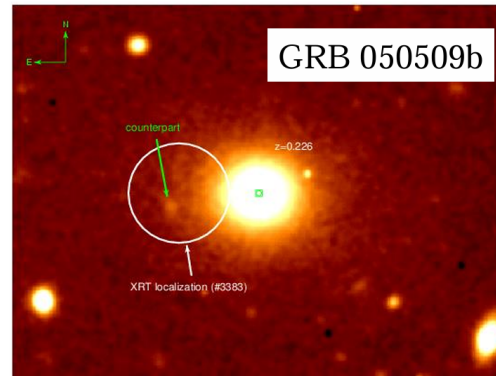
(b) *Location of GRB050509b (short-duration) in its host elliptical galaxy.*

Figure 1.14: *Different GRB locations. Images taken from Bloom et al. (2002).*

Chapter 2

THESEUS ESA M7 candidate for a future GRB space mission

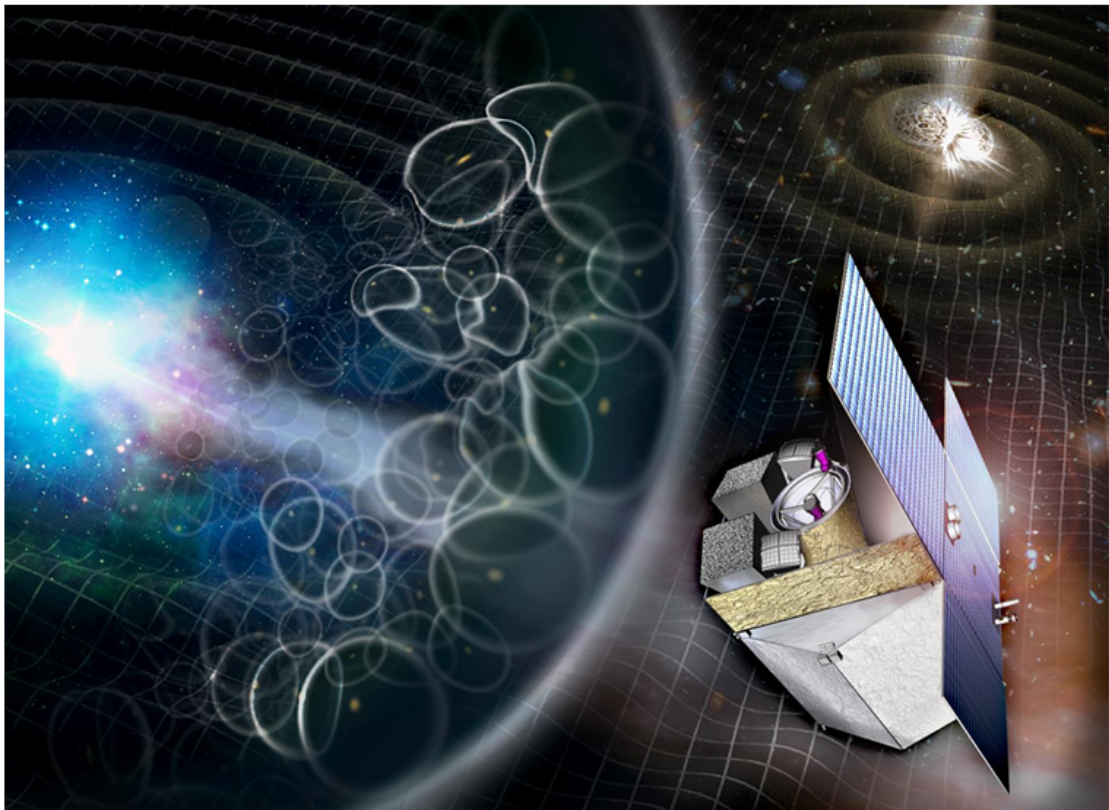In this Chapter, attention is put on GRBs as scientific probes of fundamental astrophysical theories; as such, they are subject of a multitude of space mission proposals. After a brief introduction on how a GRB mission is built, the focus is on the description of the candidate ESA M7 mission THESEUS and how it can exploit GRBs for answering unsolved problems in Astrophysics.

2.1   Concept of a GRB mission

GRBs are unique and powerful tools for cosmology: due to their high luminosity (with emission peaking in hard X and soft γ-rays) and to their redshift distribution, they can be used as probes of the early phases of star and galaxy formation, and the resulting reionization of the Universe at z $\sim$ 6–20. Thus, promptly localized GRBs could provide information about much earlier epochs in the history of the Universe.

Therefore, from the papers of Daisuke et al. (2020), White et al. (2021) and Amati et al. (2021), it is evident how the two scientific goals of every GRB space mission are the exploration of Early Universe and the Multi-Messenger Astrophysics. Hence, the common purpose is to shed light on the main open issues in modern cosmology, such as the population of primordial low mass and luminosity galaxies, sources and evolution of cosmic reionization, SFR and metallicity evolution up to the "cosmic dawn" (Fig. 2.1). At the same time, the missions will provide a substantial advancement of Multi-Messenger and Time-Domain Astrophysics by enabling the identification, accurate localisation and study of electromagnetic counterparts of sources of gravitational waves (Amati et al., 2021).

To achieve these goals, the missions need specific instruments on board, but generally the payload is composed by a GRB monitor and a lower energy telescope. The GRB wide field monitor should work in hard X-/γ-ray band and its purpose is the direct detection of GRB events. The telescope instead can work in other energy bands and is dedicated to follow-up observations in order to obtain specific measurements (imaging, spectroscopy, redshift measurements, etc.), targeted to the advance in the astrophysical domain regarding the already cited goals.

The next sections are completely dedicated to THESEUS space mission description, in terms of technological requirements and scientific goals.

2.2   THESEUS ESA M7 candidate

Transient High-Energy Sky and Early Universe Surveyor (THESEUS) is a space mission developed in response to the calls for M-class missions by the European Space Agency (ESA). The study of the mission science case has been conducted
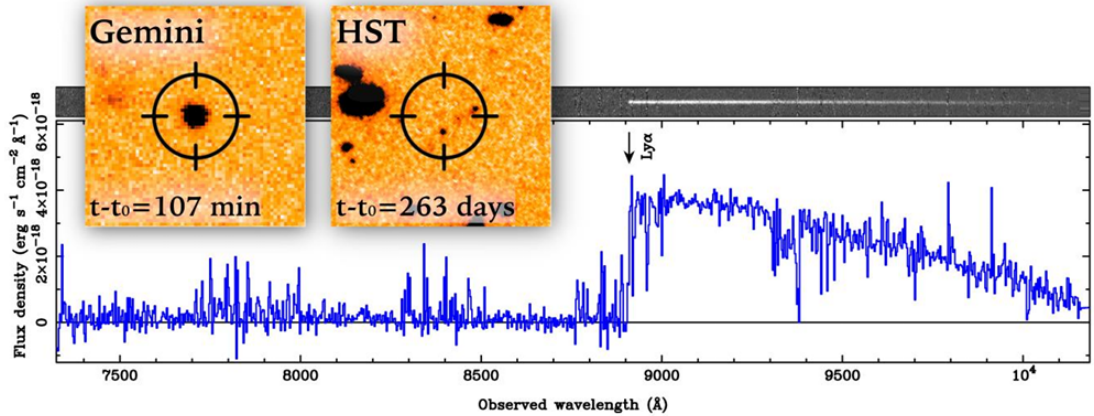
Figure 2.1: *The bright afterglow of GRB140515A at z = 6.3 imaged from Gemini (left inset), contrasts with the much deeper HST image of the same region (right), which provides marginal evidence of a host galaxy. The Gran Telescopio Canarias (GTC) afterglow spectrum (main panel) shows a sharp break at Ly-alpha, and detailed analysis of the spectrum places limits on the metallicity of $Z < 0.1Z\odot$ (Amati et al., 2021).*

by the ESA study Team and the *THESEUS consortium*, an entity coordinated by five main contributors and comprising most of the ESA member states. Italy acts as consortium lead, while United Kingdom, France, Switzerland, and Germany are co-leads. The members of the coordination team are supplying the payload and science ground segment elements of the mission (ESA-THESEUS, 2021).

THESEUS aims to fully exploit Gamma-Ray Bursts for investigating the Early Universe and advancing Multi-Messenger Astrophysics from identification of electromagnetic (IR/Optical/X-ray) counterparts to gravitational wave events. First, the attention is put on the physical conditions of the Early Universe by unveiling the GRB population in the first billion years; second, THESEUS will perform an unprecedented deep monitoring of the soft X-ray transient Universe, thus providing a fundamental synergy with the next-generation of gravitational wave detectors (Amati et al., 2018). This will be achieved through a step change in capability of detection (Fig. 2.2) and characterisation of GRBs and other transients, exploiting a very broad energy band (from 0.3 keV to 10 MeV) and a wide Field of View size.

Long GRBs, associated with the collapse of massive stars, allow to probe star-formation and gas physics over all redshifts, back to the era of reionization. In fact, GRB progenitors and their host galaxies are very good representatives of the massive stars and star-forming galaxies that may have been responsible for reionization, due to their intensive ionizing radiation. Therefore, a statistical sample of GRB at z > 6 is mandatory for an independent measurement of the cosmic SFR
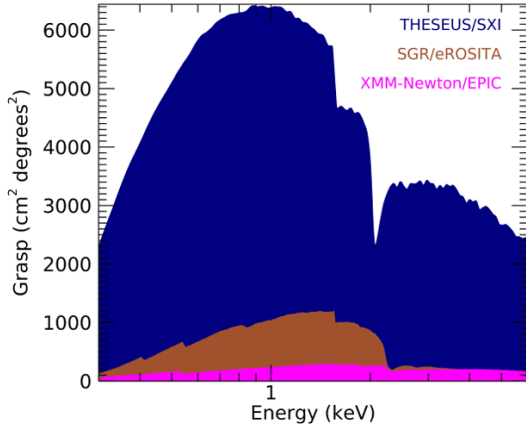
Figure 2.2: *SXI grasp (blue) as a function of energy compared to that of the X-ray survey mission SRG/eROSITA (brown), and XMM-Newton/EPIC (magenta), from Amati et al. (2021). The grasp is the telescope ability to capture light.*
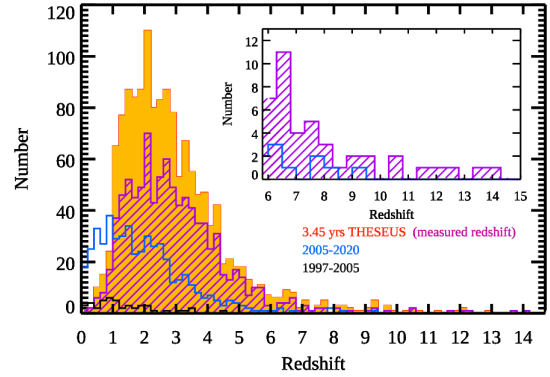
Figure 2.3: *Expected redshift distribution of long GRBs detected by THESEUS in 3.45 years of scientific operations (orange and purple histograms) based on GRB population modeling, compared with the redshift distribution obtained to date (blue and black histograms), from Tanvir et al. (2021).*

in the first phases of the Universe. The first generation of metal-free stars (Pop III) and the second generation of massive, metal-poor stars (Pop II) can result in powerful GRBs, opening the possibility to an identification of such old objects and a study of their hosts. Moreover, the role of Pop III stars in enriching the first galaxies with metals can be studied by looking at the absorption features of Pop II GRBs blowing out in a medium enriched by the first Pop III supernovae (Amati et al., 2018). Simulations show that THESEUS will identify and locate between 40 and 50 GRBs at z > 6 in 3.45 years of scientific operations (Fig. 2.3), with photometric redshift accuracy better than 10% thanks to the identification of Lyman break features shifted to the THESEUS telescope imaging sensitivity range (Amati et al., 2021).

Short GRBs, as discussed in Section 1.2.3, are associated with neutron-star compact binary mergers, known as powerful sources of gravitational waves (Amati et al., 2018). GW detectors have relatively poor sky localisation capabilities, mainly based on triangulation methods. For GW sources at distances larger than the horizon of second-generation detectors (200 Mpc), therefore accessible only by the third-generation ones around 2030 (e.g. Einstein Telescope and Cosmic Explorer), sky localisation may even worsen if the new generation network will be composed by only one or two detectors. In order to maximise the science return of the multi-messenger investigation, it is essential to have a facility that can detect

28
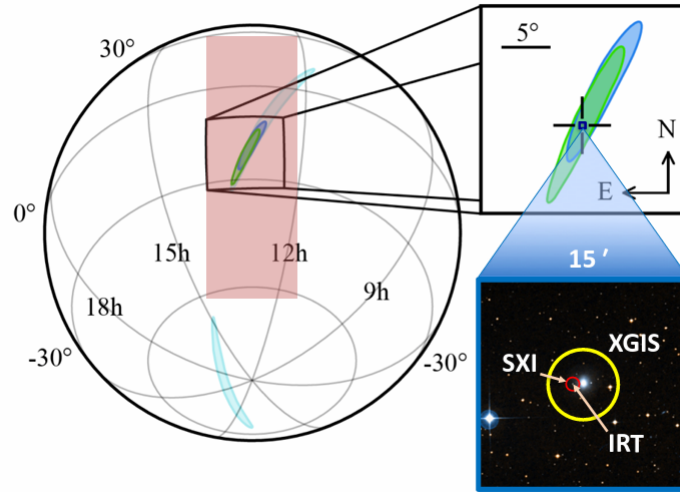
Figure 2.4: *THESEUS/SXI field of view (pink rectangle) superimposed on the probability skymap of GW 170817, obtained with the two Advanced LIGO (cyan) and with Advanced Virgo (green). THESEUS not only will cover a large fraction of the skymap, but will also localise the counterpart with uncertainty of the order of 15' with the XGIS and to less than 2' with SXI (Stratta et al., 2018).*

an electromagnetic signal independently to the GW event and can rapidly search with good sensitivity in the large error boxes provided by the GW facilities. These combined requirements are uniquely fulfilled by THESEUS, that will provide accurate localisation (Fig. 2.4), while GW archival data analysis will enable to search for simultaneous events at the time of the trigger (Stratta et al., 2018).

2.3   Instruments on board THESEUS

The scientific goals for the exploration of the Early Universe require the detection, identification, and characterization of tens of long GRBs occurred in the first billion years of the Universe ($z > 6$). This performance can be achieved by extending the GRB monitoring band to the soft X-rays with an increase of at least one order of magnitude in sensitivity with respect to previous X-ray monitors, as well as a substantial improvement of the efficiency of detection, spectroscopy and autonomous redshift measurement through on-board NIR follow-up observations. Meanwhile, the objectives on Multi-Messenger Astrophysics require an advancement in the detection and localization of short GRBs, monitoring the high-energy sky with an innovative combination of sensitivity, location accuracy and Field of View in the soft X-rays and finally imaging up to the hard X-rays and spectroscopy

up to the soft γ-rays.

Based on the scientific requirements of the mission, the THESEUS payload will be composed by three scientific instruments (Amati et al., 2021), whom Data Handling Units (DHU) will operate in synergy in order to optimize THESEUS capabilities. The instruments involved are:

- *Soft X-ray Imager* (SXI): a set of two "Lobster-eye" telescope units, covering an energy band of $0.3 - 5$ keV and a total FoV of ~ 0.5 sr with source location accuracy ≤ 2';

- *X/Gamma-ray Imaging Spectrometer* (XGIS): a set of two coded-mask cameras using monolithic SDD+CsI(Tl) X- and γ-ray detectors, granting a ~ 2 sr imaging FoV and a source location accuracy <15' in 2 - 150 keV, and covering a total energy band from 2 keV up to 10 MeV;

- *InfraRed Telescope* (IRT): a 0.7 m class IR telescope with imaging (I, Z, Y, J and H filters) and moderate spectroscopic capabilities (R ~ 400).

The three instruments placement on board of THESEUS have been studied by two industrial teams, as shown in Fig. 2.5.
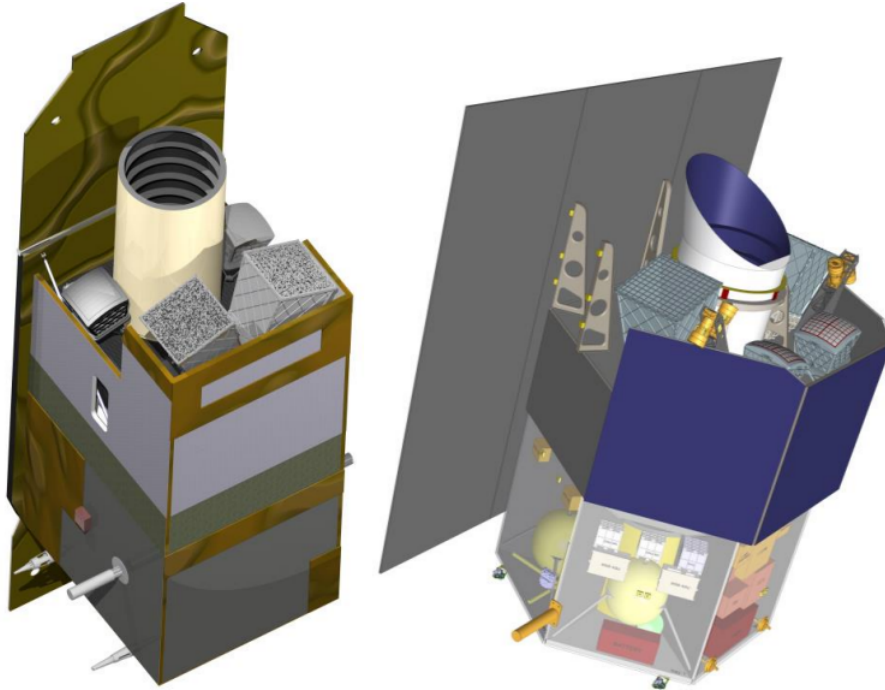
Figure 2.5: *Two spacecraft designs have been derived by industrial teams: schematic view of the spacecraft design for the Phase A of 2018-2021, ADS (left) and TAS (right) studies (ESA-THESEUS, 2021).*
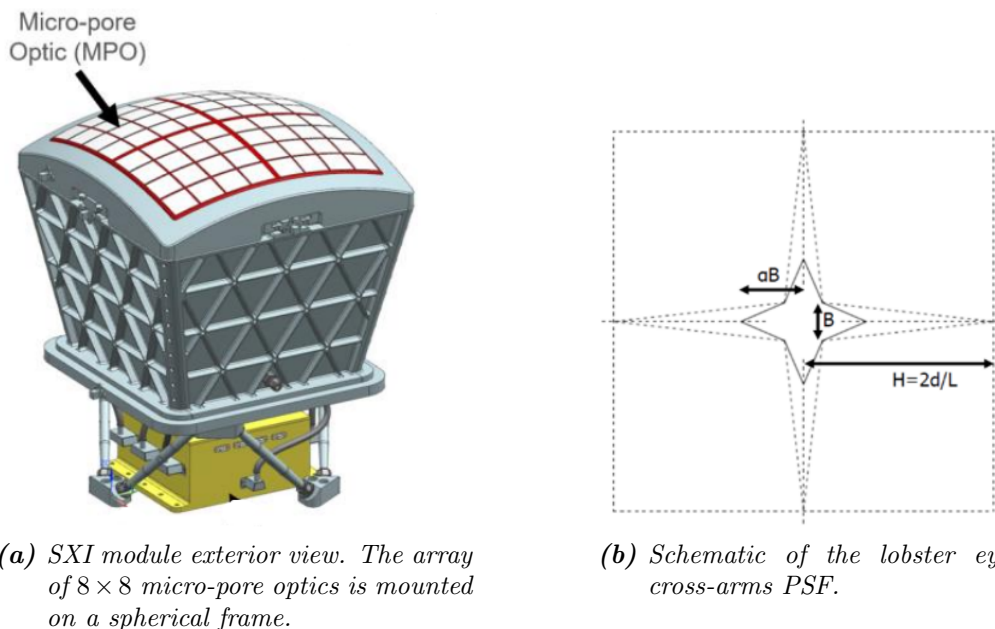
2.3.1 Soft X-ray Imager

The technical characteristics of SXI are taken from O'Brien et al. (2021).

The instrument is made of two wide-field "Lobster eye" X-ray cameras (Fig. 2.6a). By using Lobster eye wide-field focusing optics, an increase of sensitivity to fast transients is obtained, because such optics provide uniform sensitivity across a very large Field of View while maintaining a localisation accuracy of the order of arcminute.

Each module of SXI is composed by a matrix of squared micro-pore optics (MPO) mounted on a curved surface, and they will be aligned in order to overlap by 1° and be co-aligned with the IRT FoV.

With this configuration, X-rays which reflect off the square pore sides can form a central focus or a line focus depending on how many reflections in the MPO they undergo, giving a four cross-arm PSF, characterized by a central spot (Fig. 2.6b). The optics provide a transient location accuracy less than 2'.

A summary of the main characteristics of SXI is presented in Tab. 2.1.

Thanks to its capabilities, SXI will enable the discovery of many hundreds of X-ray transients per year, with a large sensitivity to high redshift GRBs, it will search for X-ray transients associated with multi-messenger sources and will monitor the X-ray sky on a wide variety of timescales, while simultaneously providing important targets for future observing facilities.

(a) SXI module exterior view. The array of 8×8 micro-pore optics is mounted on a spherical frame.

(b) Schematic of the lobster eye cross-arms PSF.

Figure 2.6: SXI structure (left) and schematic of its PSF (right); O'Brien et al. (2021).

Table 2.1: *Main structural and functional characteristics of SXI.*

| SXI	
Energy band (keV)	0.3 - 5
MPO size (mm^2)	40×40
Module optics configuration	8×8 MPOs
Module FoV (sr)	~ 0.25
SXI FoV (sr)	~ 0.5
SXI mass (kg)	82
Transient location accuracy	<2'

2.3.2 X/Gamma-ray Imaging Spectrometer

The technical characteristics of XGIS are taken from Labanti et al. (2021).
The XGIS system is composed of two coded-mask X-/γ-ray cameras. It has imaging capabilities up to 150 keV, in a FoV overlapping the SXI one, and is a spectrometer covering a wide energy range from keV to MeV. The XGIS FoV, defined as the solid angle through which a detector is sensitive to electromagnetic radiation, can be fully or partially coded (Fig. 2.9), depending if the direction of radiation is comprised in the FoV of detector+collimator or if it is below it, resulting in incident radiation hitting the side of the collimator and being partially detected by the instrument detection plane.
The detector plane contains 10×10 modules arranged side by side. A Module contains 8×8 Silicon Drift Detectors coupled to CsI(Tl) crystal scintillator bars (3 cm long), shown in Fig. 2.7a. The SDDs operate in an energy band of 2 - 30 keV, while the scintillators operate between 30 keV and 10 MeV. The imaging system of the XGIS is based on the coded mask technique (Fig. 2.7b): a tungsten coded mask is located 70 cm above the detection plane and has a random pattern with mask elements size of 2 times the detection pixel size (square pixels, of size 5 $\times$ 5 mm^2), providing an angular resolution of $\sim 1°$ and a source location accuracy $\leq 15'$. The two cameras are misaligned by $\pm 20°$ with respect to SXI and IRT, thus providing a total FoV of 117° $\times$ 77°. Above 150 keV, the FoV of an XGIS camera can be considered of the order of ~ 6 sr.
A summary of the main characteristics of XGIS is presented in Tab. 2.2, focusing on the instrument capability of detecting soft X-rays, hard X-rays and γ-rays.

The large extension of the energy band (2 keV - 10 MeV) allows XGIS to provide unique insight on the physics of the emission of GRBs through sensitive timing and spectroscopy: it can be used complementary to SXI to detect and localize both short GRBs (also determining the hard spectrum of these events, which makes them mostly undetectable with SXI) and high-redshift GBRs (thanks to the large
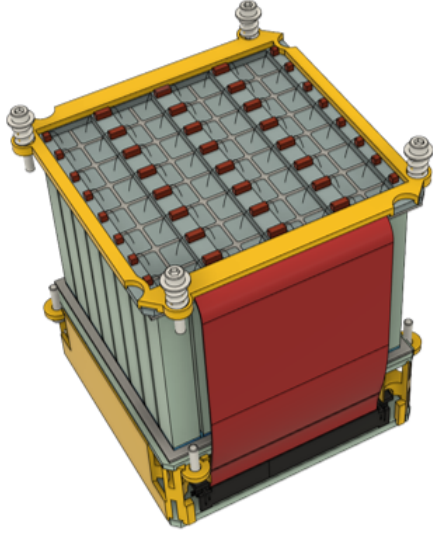
(a) *XGIS module: square SDDs on top and scintillator visible from the side.*
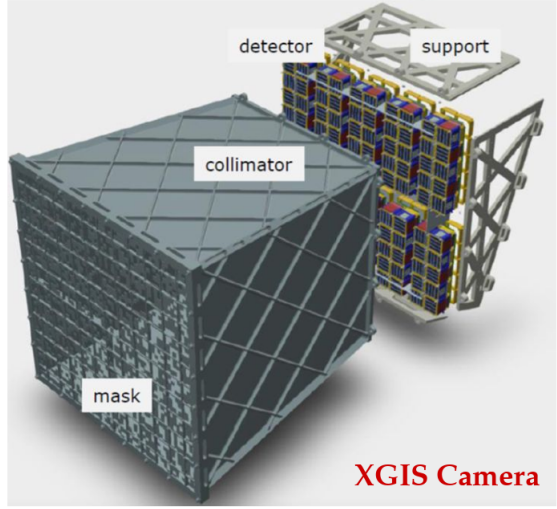
(b) *XGIS camera, with labelled components.*

Figure 2.7: *Costitutive elements of XGIS instrument (Labanti et al., 2021).*

Table 2.2: *Main structural and functional characteristics of XGIS.*

	XGIS	
Energy band (keV)	2 - 150	150 - 1000
FoV	117° ×77°	∼ 6 sr
Effective area (cm²)	∼ 500	∼ 1000
Angular resolution	< 120'	-
Transient location accuracy	≤ 15'	-
Energy resolution	≤ 1200 eV FWHM at 6 keV	≤ 6% FWHM at 600 keV
XGIS mass (kg)	190	

effective area).

The structure and working principle of XGIS will be discussed in more detail in Chapter 3.

2.3.3 InfraRed Telescope

The technical characteristics of IRT are taken from Gotz et al. (2021).
The IRT is a 70 cm, three-mirrors Korsch telescope, optimized for an off-axis line

of sight of 0.884°. The optical design will implement two separated Fields of View: one for photometry with a size of $15' \times 15'$ and one for spectroscopy of $2' \times 2'$. Using the photometric FoV, IRT will be able to acquire images using five different filters (I, Z, Y, J and H), while with the spectroscopic FoV it will provide moderate resolution ($R \sim 400$) slit-less spectroscopy in the 0.8 - 1.6 μm range. The different observation modes will be implemented through the IRT Camera, which includes a filter wheel, carrying the different optical filters and a grism, which will allow for spectroscopy.

A summary of the main characteristics of IRT is presented in Tab. 2.3, focusing on the instrument photometric and spectroscopic capabilities.

Thanks to the capabilities of IRT, an onboard and real-time measurement of the redshift of GRB afterglows is possible, focusing especially on those at high redshift. In addition, IRT will be used to characterize the afterglows through spectroscopy.
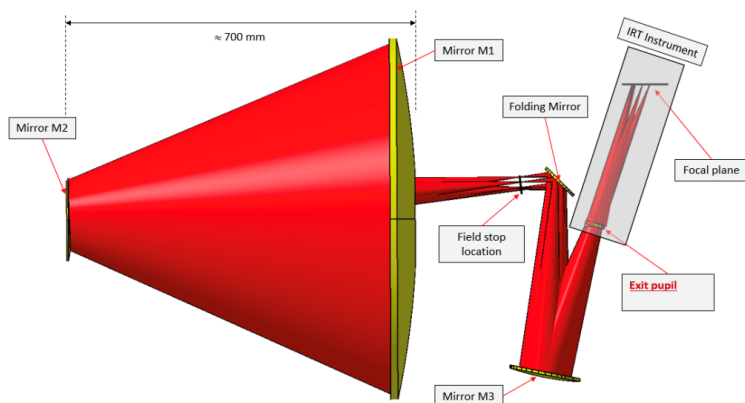
Figure 2.8: *IRT Optical scheme. M1, M2, M3 are under Italy responsibility. The exit pupil represents the optical interface with the IRT Camera provided by the consortium (Gotz et al., 2021).*

Table 2.3: *Main structural and functional characteristics of IRT.*

IRT	
Photometric wavelenght range (μm)	0.7 - 1.8
Photometric FoV	$15' \times 15'$
Photometric z accuracy	$< 10\%$
Spectroscopic wavelenght range (μm)	0.8 - 1.6
Spectroscopic FoV	$2' \times 2'$
Resolving power	~ 400
IRT mass (kg)	220

2.4 THESEUS observational modes
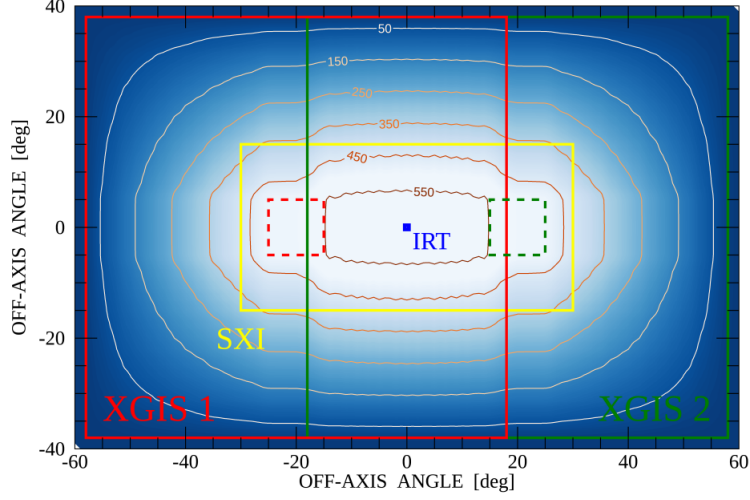
Figure 2.9: *Fields of view of the THESEUS instruments. The red (left) and green (right) squares indicate the partially coded FoV (solid lines) and fully coded FoV (dashed lines) of the two XGIS units. The yellow rectangle is the SXI FoV. The blue square indicates the pointing direction of the IRT. The contour lines indicate the effective area at 10 keV provided by the sum of the two XGIS units, assuming a 50% open fraction for the coded masks (Mereghetti et al., 2021).*

THESEUS is designed to catch high-energy transients and transmit information to the ground within few tens of seconds and full resolution data within a few hours. Most of the mission lifetime will be spent in the "Survey Mode", where the two wide field X-ray monitors (XGIS and SXI) observe portions of the sky searching for X-ray transients. Once an onboard trigger occurs due to an event localized by either XGIS or SXI (or both), the spacecraft will switch to the "Burst Mode" and will automatically slew to place the transient within the field of view of IRT. In Fig. 2.9, it is evident that XGIS and SXI FoV are covering a much wider area than IRT, which will first acquire a sequence of images in different filters during the "Follow-up Mode". The latter process lasts about 12 minutes. The acquisition by IRT aims at identifying the counterpart of the high-energy source, localize it with arcsec accuracy and provide a first indication of a possible high redshift event ($z \geq 6$). In order to determine onboard the redshift of the transient source, THESEUS will then enter in one of the two following modes:

- "Characterization Mode", during which the IRT will acquire a sequence of deeper images in different filters and then the spectra;

- "Deep Imaging Mode" during which only images in different filters will be

acquired, depending mainly on the IR brightness of the identified counterpart.

If the counterpart identified by the IRT is a known transient or variable source not associated with a GRB, the spacecraft will go back to the Survey Mode. The Survey Mode is anyway restored after the Characterization or Deep Imaging Mode is completed. The succession of modes is also described by Fig. 2.10.
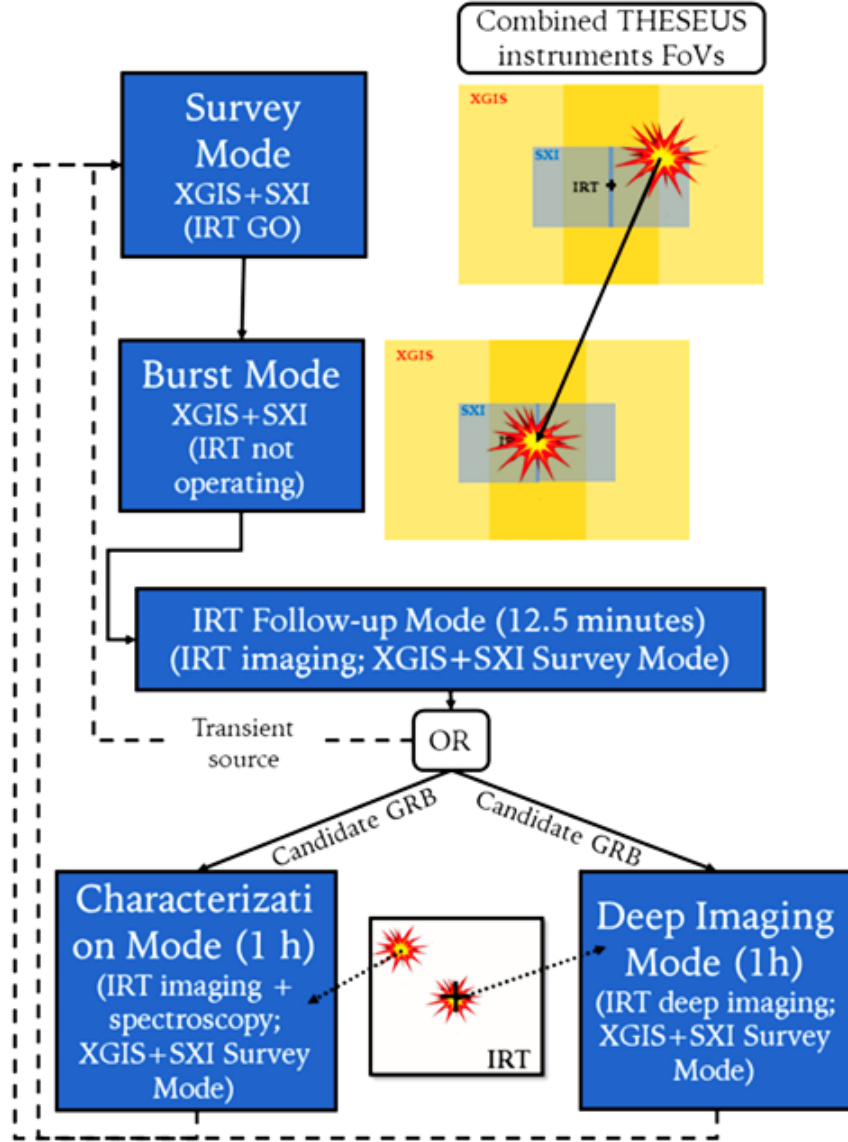
Figure 2.10: *THESEUS observational modes and strategy during the detection, follow-up and characterization of an internal trigger, i.e. an event detected by either XGIS or SXI, or both (Amati et al., 2021).*

THESEUS is also designed to rapidly respond to triggers that are provided by other facilities. This "External Trigger Mode" activates a custom version of the IRT Characterization Mode when the coordinates of a source are provided from the ground to the onboard computer (Amati et al., 2021).

2.5 THESEUS scientific objectives

The recent results of *JWST* place THESEUS and GRB missions in a scientific competitive position, due to the new questions that are arising regarding galaxy physics and evolution, star formation and cosmology. Therefore, these hot topics need alternative probes, and GRBs are one of the most powerful objects that can be employed for further studies in these domains.

A list of the major scientific goals of THESEUS is now presented to better characterize the important scientific framework in which it will work (e.g., Tanvir et al., 2021; Ciolfi et al., 2021).

SFR(z) from GRB rate
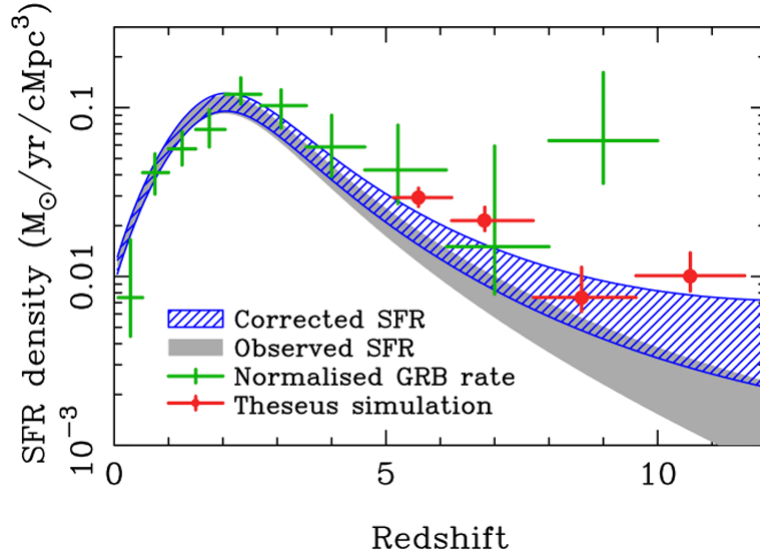
***Figure 2.11:*** *Star-Formation Rate density as a function of redshift, derived from rest-frame UV surveys (shaded curve based on the observed galaxy population, blue hatched region accounts for galaxies below the detection limit) and from GRBs: green points show current constraints from the available GRB sample, red points show corresponding estimates expected from a representative THESEUS sample (Tanvir et al., 2021).*

There is evidence that long GRBs are disfavoured in high-metallicity environments (Fig. 1.13), but it is likely that GRBs are tracing well the majority of massive star-formation beyond $z \sim 3$. Therefore, THESEUS will establish the GRB redshift distribution at $z > 5.5$ much more reliably than previous missions, thanks to a more uniform selection via rapid onboard redshifts measurements. This implies avoiding mass and luminosity selection effects, source of uncertainty in traditional redshift distribution obtained from traditional galaxy observations. However, it is important to mention that recent studies regarding the search of dust-obscured star-forming galaxies at radio wavelengths, lacking of optical counterparts, can contribute to the SFR density at redshift larger than 3 (e.g., Talia et al., 2021). Analyses of this kind have pointed to a higher SFR density at redshifts larger than 6, as shown by simulations of the expected THESEUS representative sample (Fig. 2.11).

Galaxy luminosity function

The intrinsically very small galaxies, which appear to dominate star-formation at $z > 6$, are very hard to detect directly: the faint end of the galaxy luminosity function (LF) is a key issue for our understanding of reionization since it appears that the faint-end of the LF steepens significantly with redshift, reaching a power-law of slope $\alpha \sim 2$ at $z > 6$.

By conducting deep searches for the hosts of GRBs at high-z, we can directly quantify the ratio of star-formation occurring in detectable and undetectable galaxies, with the only assumption that GRB rate is proportional to star-formation rate. Application of this assumption has confirmed that the majority of star-formation at $z > 6$ occurred in galaxies below the effective detection limit of *HST*, with expected magnitudes at the limit of what is reachable with *JWST* and the *ELT*. Since the exact position and redshift of the galaxy is known from the GRB afterglow (from spectroscopic and photometric measurements), follow-up observations to measure the host UV continuum are much more efficient than equivalent deep field searches for Lyman-break galaxies. Imaging of the locations of known GRBs at $z > 6$, obtained when the afterglows had faded, shows that the host galaxy is detected only in a few cases, confirming that the bulk of high-z star-formation is occurring in galaxies below current limits (Fig. 2.12). If the luminosity function is modelled as a Schechter function with a sharp faint-end cut-off, then this analysis allows to constrain that cut-off magnitude, even though the galaxies are too faint to be observed.
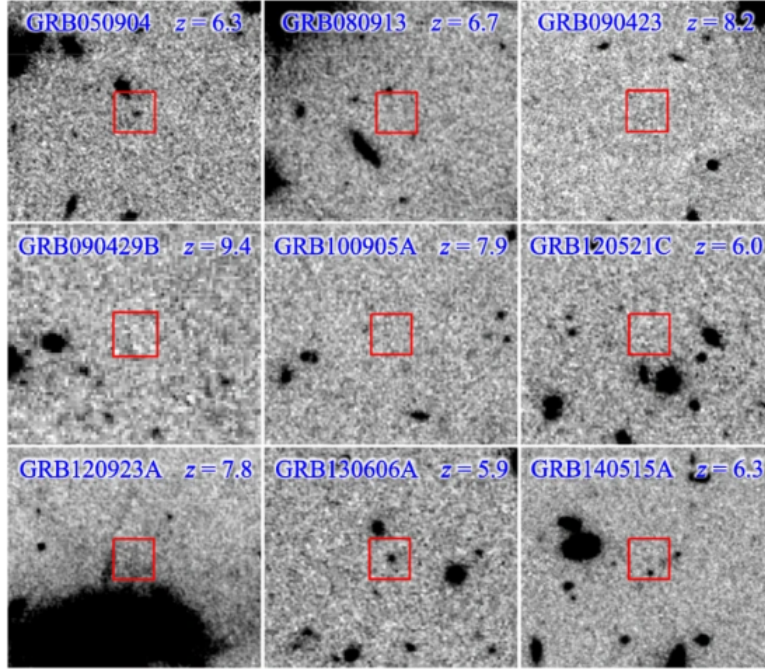
Figure 2.12: *Mosaic of deep HST imaging of the locations of known GRBs at z>6, obtained when the afterglows had faded (red boxes are centered on the GRB locations). The host galaxy is detected only in 2–3 cases, confirming that the bulk of high-z star-formation is occurring in galaxies below current limits. This approach allows us to quantify the contribution of the faint end of the galaxy luminosity function to the star-formation budget, even in the absence of direct detections (Tanvir et al., 2021).*

Metal, molecules and dust

Bright GRB afterglows provide backlights for measuring abundances and gas kinematics of their host galaxies. Thus, they can be used to monitor cosmic metal enrichment and chemical evolution at early times. Follow-up of the brightest afterglows in spectroscopic mode will provide the identification of metal absorption lines and will also enable spectroscopic redshift determinations, which will help refining the photo-z estimates by distinguishing clearly between the GRBs at z > 6 and contaminants from dusty afterglows at lower redshifts. GRBs will help to trace the ISM in galaxies at z > 6, mapping in detail accurate metallicities and abundance patterns across the whole range of star forming galaxies in the early Universe, including those at the very faint end of the LF.

Reionization

The evolution of the IGM from a completely neutral to a fully ionized state is linked to early structure formation. Addressing this phase change to stars leads to the necessity of knowing about how much massive star-formation was occurring as a function of redshift and, on average, what proportion of the ionizing radiation produced by these massive stars escaped from their host galaxies. Both problems will be resolved through THESEUS GRB observations. The former problem relies on the same concepts presented in previous sections. The latter will rely on GRB afterglow spectroscopy, which allows to measure the column density of neutral hydrogen in the host galaxies, thus providing a powerful probe of the opacity of the interstellar medium to extreme UV photons. Future observations of the population of $z > 5$ GRBs detected by THESEUS will provide much more precise constraints on the fraction of ionizing radiation that escaped galaxies during the epoch of reionization.

Moreover, it is expected that reionization should proceed in a patchy way, i.e. ionized bubbles may grow initially around the highest density peaks where the first galaxies form, expanding and ultimately filling the whole IGM. Therefore, the topology of the growing network of ionized regions would reflect the character of the early structure formation and the ionizing radiation field. GRBs themselves do not ionise the surrounding IGM, but previously occurring star-formation in the host galaxy as well as contributions from nearby galaxies will form HII regions. A patchy reionization scenario, which predicts galaxies carving out HII bubbles which later merge, would imply that measurements will vary across a sample of GRBs, so a statistical approach is needed. The IGM neutral fraction can be recovered from follow-up spectroscopy of afterglows.

Population III stars

The very first stars are expected to form from pristine gas at redshift $z \sim 10$-30. Because of the absence of heavy elements and the subsequent inefficiency of cooling at these early cosmic times, their mass is supposed to largely exceed those of Pop I and Pop II stars ($M > 40 \, M_\odot$). When these first stars reach their final stage of evolution, their low-opacity envelope, combined with limited mass loss from stellar winds, may keep large amounts of gas bound until the final collapse, favouring the conditions for jet breakout and for the launch of a very energetic long GRB, detectable up to the highest possible redshifts. The large population of high-redshift GRBs detected by THESEUS offer several routes for searching for these unique events. Given the peculiar energetics and chemistry associated with Pop III star GRBs, their observed properties should differ from GRBs at lower redshift. Their prompt emission could extend over much longer timescales,

similarly, the energy released by the jetted explosion could imply much longer times to dissipate.

Multi-Messenger Astrophysics

Compact binary coalescences (CBCs) represent the most common GW sources and they are expected to emit a variety of bright electromagnetic signals over the entire spectrum, from radio to γ-rays, offering opportunities for a multi-messenger investigation. The first GW detection of a NS-NS coalescence on August 17th 2017, accompanied by the observation of the short GRB170817A, provided a first example of what can be accomplished by combining together all the information. In order to maximise the science return of the multi-messenger investigations during the 2030s, it will be essential to have a facility that can both detect and localize the EM counterpart signals independently from the GW events and, at the same time, rapidly cover with good sensitivity the large compatible sky areas provided by GW detections. Moreover, given the lack of precise knowledge about the properties of various EM counterparts, a large spectral coverage is another essential capability. These combined requirements are fulfilled by THESEUS.

A unique capability of THESEUS is building samples of short GRBs, for which coincident GW observations will be available, allowing unprecedented investigations on the nature of compact binary mergers. Fundamental open questions on the nature of CBC sources and short GRB central engines will be explored by THESEUS, in synergy with the next generation GW interferometers. The main goals that THESEUS is expected to reach are:

- the detection of at least a few to about 10 or more short GRBs associated with GW-detected NS-NS/NS-BH mergers;

- to characterize the time delay between the GW merger epoch and the GRB peak flux, a powerful diagnostic indicator for the jet launching mechanism, capable of highlighting differences between NS-NS and NS-BH systems;

- a combined analysis in presence of a coincident GW detection, shedding light on the nature of the merger remnant;

- to detect and localize several misaligned short GRBs, knowing that the afterglow properties of short GRBs viewed from outside the core of the jet strongly depend on the jet structure;

- to provide information on the r-process element formation accompanying kilonova events: THESEUS accurate sky localization of several NS-NS/NS-BH mergers will allow for kilonova detection and characterization through follow-up observations.

Chapter 3

Characterization of XGIS detection plane

In this Chapter, a detailed description of the XGIS monitor detection element is given, focusing on the technological advantages that such system (characterized by an hybrid Si/CsI(Tl) detector coupled to advanced and specific electronics) can provide for THESEUS space mission.

In particular, we focus on the experimental characterization of the electronics developed for the XGIS detector, studied, optimized and adopted as hard X-ray monitor of the THESEUS mission concept. The characterization of a representative prototype is carried out through both radioactive sources and synthetic electric signals. In particular, I realized experimental tests that concerned the calibration of the electronic processors, functional and performance tests after the introduction of scintillators and an evaluation of the energy resolution. Finally, an environmental test has been performed to evaluate the effect of different values of temperature on the prototype data output.

3.1   XGIS scientific objectives

The main goal of XGIS will be to detect and identify transient sources, characterizing them over an unprecedented wide energy band, thus providing unique clues to their emission physics and mechanism (Section 2.3). The technology developed for making the detection elements will produce a position-sensitive detection plane with a large effective area over a broad energy pass-band (from soft X-rays to soft γ-rays; Labanti et al., 2021).

In order to be suitable for THESEUS scientific objectives, XGIS must satisfy specific requirements, on the basis of the space mission goals outlined in Chapter 2. The scientific requirements of the instrument are reported in Tab. 2.2; the following

ones have been directly tested in this Thesis activity at INAF-OAS Bologna.

- **XGIS science data product** - The mission shall allow to produce the following science data when collecting them: event lists in the given energy range, histograms of X/γ events (images, light curves, and spectra) over reconfigurable bin boundaries, calibration data products.

- **XGIS energy range** - XGIS shall be able to detect photons for science analysis in the energy range between 2 keV and 10 MeV; the effective area at 10 keV, 350 keV and 4 MeV is $\sim$500, $\sim$1050 and $\sim$660 cm^2, respectively.

- **XGIS energy resolution** - The instrument shall have an energy resolution better than 1200 eV FWHM at 6 keV (goal of 300 eV), and less than 6% at 600 keV.

An overview of the technological background within XGIS design and configuration is now needed, to better understand the logic of operation mode and the advantages in using such technologies.

3.2 SISWICH principle and basic components

As described in Chapter 2, the basic detection element of XGIS is composed by two Silicon Drift Detectors and a scintillator bar. This system is paired with electronics to read the carriers coming from the different components of the detection element: the reading of the signal is based on the so called "SISWICH principle", being able to combine the information received by silicon detectors and scintillator. Hence, the following sections are dedicated to an introduction of the physical working principle of the basic components, with particular emphasis on energy range, resolution, timing and noise required by the scientific objectives of THESEUS space mission.

3.2.1 Silicon drift detectors

Solid-state detectors started to be employed as basic detection medium in devices at the beginning of 1960s. Using this technology, better results were achieved in terms of physical size, energy resolution and timing with respect to gaseous detectors (Knoll, 2010).
First of all, compact sizes are achievable due to density values much higher than gaseous medium: high-energy charged particles can provide their full energy in a semiconductor layer of relatively small volume and the production of carriers (electron-hole pairs) requires less amount of energy with respect to the creation of
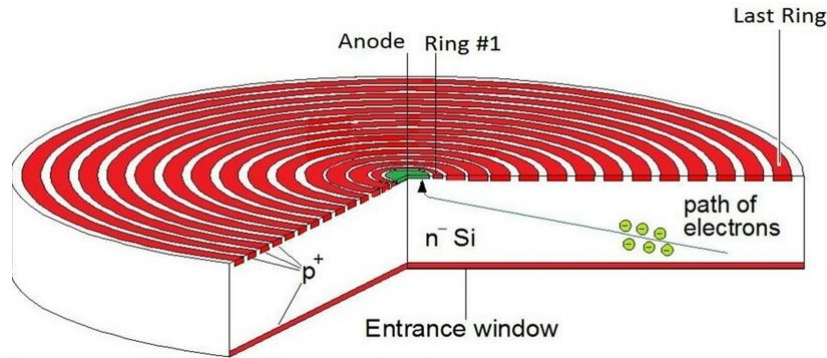
Figure 3.1: *Schematic structure of an SDD. The concentric p$^+$ junction strips are in red (Macchia, 2015).*

the carriers (ions) in a gaseous detector (Castoldi & Guazzoni, 2012). This leads also to a much higher number of carriers for a given incident radiation, improving the energy resolution. Moreover, time resolution benefits from electrons travelling faster in semiconductors than in gas.

In low energy radiation spectroscopy, semiconductor detectors achieve the best energy resolution, so a natural choice for "collecting" X-ray photons through XGIS implied the use of Silicon Drift Detectors (SDDs). In fact, energy and temporal resolution depend on the amplitude of the signal received and on the associated noise, two factors that are dependent on the device. Compared to other photodetectors, SDDs have better efficiency for soft X-rays, a high quantum efficiency for the light for example coming from a scintillator and finally a lower noise associated with the reading of the signal.

The adopted technology was invented by Gatti & Rehak (1984): in their paper, they present a new method for charge transport, where the field responsible for the charge transport is independent of the depletion field.

An SDD is made by a n-type silicon wafer with a concentric strip pattern of p^+ junctions, covering the surfaces of the Si structure (Fig. 3.1). At the centre of the smallest circular strip there is the anode, from which the signal is taken. A voltage is applied across the wafer to deplete the detector, and a second external electric field is superimposed to transport carriers, so particles passing through the detector produce electron-hole pairs which drift toward the electrodes under the influence of the external electric field (Gatti & Rehak, 1984 and Castoldi & Guazzoni, 2012). In this way, a potential "gutter" is formed in the semiconductor volume and is tilted so that the electrons generated by radiation interaction are transported from the position of the generation to the anode (Fig. 3.2).

This configuration allows to have a point anode as an independent component with respect to the surface of the SDD that collects the incident ionizing radiation, ob-
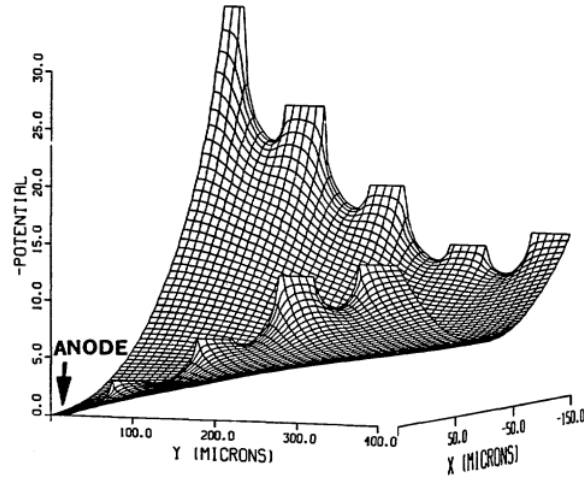
Figure 3.2: *Potential gutter within the SDD. A high negative potential is applied between the external p+ junction strip and the junction near the anode, consequently electrons move (drift) toward the anode (Gatti & Rehak, 1984).*

taining a device with a small capacitance of the anode and, as a consequence, minimizing the effect of the amplifier noise for the total charge measurement (Nicholson, 1974).

The SDDs used for XGIS have been designed and manifactured by Istituto Nazionale di Fisica Nucleare-Trieste (INFN) and Fondazione Bruno Kessler (FBK), a collaboration born with INAF-OAS and many other institutions in the framework of ReDSoX (Research Drift for Soft X-Rays), where research and technological innovations concerning SDDs were born and developed.

The SDDs employed have a square cross section of 5×5 mm^2. In Fig. 3.3 an SDD array 2×2 is shown. The detection plane of XGIS is an SDD array of 8×8 elements, but for electronic and functional tests also smaller arrays can be adopted, due to the modularity of the plane. The anode side (right) is the input side for incident X-ray radiation. Wire bonding connecting the SDD anode and the pre-amplifier are needed for the subsequent elaboration of the signals; the window side (p-side) instead is the input side for the light coming from the scintillator (left).
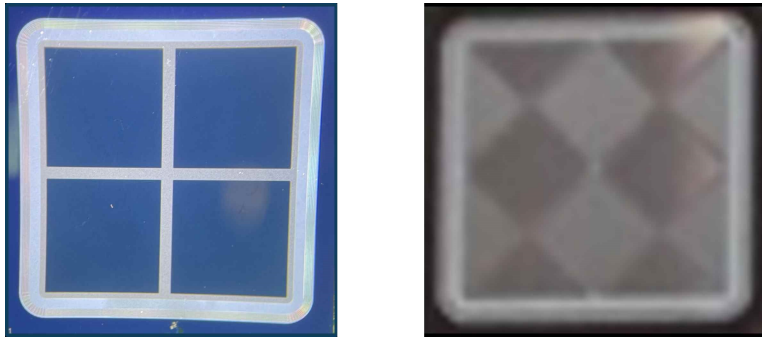
Figure 3.3: *Two sides of the SDD wafer: anodes, input side for scintillation light (left); entrance window, input side for X-ray radiation (right). Wire bonding are visible. Courtesy of FBK.*

3.2.2 Scintillators

As semiconductor devices, scintillation detectors offer a possibility of providing a solid detection medium and are used for measurements of nuclear radiations, particles and photons: they convert the energy of the incident radiation in light, which should reach a photodetector in order to be converted into a signal that can be elaborated. The signal created in a typical radiation interaction is made by electrons (called *photoelectrons*), that usually are no more than a few thousand per MeV (Knoll, 2010). Of fundamental importance is the efficiency to the kind of radiation it needs to detect, in order to choose the right scintillator for each experiment: in the case of XGIS, a γ-ray detector is required to complement the soft X range and should consist of heavy elements, i.e. CsI(Tl), in order to be dense enough to stop as much of the incident photon energy as possible. The detection of γ-ray photons is possible because they undergo an interaction that transfers all or part of their energy to electrons in the absorbing material (Iyudin et al., 2023). Moreover, due to the dependence between resolution and amplitude of the detected signal, the energy resolution is strongly affected by the *Light Output* (*LO*), expressed as the number of scintillation photons per keV of the material.

Detection of γ-rays in scintillators takes place due to three major type of interaction mechanisms with the scintillator material: photoelectric absorption, pair production and Compton scattering.
In the photoelectric absorption process, the γ-ray interacts with an absorbing atom transferring all of its energy to an electron bound in one of the atom shells; it predominates for low energy γ-rays (up to hundreds of keV). For γ-rays with energy larger than 1.02 MeV, twice the rest-mass energy of an electron, the γ-ray interacting with the scintillator material can disappear, being replaced by an electron-positron pair carrying the γ energy exceeding 1.02 MeV; it predominates for high-energy γ-rays (above 5-10 MeV). In the Compton scattering process, the

γ-ray transfers a portion of its energy to an electron of the scintillator material and is deflected from its original path; it is the most probable process over the range of energies between the previous two extremes.

The spectrum for low γ-ray energies (where pair production is not significant) results only from the combined effect of Compton scattering and photoelectric absorption (Fig. 3.4a). The continuum of energies corresponding to Compton scattered electrons is called *Compton continuum*, whereas the narrow peak corresponding to photoelectrons is designated as the *photopeak*. At medium energies, there is the possibility of multiple Compton scattering followed by escape of the final scattered photon (Fig. 3.4d). These multiple events can partially fill in the gap between the Compton edge and the photopeak, as well as distort the shape of the continuum predicted for single scattering (Fig. 3.4b). If the γ-ray energy is high enough to make pair production significant, a more complicated situation prevails (Fig. 3.4c). The annihilation photons now may either escape or undergo further interactions within the detector, leading to either partial or full-energy absorption of either one or both of the annihilation photons. If both annihilation photons escape without interaction, only the electron and positron kinetic energies are deposited (*double escape peak*). Another case is when one annihilation photon escapes but the other is totally absorbed. These events contribute to a single escape peak, which now appears in the spectrum at an energy of 0.511 MeV, below the photopeak. A continuous range of other possibilities exists in which one or both of the annihilation photons are partially converted to electron energy through Compton scattering and subsequent escape of the scattered photon. Such events accumulate in a broad continuum in the pulse height spectrum lying between the double escape peak and the photopeak (Knoll, 2010).
Hence, all of these kind of spectral features are related to physical interaction occurring between photons and scintillator material, as shown in Fig. 3.4d.

The assembly of a scintillator-based detector should ensure the optimal collection of the scintillation light in the photodetector, i.e. the SDDs. To improve light transmission, a scintillator may be treated, polished or slightly roughened. Typically, it is surrounded by a light reflective, or diffusive material on all sides apart from the side coupled to the photodetector. In the optical coupling, the light transfer is maximized using a transparent medium (epoxy or silicone), which adapts to the refraction indices of the different media. In space applications, the choice of the materials should take into account also other requirements, such as thermal expansion, lifetime (ageing or yellowing), outgassing in vacuum, hygroscopic properties, weight and costs (Iyudin et al., 2023).
The scintillator bars used are made of CsI(Tl) with a square section of 4.5×4.5 mm^2 and 3 cm long. They are polished on the sides in contact with the SDDs and rough on the other surfaces. The bars are all individually wrapped by INAF-OAS
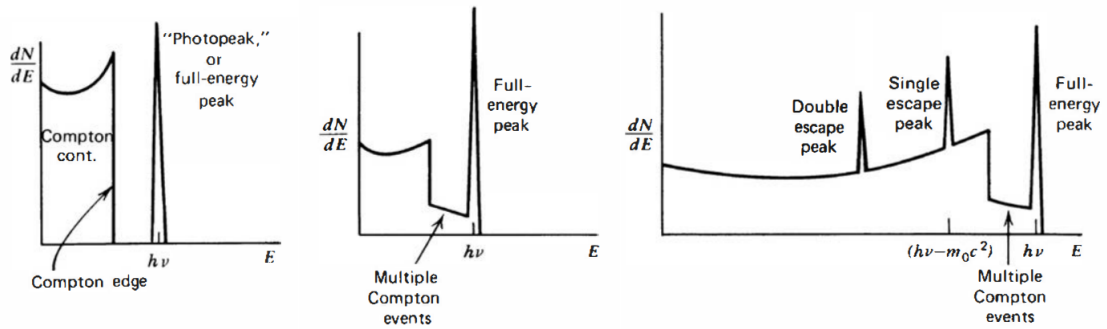
(a) *The processes of photoelectric absorption and single Compton scattering give rise to the low-energy spectrum.*

(b) *In addition to the continuum from single Compton scattering and the full-energy peak, the spectrum at medium energies shows the influence of multiple Compton events.*

(c) *The single escape peak corresponds to initial pair production interactions in which only one annihilation photon leaves the detector without further interaction. A double escape peak will also be present due to those pair production events in which both annihilation photons escape.*
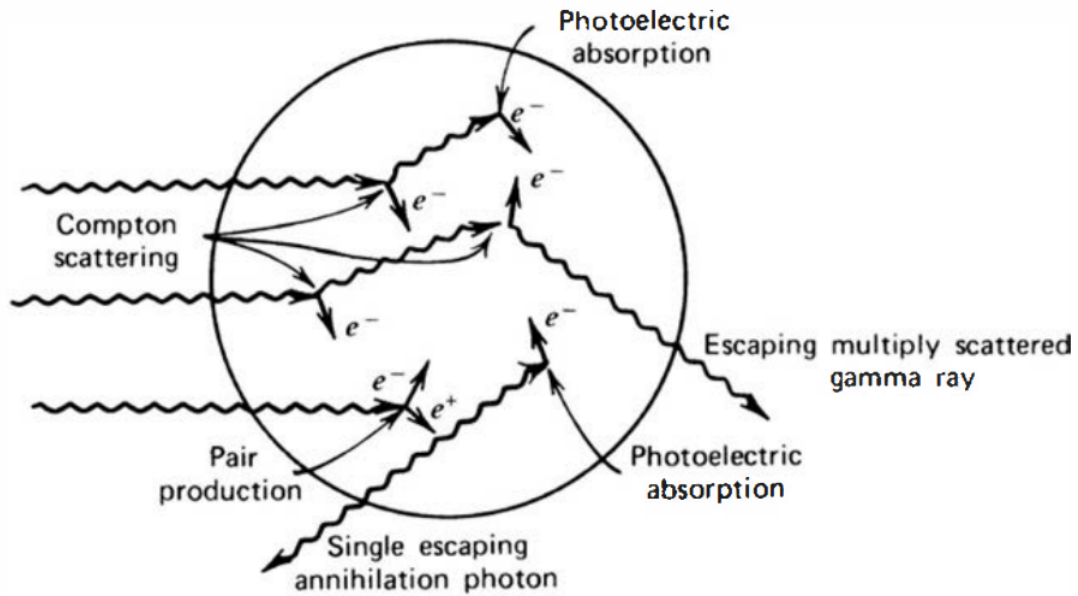
(d) *Representation of the possible interactions between γ-ray photons and scintillator material.*

Figure 3.4: *Representation of spectra for low, medium and high γ-energy photons in Fig. 3.4a, 3.4b and 3.4c, with respective physical interactions in Fig. 3.4d (Knoll, 2010).*

on all sides except for the SDD coupled ones. This will guide the scintillation light into the photodetector, through an optical coupling to SDDs made by transparent and flexible silicone pad, less than 1 mm thick.

3.2.3   SISWICH principle

A γ-ray detector based on a CsI(Tl) scintillating crystal coupled to a silicon photodetector is also a direct X-ray detector, for radiation interacting in silicon, allowing a simultaneous X and γ-ray detection with a single, compact device. Since the energy threshold and the spectroscopic capabilities of such detector are dominated by the electronic noise of the photodetector, it was decided to use a SDD because of its much lower intrinsic electronic noise (Section 3.2.1). This kind of detector could find application in space-based High-Energy Astrophysics instruments due to its compactness being a valuable solution to fulfill the strict weight and volume constraints of space missions (Marisaldi et al., 2005).

The main idea at the basis of SISWICH principle (a name self explanatory if translated into "Silicon Sandwich", Fig. 3.5) consists into coupling two SDDs, one on top and one on bottom of a CsI(Tl) scintillator bar, producing the single detection element, the pixel. Each pixel operates in a combination of direct conversion for low energy X photons (2 - 30 keV) and indirect conversion for hard X-ray and γ-ray photons (20 keV - 10 MeV). The incident low-energy photons, coming from the top entrance window, will be absorbed and detected by the top SDD. Above $\sim$30 keV, photons pass through the top SDD, reaching the scintillator crystal, whose scintillation light travels toward both SDDs: the energy released by the photons into the bar can be calculated summing the two signals measured on top and bottom SDDs. It is important to remember that interactions in silicon and in CsI(Tl) needs different amount of energy to produce a charge, 3.65 eV/e$^-$ and 70 eV/e$^-$ (collected by one SDD) respectively, so discrimination of the place of interaction is necessary to obtain the correct energy (Mele et al., 2021). Signals produced in Si or in CsI(Tl) thus have different amplitudes, but also different temporal characteristics. In fact, charge pulses either from X-ray interaction in silicon or scintillation light collection are quite different in shape, due to the different timing properties. While the electron-hole pair creation from X-ray interaction in silicon originates a fast signal (about 10 ns rise time), the scintillation light collection is dominated by the fluorescence states de-excitation time, and a few μs shaping time is needed in this case to avoid significant ballistic deficit (Marisaldi et al., 2005). In order to optimize the signal to noise ratio, the processing of the two signals will take into account their different characteristics, a topic further discussed in next section.
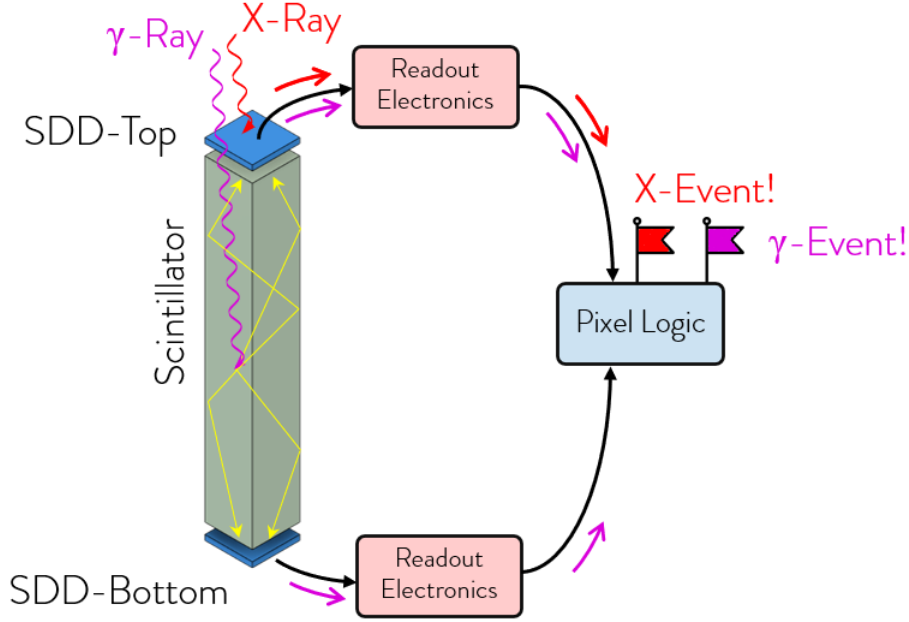
Figure 3.5: *Schematic view of an XGIS pixel, composed by two SDDs and a CsI(Tl) crystal bar. The event is processed by the Readout Electronics, ORION-FE, and a single multichannel processor for the event identification, ORION-BE. Image taken from Mele et al. (2021).*

3.3 ORION IV architecture

With the realization of a first demonstration model of XGIS module, an application specific multi-chip readout electronics designed for spectrometry, named ORION, has been developed by Politecnico di Milano and Università di Pavia, following the specifications given by INAF-OAS team. Several prototypes of ORION have been produced, increasing level of complexity and completeness. The current version is ORION IV. The purpose of the demonstration module was to test the functionality of the detector, determine its characteristics and performances, in order to suggest further modifications and improvements.

ORION IV must be capable of distinguish between a direct detection of X-rays on the top SDD and the indirect detection of γ-rays on the crystal. For a direct detection of an X event, the ASIC must read and properly elaborate the signal coming from a single pixel, producing a well defined signal shape and peaking time leading to minimum noise, in order to take advantage of the high energy resolution capabilities provided by SDDs. Instead, for an indirect detection of a γ event, the ASIC readout electronics must be able to combine the charge signals from top and bottom SDDs, to ensure a longer peaking time to avoid ballistic deficit in charge collection, to have a low noise performance even though CsI(Tl) surely limits the

spectroscopic resolution.

The different nature of the two signals requires two mechanisms of discrimination: for an X event, the discriminator is applied only to signal coming from the top SDD, instead for a γ event the discriminator should be applied to the sum of signals coming from top and bottom SDDs.

The XGIS electronics has been developed taking into account a specific requirement: the separation between a small Front-End (ORION-FE) and a Back-End (ORION-BE), which will process in parallel the information coming from the SDDs, generate event triggers and convert the analog signal into a digital one (Fig. 3.6, Mele et al., 2021).

The SDDs have been mounted on a dedicated PCB and their ORION-FE chips (one for each SDD) are placed on small ribs on a FE-PCB (Fig. 2.7a): in fact, SDD should not be shadowed by other materials that could block X events, so the electronics should be as small as possible. The ORION-FE represents the first stage of the electronic chain, i.e. the analog low-noise pre-amplifiers, placed near the detection element to minimize the parasitic capacitance due to the interconnection between the sensor and the charge amplifier, and so the noise (Grassi et al., 2022). The ORION-BE is placed ~5 cm away from the ORION-FE chips, out of the sensitive area of the detector (Mele et al., 2021). It comprehends all the analog and digital signal processing circuits, including the ADC modules, the smart logic for event type extraction and timing assignment (Grassi et al., 2022).

The laboratory test board used is composed by 4 pixels, for a total of 8 SDDs, 4 scintillator bars, 8 ORION-FE and 1 ORION-BE, that includes 4 identical chains for processing the 4 pixel signals.

The ORION-FE provides the pre-amplification and processing of the charge signal coming from top and bottom SDDs, then a shaping current conveyor shapes the signal and allows a clean transmission to dedicated current receivers on the ORION-BE some cm away.

In ORION-BE the circuitry serving one pixel is composed by three independent branches, respectively X, γ-Top and γ-Bottom, that operate in parallel: the first two elaborate the signal from the SDD on the top of the pixel, while the last one processes the signal coming from the SDD on the bottom of the pixel.

In each branch, the signals are amplified and shaped, then compared in amplitude by discriminators, different for X and γ, with a threshold level set above the noise level of the circuits. In the X branch, the shaping time of the processor is set to 1 μs, since an X photon directly absorbed by the SDD silicon generates a fast signal. In the γ branch, the shaping time of the processor is set to 3 μs, since scintillators generate a slower and dispersed charge collection. X and γ branches have two different gains (Grassi et al., 2022).

A further peak detector circuit flags the signal peaks by generating a trigger,
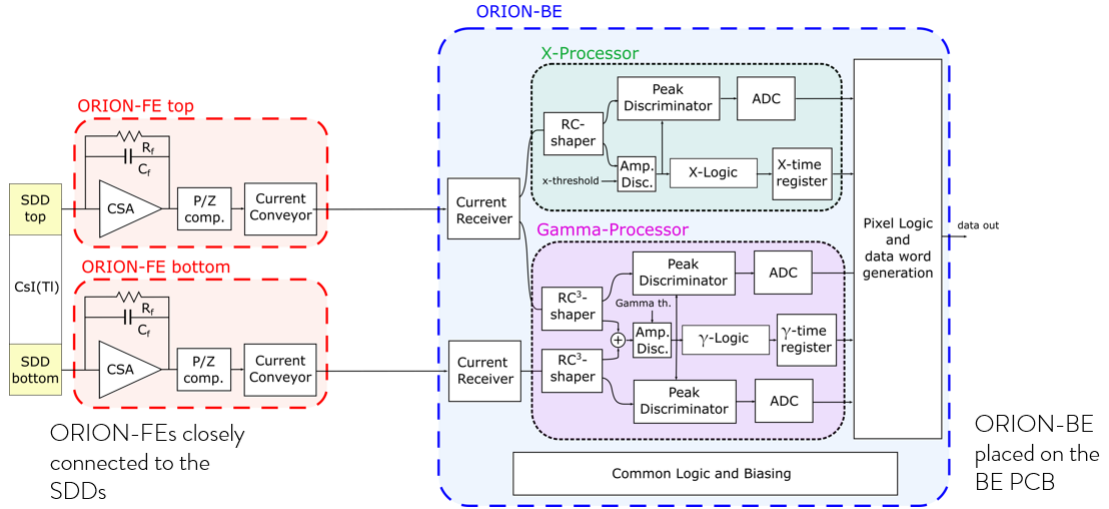
Figure 3.6: *Block diagram of ORION IV electronics and logic for a single pixel, separated into ORION-FE and ORION-BE (Mele et al., 2021).*

that is used both to assign a unique time-stamp to the event and to command the stretching of the signal peak levels. The ASIC holds the three values registered at the peak amplitude in order to let the 16 bit ADC to acquire the analog information and convert them into Analog Digital Units (ADU).

At the end of the whole process, the ASIC gives in output an End Of Conversion flag (EOC) and is then ready to transmit his digital data. After receiving a 'RESTART' command, it is ready for new acquisitions.

For each detected event, ORION IV provides a digital data word made by 64 bits, containing the information on position (i.e. pixel), timing, event type and energy (Mele et al., 2021):

- bit(0) ÷ bit(15) = Bottom SDD ADC

- bit(16) ÷ bit(31) = Top SDD ADC

- bit(32) = Flag γ/X event (1 for γ, 0 for X)

- bit(33) = Flag Trigger γ (1 if True)

- bit(34) = Flag Trigger X (1 if True)

- bit(35) ÷ bit(37) = Pixel Address

- bit(38) ÷ bit(61) = Time

- bit(62) ÷ bit(63) = Spare

52

Figure 3.7: *Left: shaping mode. Right: stretching mode. In both figures, triggers for X and γ events are shown.*

It should be noticed that the output digital word includes the Bottom ADC and the Top ADC bits, where a dedicated logic inside ORION IV determines what these information represent. In the case of an X event, Top-ADC is the ADU of the X branch and Bottom-ADC is 0, whilst in the case of a γ event, Top-ADC is the ADU of the γ-Top branch and Bottom-ADC is the ADU of the γ-Bottom branch. On the basis of the value of the ratio of γ-Top ADU and γ-Bottom ADU, it is possible to logically distinguish between X and γ events.

By configuring the ORION-BE, it is possible to work in two different modes: *shaping mode* and *stretching mode* (Fig. 3.7).

In shaping mode, the pulse discriminator, the peak detector and the trigger logic are disabled, and the output signals of the X and γ shapers are directly routed to the output buffer. In stretching mode, the pulse discriminator, the peak detector and trigger logic are enabled, and the internal stretched output signals, i.e. the ADC input signal, are also routed to the output buffers (Mele et al., 2021).

It is important to mention that the discriminators responsible for the generation of the internal trigger and the starting of acquisition operations are crucial elements. Currently, the two discriminator blocks, one for each branch, compare their signal with the same selectable threshold level. Since the first test of the ASIC, it was clear that this is the major problem of the actual design of ORION-BE IV, due to difference in gains between the X and γ branches. The different gain accounts for the different ranges of the two branches, 2-40 keV for X events detected in the SDD (i.e. signals spanning from about 500 to 11000 e$^-$) and 30-5000 keV for γ events detected in the scintillator (i.e. signals spanning from about 500 to 75000 e$^-$).

The X branch has a gain ∼10 times higher than the γ branch, thus the common threshold level, which is correct for detecting X events, results in a very high threshold for γ events, due to their much lower amplitude.

3.4 Experimental characterization of ORION IV

Tests on the prototype (made by only 4 pixels, i.e. detection elements) cannot exclude tests on the functioning of the ASIC, so in this section a series of experimental tests done on ORION IV demonstration module are presented. Testing the ASIC is important in terms of expected performance from the detector: a deep knowledge of the limits of the constituents and of the logic is fundamental to set the boundaries on what requirement are achievable and what are not achievable with the current system, keeping in mind the scientific objectives outlined in Chapter 2 for THESEUS mission and in Section 3.1 specifically for XGIS.

The following tests include the use of radioactive sources and voltage impulses to specifically test the ORION-BE. The performance of SDDs and ORION-FE have already been tested (Mele et al., 2021); this system is the most sensible part for what concern the signal/noise, thus it characterizes the whole ORION (FE and BE) performance. Moreover, preliminary tests on a first prototype of ORION-BE (ORION-BE I) have been made (Borciani, 2023 and Srivastava et al., 2023).
In this Thesis, detailed tests of ORION-BE IV operations are presented and scintillator bars have been introduced for the first time, allowing functionality and performance tests of the reduced prototype detector.

3.4.1 Test Equipment

In Fig. 3.8 the detection unit prototype with 4 pixels and without scintillation elements is presented. The electronic components of the ASIC are not visible, as well as the pins for the electric connection with the Test Equipment (TE, Fig. 3.9), that allows the correct functioning of the module and its logical blocks.
One low-power supply (*Digimess PN300*) is needed for the alimentation of the entire board and a high-power supply (*AimTTi PLH250*) is needed for the polarization of the silicon wafers. A *National Instruments NI-USB-6351* multifunction I/O board is connected to the ASIC and through a *LabView* software interface it is possible to configure ORION IV and command the data acquisition (Fig. 3.10). An oscilloscope (*Tektronix TDS3012B*) can be connected to the ORION-BE output pin to check the signals related to detected events. The events can be produced both by radioactive sources or test impulses generated by a pulser (*Tektronix AFG1062*), supplying also the clock regulating the acquisition.
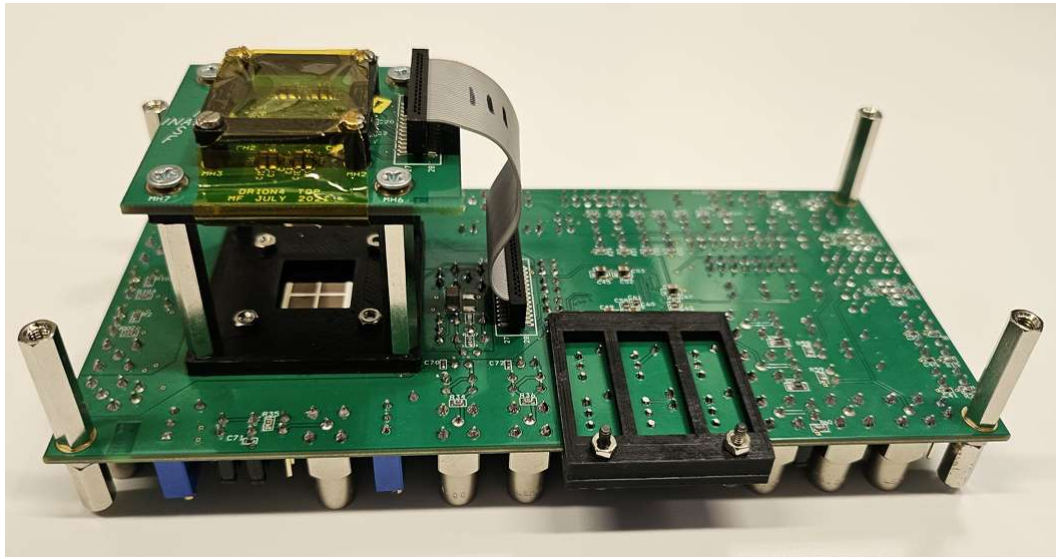
Figure 3.8: *XGIS demonstration module: on the bottom of the board a 2 × 2 SDD array is clearly visible, showing the side that will be optically coupled to 4 scintillator bars (light input side); on the upper board, another SDD array is present, with the input window for the scintillator light facing the bottom one and the window for the incident radiation on the opposite side. Scintillator bars have not been introduced yet.*
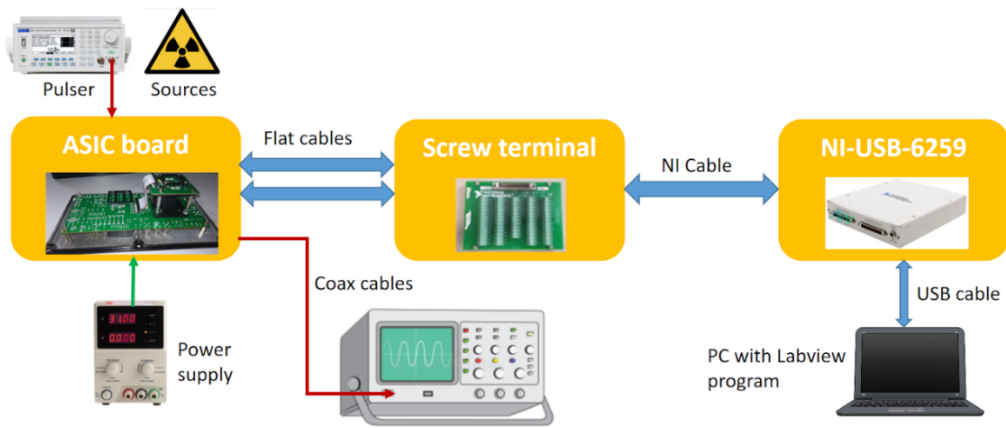
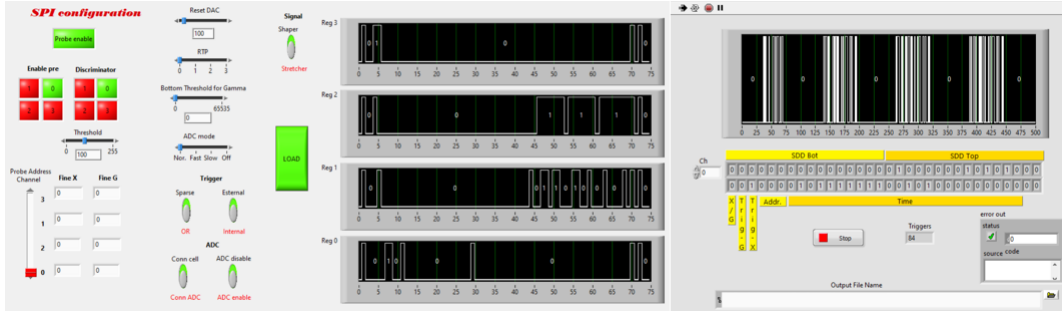**Figure 3.9:** *Test Equipment setup. Courtesy of Claudio Labanti.*

Figure 3.10: *Panel of control for ASIC configuration (left) and data acquisition panel (right).*

3.4.2 Calibration of X and γ branch

Calibration is of fundamental importance to correctly interpret the outputs of new devices. In the case of XGIS demonstration module, it allows us to find a one to one relation between the output measurements from the ORION-BE ADC (*channels*) and well known quantities, which are the spectral lines emitted at specific energies by radioactive sources. Thus the calibration of the prototype is in terms of energy. The radioactive sources chosen for calibration were ^{55}Fe, emitting spectral lines at [5.9, 6.5] keV, and ^{241}Am, emitting at [11.9, 13.9, 16.8, 17.7, 20.7, 26.3, 59.5] keV. The calibration consisted of exposing the demonstration module to source radiation and acquire the events. Each acquisition lasted ~30-40 minutes and was done enabling the stretching mode, implying the use of the digital part in ORION-BE, producing a digital output data word.

The calibration was performed for both X and γ branch: dedicated methods are further discussed in next sections. At this stage, the prototype does not include scintillator crystals, but SDDs produce charge both from incident X radiation and from collecting the scintillator light, so the γ branch calibration is possible through stimulation of the pixels by low-energy radiation on the SDD or by electric impulse and a subsequent estimation of how much charge CsI(Tl) typically produces.

Several data acquisitions have been done using different setups, as enabling one Pixel at time or enabling multiple Pixels simultaneously. The end result was that, from an initial analysis of the raw data, enabling only Pixel 0 was the most reliable configuration. Pixel 1, 2 and 3 were progressively more noisy and presented unpredictable behaviours: this problem may be addressed to the internal logic of the multi-channel, because most of the logical blocks are asynchronous and may suffer from glitches of other pixel-channels.

Hence, every acquisition further taken, analyzed and discussed in this Thesis is referred only to Pixel 0 enabled.

3.4.3 X branch calibration with radioactive sources

The ^{241}Am source was put in front of the Top SDDs of the demonstration module, mimicking the arrival of X-photons as in the spacecraft configuration of XGIS.

After the acquisition of X events, a multichannel spectrum of the signals processed by the X branch was plotted using the `MESCAL` pipeline (Dilillo et al., 2024): the software analyzes the raw data expressed in Analog Digital Units, counts how many occurrences an ORION-BE channel registered and produces a histogram. The transformation of the histogram into a physical spectrum is obtained through the calibration that `MESCAL` automatically performs. In fact, it is able to recognise each emission line (assigning its corresponding energy), fit it with a Gaussian model, extract the parameters of the fit (centroid, FWHM and amplitude with respective errors calculated at 1σ) and obtain an experimental relation between ADU and keV.

For this acquisition, the extracted peaks parameters, before calibration, are summarized in Tab. 3.1. The 59.5 keV emission line was not considered because in this section the focus is just on the X branch calibration (60 keV are already in γ-ray energy band).

Table 3.1: *Gaussian fit parameters for each detected emission line of ^{241}Am. The parameters are expressed in Analog Digital Units because they are extracted before the calibration.*

Emission line (keV)	Centroids (ADU)	FWHM (ADU)	Amplitude (ADU)
11.9	814.4 ± 0.5	15.4 ± 1.5	1032 ± 83
13.9	868.5 ± 0.1	11.8 ± 0.3	6948 ± 161
16.8	946.5 ± 0.4	15.4 ± 1.5	2979 ± 231
17.7	967.4 ± 0.2	13.0 ± 0.5	6442 ± 191
20.7	1046.6 ± 0.3	15.8 ± 0.9	1351 ± 70
26.3	1187.0 ± 0.3	11.2 ± 0.9	480 ± 32

For the proper calibration, a linear relation between channels and energy (E) was assumed:
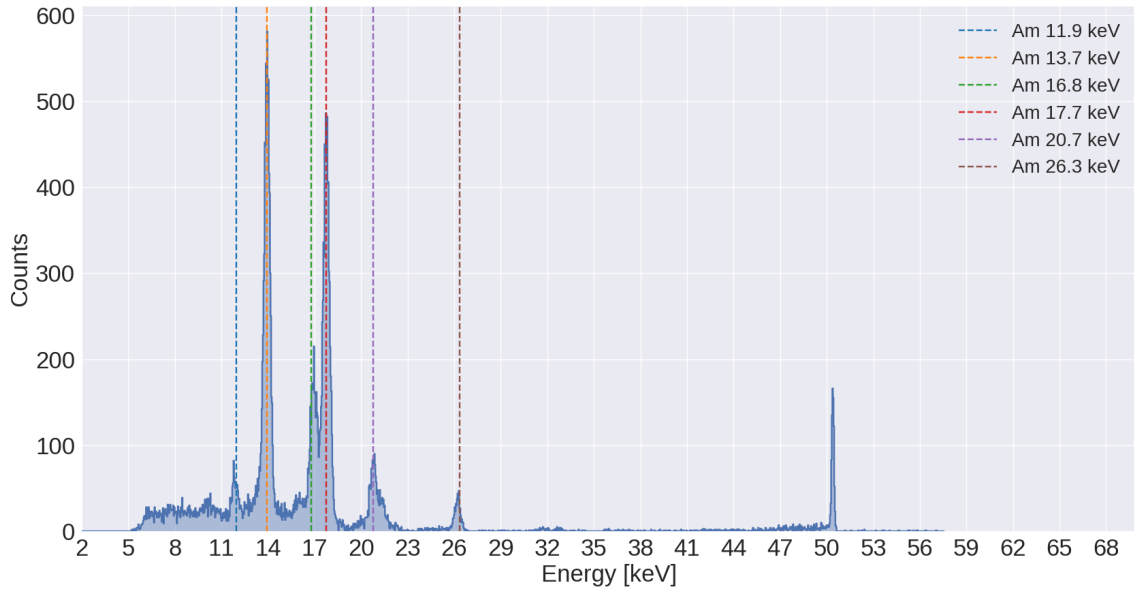
$$Centroid \; [\text{ADU}] = Gain \cdot E + Offset \tag{3.1}$$

$Gain$ and $Offset$ values were extracted from minimizing the linear relation, a task automatically performed by `MESCAL`:
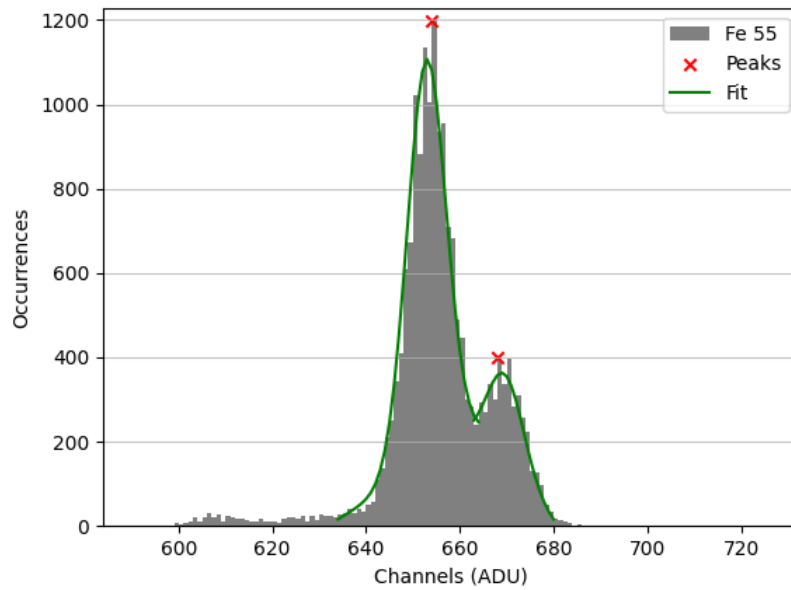
$$Gain = (25, 9 \pm 0, 3) \; \text{ADU/keV} \tag{3.2a}$$

$$Offset = (507 \pm 5) \; \text{ADU} \tag{3.2b}$$

These are the relevant parameters for the calibration, able to produce the ^{241}Am spectrum, presented in Fig. 3.11.

Figure 3.11: *Multichannel spectrum of ^{241}Am produced with* `MESCAL`. *Acquisition done setting only Pixel 0 enabled.*

Figure 3.12: *Multichannel spectrum of ^{55}Fe, not calibrated in energy. Acquisition done setting only Pixel 0 enabled.*

Also a spectrum of ^{55}Fe was plotted, this time without `MESCAL`. As already mentioned, the latter software purpose is mainly calibration and so it presents the requirement of at least three emission lines in order to analyze the raw data. ^{55}Fe has only two spectral lines, so the data analysis was not possible with `MESCAL`. However, the events acquired were similarly plotted in a histogram (Fig. 3.12) and the peaks fitted using a composite model (Gaussian + Linear). Then, the fit parameters for each peak were extracted (Tab. 3.2). The validity of the ^{241}Am source calibration was confirmed using also the emission line of the Iron spectrum.

Table 3.2: *Gaussian fit parameters for each detected emission line of ^{55}Fe. The parameters are expressed in Analog Digital Units because they are extracted before the calibration.*

Emission line (keV)	Centroids (ADU)	FWHM (ADU)	Amplitude (ADU)
5.9	652.9 ± 0.2	9.8 ± 0.6	10054 ± 794
6.5	669.7 ± 0.7	9 ± 3	2388 ± 1300

### 3.4.4 X branch calibration with electric impulses

From the values of *Gain* and *Offset* (eqs. 3.2), it is possible to extend the calibration to a continuous range of energies by using electric impulses. The input impulses were generated by a pulser and their amplitude voltage was chosen to be compatible with the data processing from the X branch only: the voltages applied to the ORION-FE were [15, 30, 45, 60, 75] mV. In fact, charges can be injected through a small test capacitance on ORION-FE; when injecting charge through test impulses, the SDD needs to be polarized in order to have a functioning FE and to acquire under realistic conditions by introducing also electric noise from the SDD. One acquisition of $\sim$1 minute was done for each test impulse, then the corresponding digital output words were examined and plotted in form of histogram (Fig. 3.13).

The peaks generated by the test impulses were fitted and their fit parameters extracted, as for the calibration sources (Section 3.4.3). By using the inverse calibration linear relation (eq. 3.1)

$$E \text{ [keV]} = (Centroid - Offset)/Gain \;, \tag{3.3}$$

at each impulse can be associated an energy value. In Tab. 3.3 the parameters of each peak are listed, showing also the corresponding energy values.
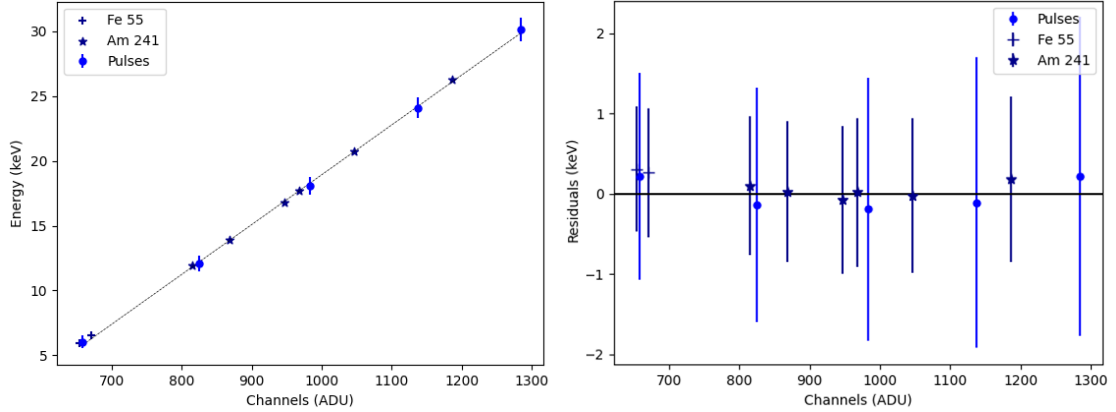
To validate the calibration in energy carried out using the radioactive sources, a linear fit including also the test impulses was done (Fig 3.14). The fitting gives also information about the linearity of the system, which is enclosed between $\pm 1\%$ of the operative range.
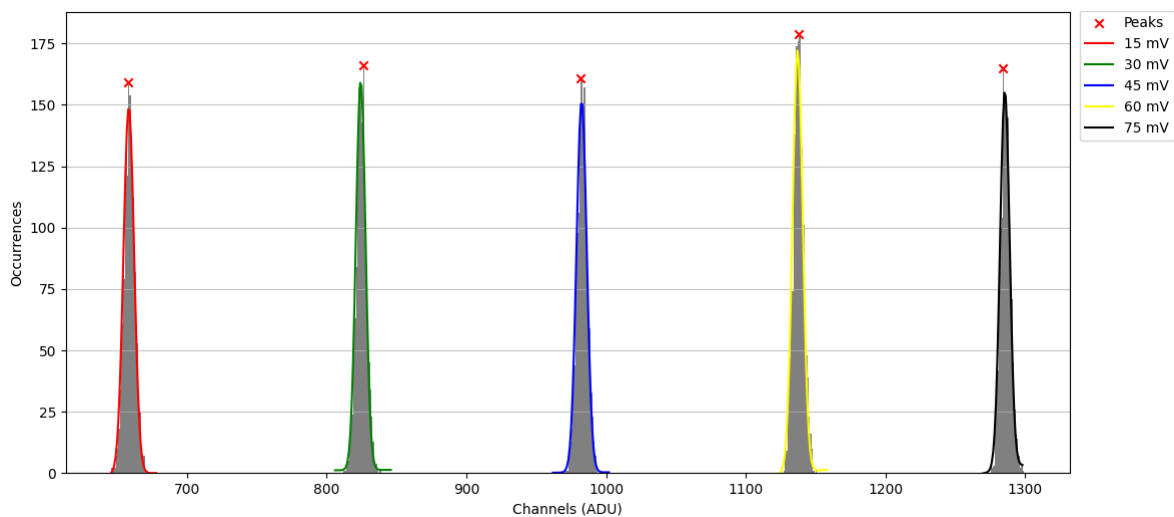
Figure 3.13: *Peaks produced by test impulses of different amplitude and processed by the X branch (only Pixel 0 enabled). The plot is not calibrated in energy.*

Table 3.3: *Gaussian fit parameters for each test impulse and corresponding energy values, calculated as in eq. 3.3. The parameters are expressed in Analog Digital Units because they are extracted before the calibration.*

Test Impulse (mV)	Centroids (ADU)	FWHM (ADU)	Amplitude (ADU)	Energy (keV)
15	658.44 ± 0.17	8.9 ± 0.6	1413 ± 165	5.8 ± 0.3
30	824.41 ± 0.09	8.1 ± 0.2	1362 ± 40	12.2 ± 0.3
45	982.50 ± 0.08	8.6 ± 0.2	1389 ± 34	18.3 ± 0.4
60	1137.06 ± 0.09	8.6 ± 0.2	1578 ± 47	24.3 ± 0.4
75	1285.37 ± 0.10	8.0 ± 0.4	1309 ± 88	30.0 ± 0.5

(a) *Calibration in energy for radioactive sources* **(b)** *Residuals of the linear regression for each* (^{241}Am *and* ^{55}Fe) *and test impulses.* *point of the calibration plot.*

Figure 3.14: *Linear regression (left panel) and residuals (right panel), validating the calibration in energy for the X branch. Plots valid for Pixel 0 only.*

ORION-FE test capacitance

From the test impulse acquisitions, the test capacitance of the ORION-FE of Pixel 0 Top SDD has been calculated.

The capacity C is calculated starting from its physical definition: $C = Q/V$, where Q is the charge collected and V the voltage. V is addressed to the voltage amplitudes of the test impulses shown in Tab. 3.3. Q instead is calculated starting from the energy values associated to the test impulses, recalling that photon interactions in silicon produce one electron for each 3.65 eV deposited (Section 3.2.3). Thus, the amount of electrons (n_e) and the total charge (Q) are derived for each pulse:

$$n_e = \frac{E \cdot 10^3}{3.65} \qquad ; \qquad Q = n_e \cdot e , \qquad (3.4)$$

where $e = 1.602 \cdot 10^{-19}$ C. To obtain a unique value for the capacitance, the mean of the capacities calculated for each pulse has been done, obtaining a value of

$$C = (17.6 \pm 0.3) \text{ fF}, \qquad (3.5)$$

compatible with the requirement for high-resolution spectroscopy.

The capacitance value is necessary also to calibrate the γ branch.

3.4.5 γ branch calibration

γ branch calibration cannot follow the same method described in Section 3.4.3. By using the previous radioactive sources, it is evident that only ^{241}Am emits a

spectral line in the γ-ray energy band. Therefore, a calibration in energy using `Mescal` and a unique spectral line of energy $E = 59.5$ keV is not possible.

In Section 3.4.4, a method to validate the calibration with electric impulses was explained, but it implied the knowledge of $Gain$ and $Offset$ (eq. 3.2) for a direct conversion of voltage into energy. The last thing calculated was the test capacitance for the Top SDD and starting from that result the γ branch energy calibration is tackled. In fact, the knowledge of the capacity, coupled to test impulses of adequate amplitude voltages (to activate data processing of the γ branch), gives a direct measurement of the charges created in the simulated interaction within the scintillator bar, that are then read by the Top and Bottom SDDs. It is important to remember that during this test no scintillator bar was present in the demonstration module. The calibration of the γ branch was done assuming a Light Output value of 15 e$^-$/keV, which means that for each keV deposited in the scintillator, 15 photoelectrons are produced and reach the SSDs. This value of Light Output has been verified later in Section 3.4.10. Hence, two calibrations have been done, one for γ-Top and the other for γ-Bottom branch.

3.4.6 γ-Top branch calibration

From the definition of capacity ($C = Q/V$), it is possible to calibrate in energy, passing through the charge created in the interaction with the simulated scintillator bar of Pixel 0.

For the Top SDD, the test capacitance has already been calculated in eq. 3.5, while the applied test impulses had voltage amplitudes of [50, 150, 250, 350, 450, 550, 650, 750] mV. Q is then directly obtained by multiplying C to each voltage amplitude. The charge is then expressed in equivalent number of electrons (n_e) and finally the energy is calculated as $E = n_e/LO$.

To find the linear relation between ORION-BE channels and energy, one acquisition of ∼1 minute was done for each test impulse, with only Pixel 0 enabled. Then the corresponding digital output words were plotted as a histogram (Fig. 3.15). As previously explained, the peaks generated by the test impulses were fitted and their fit parameters extracted. In Tab. 3.4, the conversion from pulses to energy is presented, as well as the peak parameters. The energy range is significantly different from the one of X branch, as required and expected.

To find the calibration parameters for the γ-Top branch, a linear regression has been done and plotted in Fig. 3.16. In this plot, it was introduced also the 60 keV peak of ^{241}Am: its parameters were obtained from the analysis of an acquisition.

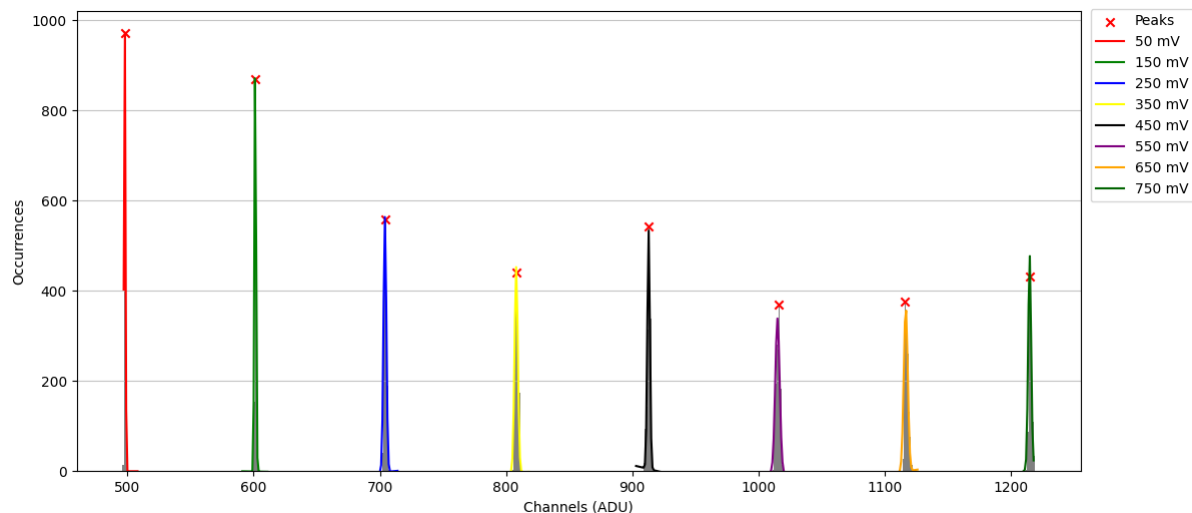From the linear fit $Gain$ and $Offset$ have been obtained:

$$Gain = (391 \pm 1) \text{ eV/ADU} \tag{3.6a}$$

$$Offset = (-174.8 \pm 1.1) \text{ keV} \tag{3.6b}$$

The different units with respect to eq. 3.2 are due to the different process done for calibrating. In this case the fit obey the following law:

$$E = Gain \cdot Centroid + Offset \tag{3.7}$$

Figure 3.15: *Peaks produced by test impulses of different amplitude and processed by the γ-Top branch (only Pixel 0 enabled). The plot is not calibrated in energy.*

Table 3.4: *Conversion from voltage amplitudes of the input impulses to energy and fit parameters obtained from data processing of γ-Top branch.*

Test Impulse (mV)	n_e	Energy (MeV)	Centroids (ADU)	FWHM (ADU)	Amplitude (ADU)
50	5500	0.4	$\sim$498	$\sim$1.4	1521.9 ± 0.1
150	16500	1.1	$\sim$601	1.56 ± 0.01	1568 ± 9
250	27500	1.8	704.01 ± 0.06	2.66 ± 0.15	1600 ± 88
350	38500	2.6	808.01 ± 0.04	3.07 ± 0.11	1487 ± 52
450	49500	3.3	912.95 ± 0.06	2.4 ± 0.15	1353 ± 83
550	60500	4.0	1015.03 ± 0.14	4.1 ± 0.4	1494 ± 133
650	71500	4.8	1116.68 ± 0.09	3.7 ± 0.2	1439 ± 95
750	82500	5.5	1214.85 ± 0.09	2.7 ± 0.3	1380 ± 161
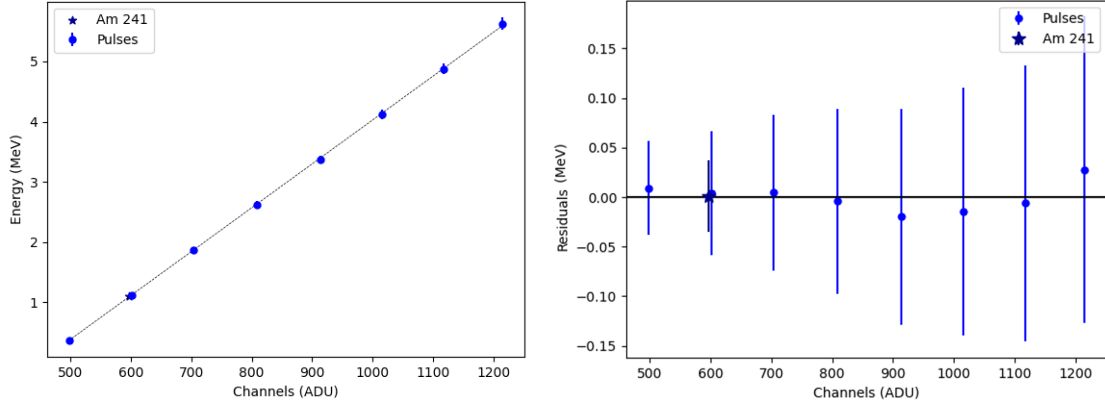
(a) *Calibration in energy for test impulses and* ^{241}Am *60 keV emission line, expressed as MeV equivalent energy from CsI(Tl) charge production.*

(b) *Residuals of the linear regression for each point of the calibration plot.*

Figure 3.16: *Linear regression (left panel) and residuals (right panel) for the calibration in energy of the γ-Top branch. Plots valid for Pixel 0 only.*

### 3.4.7 γ-Bottom branch calibration

The calibration of γ-Bottom branch follows the same method of the γ-Top one, so only the main results will be presented: the table with the peak parameters (Tab. 3.5), the uncalibrated histogram (Fig. 3.17) and the calibration plot (Fig. 3.18), as well as the values for $Gain$ and $Offset$:

$$Gain = (0.413 \pm 0.002) \text{ eV/ADU} \tag{3.8a}$$

$$Offset = (-188.9 \pm 1.7) \text{ keV} \tag{3.8b}$$

It is important to mention that it was not possible to measure the test capacitance for the Bottom SDD, therefore the same value of capacitance of Top SDD was assumed (eq. 3.5).

64
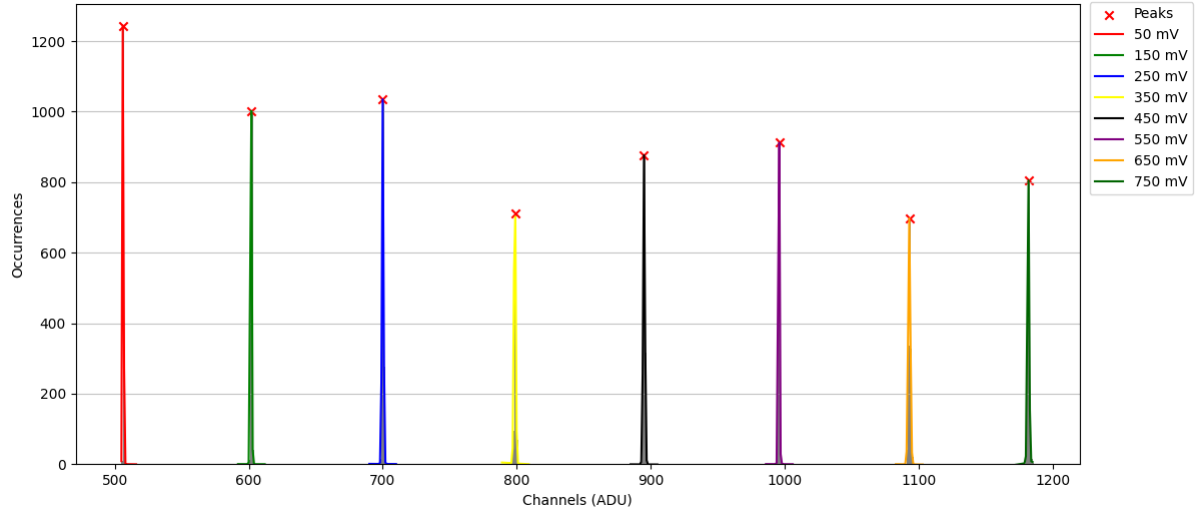
Figure 3.17: *Peaks produced by test impulses of different amplitude and processed by the γ-Bottom branch (only Pixel 0 enabled). The plot is not calibrated in energy.*

Table 3.5: *Conversion from voltage amplitudes of the input impulses to energy and fit parameters obtained from data processing of γ-Bottom branch.*

Test Impulse (mV)	n_e	Energy (MeV)	Centroids (ADU)	FWHM (ADU)	Amplitude (ADU)
50	5500	0.4	506.267 ± 0.002	0.924 ± 0.003	1541.6 ± 1.2
150	16500	1.1	601.677 ± 0.001	1.192 ± 0.006	1568 ± 3
250	27500	1.8	700.033 ± 0.003	1.400 ± 0.005	1543 ± 6
350	38500	2.6	798.608 ± 0.015	1.56 ± 0.05	1381 ± 32
450	49500	3.3	895.045 ± 0.003	1.569 ± 0.004	1468 ± 4
550	60500	4.0	995.668 ± 0.002	1.154 ± 0.008	1410 ± 3
650	71500	4.8	1092.989 ± 0.004	1.92 ± 0.01	1429 ± 7
750	82500	5.5	1181.786 ± 0.003	1.532 ± 0.007	1378 ± 6
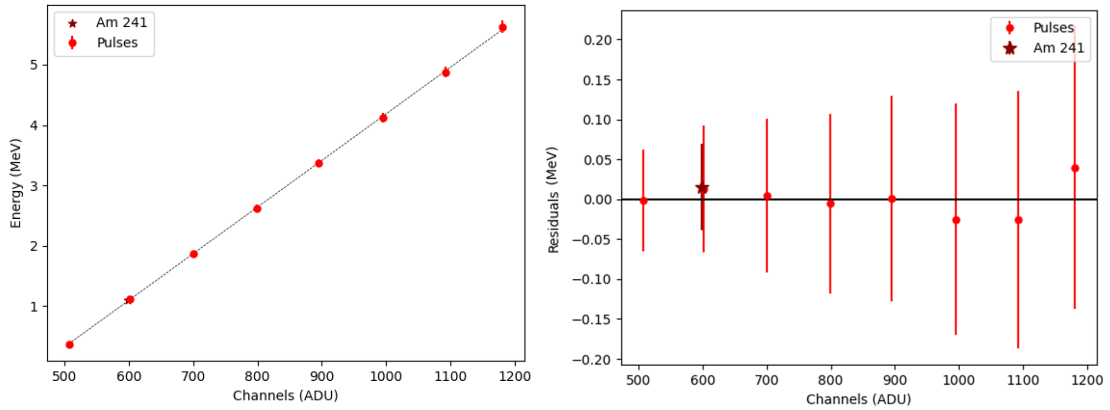
(a) *Calibration in energy for test impulses and ²⁴¹Am 60 keV emission line, expressed as MeV equivalent energy from CsI(Tl) charge production..*

**(b)** *Residuals of the linear regression for each point of the calibration plot.*

Figure 3.18: *Linear regression (left panel) and residuals (right panel) for the calibration in energy of the γ-Bottom branch. Plots valid for Pixel 0 only.*

3.4.8 Scintillator crystals in XGIS demonstration module
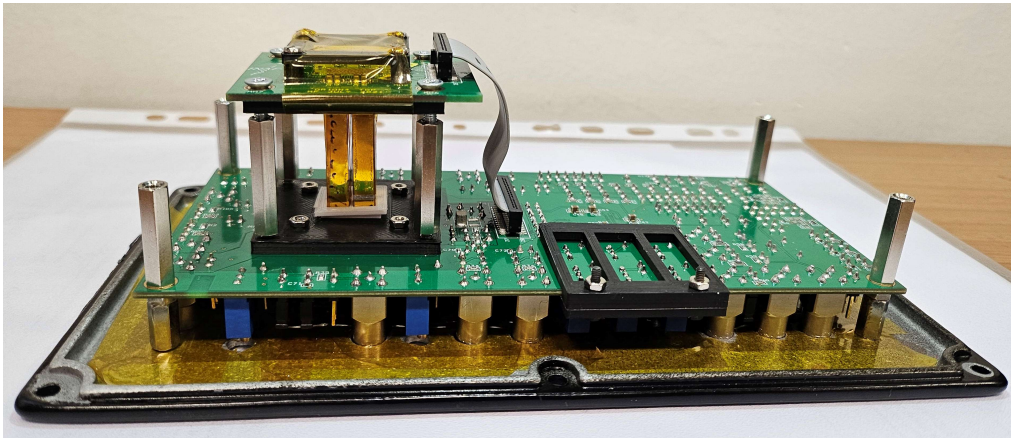
Figure 3.19: *XGIS demonstration module with SDDs coupled to CsI(Tl) scintillator bars.*

After the calibration of the SDDs with ORION IV readout, four CsI(Tl) scintillator bars have been mounted in the demonstration module, completing the Pixels configuration (Fig. 3.19). For the coupling of the crystals with the SDDs, a silicone pad was used: 8 pieces of silicone (4 for the Top SDD and 4 for the Bottom) were manually cut into squares of the dimensions of the scintillator section. Then
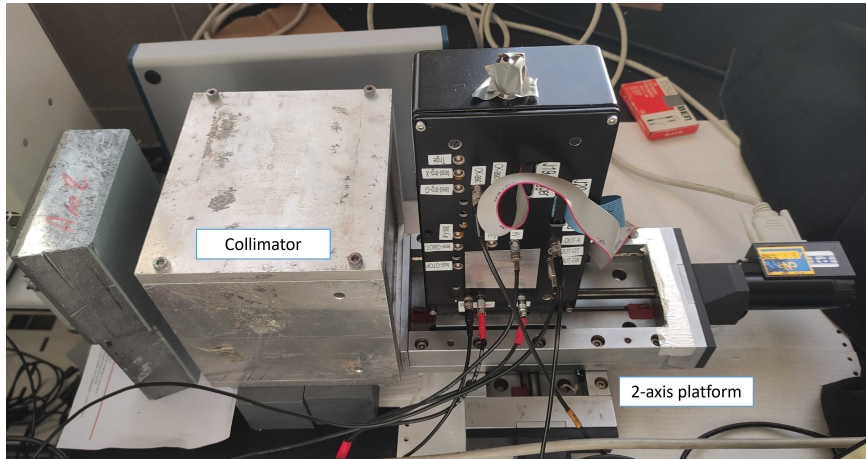
Figure 3.20: *Collimator and motorized platform with the module on top.*

performance tests were done introducing ^{241}Am (emitting low-energy X-ray photons) and a collimated radioactive γ-ray source (^{137}Cs, emitting γ-ray photons at 661.7 keV).

Test equipment

Two more components (Fig. 3.20) were added to the TE described in Section 3.4.1:

1. a lead slit collimator (10 cm thick) for the beaming of ^{137}Cs;

2. a motorized platform (*PI Linear Stage* and *PI C-863 Mercury*) over which the module has been glued: two axial movements are possible and commanded by *PIMikroMove* software.

These two new components were used to test the relation between the energy of ^{137}Cs incident photons (of energy 661.7 keV), the position of the interaction within the crystal and the measured Light Output. Hence, several acquisition were made with different beam placement with respect to the center of the scintillator bar of Pixel 0. Beaming the radiation emitted by ^{137}Cs was necessary to focus the incoming radiation in a point of the bar, keeping an adequate spatial resolution, reflected from the acquired spectra.

The discussion about the acquired spectra and their analysis will be fully addressed in the next sections, but an anticipation is now given because two issues were encountered:

- irrespective of different gains (Section 3.3), the X and γ processors share a common threshold value, due to the limitations of the current version of the ORION-BE; this results in limiting the energy range of the acquired spectra,
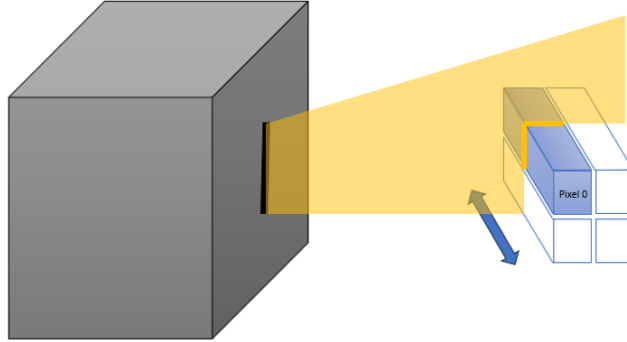
Figure 3.21: *Schematic representation of the collimated radiation onto the scintillator bar of Pixel 0. The arrow shows the motion of the bars with respect to the lead collimator. The motion is provided by the motorized platform.*

especially from the gamma processing branch of the ASIC. Therefore, current observations show a lower energy threshold of ∼400 keV instead of the expected 20 keV. However, the full range operability of the ORION-FE can be observed by enabling just the analog part of the ASIC (shaping mode) and then sampling the output signal with a commercial MultiChannel Analyzer (MCA by Amptek);

- MCA acquisitions revealed a poorly made optical contact with the silicone pad, thus the decision of substituting it and using another medium: drops of optical grease were directly poured on the input side for scintillator light of each SDD; before starting the acquisitions, a day was left for the grease to relax and uniformly cover the site. This change of optical coupling was reflected in a better measured value of CsI(Tl) Light Output.

3.4.9 Spectra of ^{137}Cs and ^{241}Am

The center of the scintillator bar was taken as a reference position by using the software of the 2-axis platform. The platform allowed micrometric precision with the movements of the board with respect to the collimated radiation. As shown in Fig. 3.20, the demonstration module inside its box is vertical, in order to have the bars oriented perpendicularly to the collimator slit (Fig. 3.21).

The radioactive source, emitting a spectral line at $E = 661.7$ keV, was placed in the collimator and several acquisitions were done with only Pixel 0 enabled. The event signals were sampled in shaping mode, so the digital part of the ORION-BE was disabled, as well as the discriminator. The MultiChannel Analyzer processed the output data (12 bits). The outputs were coming from the γ-Top branch and the γ-Bottom one at the time. Moreover, three beam placements were tested.
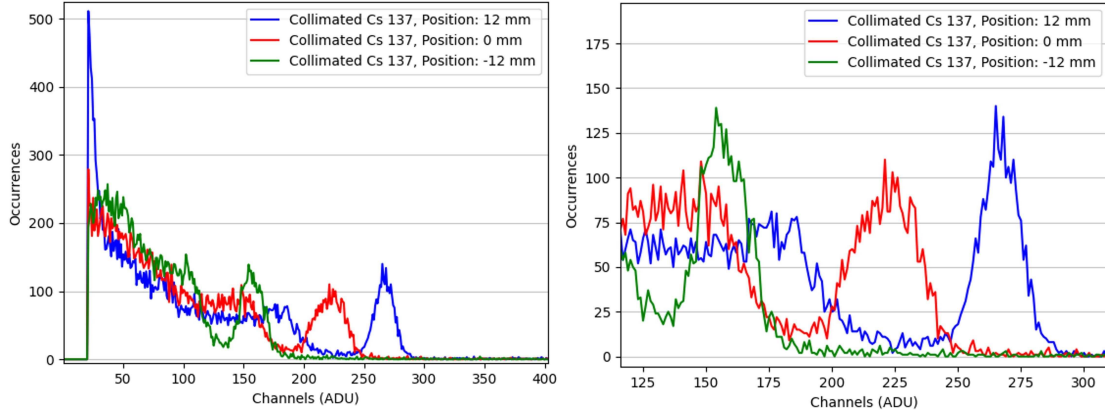
Figure 3.22: *Uncalibrated spectrum of ^{137}Cs acquired from γ-Top branch in positions [+12, 0, -12] mm (left). Compton features are visible on the left of the 661.7 keV peaks, which have been zoomed to better show their relative centroid position (right).*
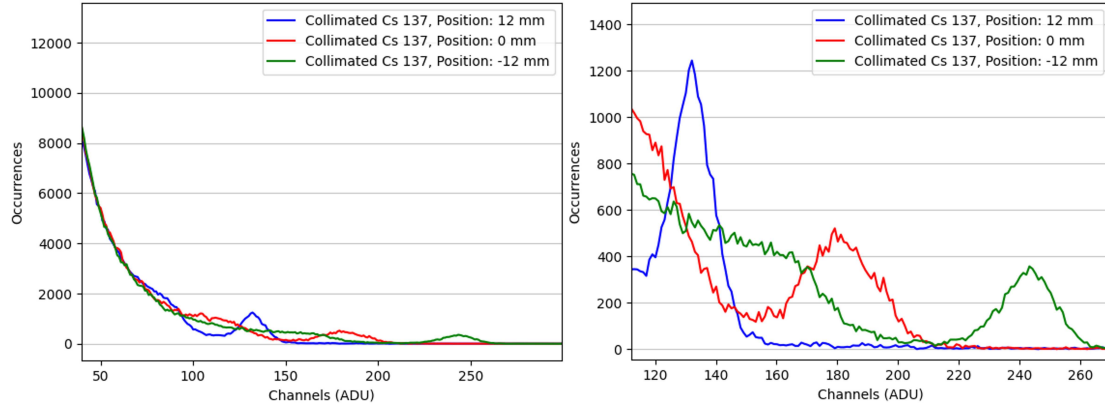
Figure 3.23: *Uncalibrated spectrum of ^{137}Cs acquired from γ-Bottom branch in positions [+12, 0, -12] mm (left); the peaks are not visible due to a high number of counts toward lower channels. Compton features are visible on the left of the 661.7 keV peaks, which have been zoomed to better show their relative centroid position (right).*

At the end, six spectra of ^{137}Cs were plotted and analyzed: three spectra (Fig. 3.22) in which the shaped signal came from the γ-Top branch, taken when the beam was at the center of the bar (reference position: 0 mm), near the Top SDD (position: +12 mm) and near the Bottom SDD (position: -12 mm); three spectra (Fig. 3.23) in which the shaped signal came from the γ-Bottom branch, taken at the same beam positions.

From the spectra, it is possible to notice that the centroids of the peaks are affected by the branch that is processing the signals and by the position of the incident beamed radiation. In fact, considering the 661.7 keV emission line in position +12 mm (i.e. near the Top SDD), there is a difference in peak centroid from

69

Fig. 3.22 to Fig. 3.23, with higher value of centroid when there is correspondence between beam placement and branch. This is valid also if the 661.7 keV emission line in position -12 mm (i.e. near the Bottom SDD) is considered, with a higher value of centroid when the signal is processed by the γ-Bottom branch.

These separate acquisitions from γ-Top and Bottom should be combined by summing the coincident signals and, due to the fact that the previously explained behaviour is present, it is possible to estimate energy and position of collimated radiation interaction inside the scintillator bar.

Each 661.7 keV peak was fitted (Fig. 3.24 is reported as an example valid for every spectrum) and its parameters extracted (Tab. 3.6).

Table 3.6: *Fit parameters for ^{137}Cs peaks, with incident radiation placed at different positions with respect to the center of the scintillator.*

	Position (mm)	Centroids (ADU)	FWHM (ADU)	Amplitude (ADU)
	+12	267.3 ± 0.3	19 ± 1	2344 ± 204
Top SDD	0	222.8 ± 0.6	34 ± 3	3542 ± 478
	-12	157.2 ± 0.3	21.2 ± 0.9	2559 ± 141
	+12	132.43 ± 0.09	14.1 ± 0.2	14544 ± 274
Bottom SDD	0	181.4 ± 0.3	27 ± 1	11723 ± 691
	-12	243.2 ± 0.1	20.1 ± 0.4	6807 ± 154
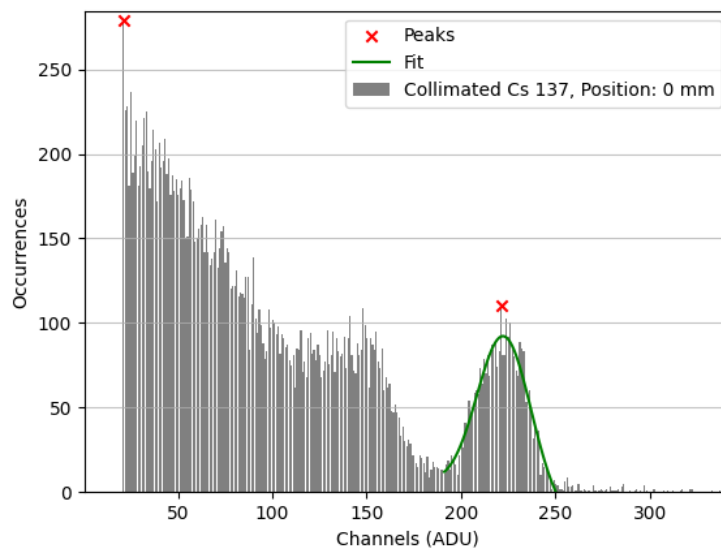
Figure 3.24: *Fit of ^{137}Cs 661.7 keV emission line, processed by γ-Top branch, with only Pixel 0 enabled. The collimated source was in position 0 mm.*
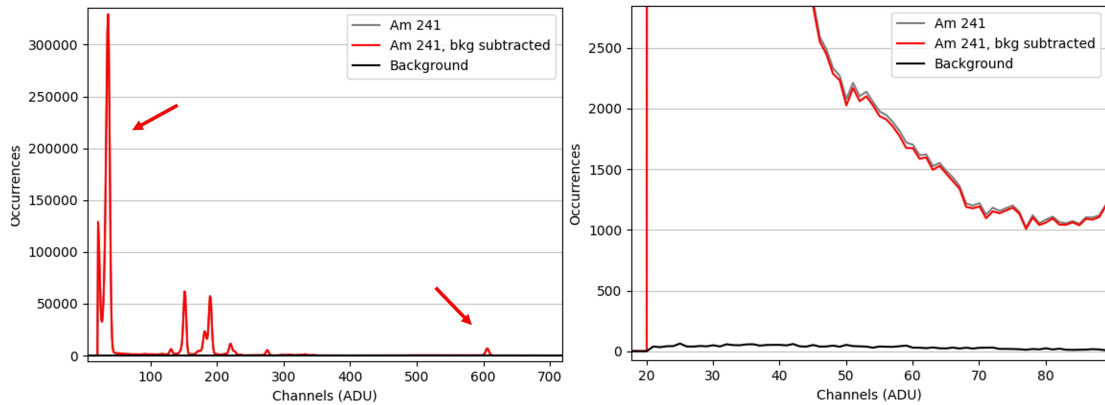
Figure 3.25: *Uncalibrated spectrum of ^{241}Am placed in front of the Top SDD, only Pixel 0 enabled. The first and the last peaks, indicated by red arrows, are both the 60 keV emission line (left). Zoom on the background (black line) affecting the low energy part of the spectrum (right). Background is so low that all the events (red line) are physical and not noise.*

Also spectra of ^{241}Am were acquired, directly placing the source first in front of Top SDD and then in front of Bottom SDD, without any collimation. These spectra were needed for a calibration in energy after the introduction of scintillator bars. Also a background acquisition (i.e. without the source) was taken for each branch and then subtracted to the spectra. In Fig. 3.25, the uncalibrated spectrum acquired with the source in front of the Top SDD is shown; this figure is taken as a reference figure for both cases.

Peaks placed above channel 100 are X photons energy deposit on the SDD, processed by the γ-Top branch. Moreover, two emission lines have been highlighted by red arrows: the two peaks correspond to ^{241}Am 59.5 keV spectral line. The first one represents the 60 keV photons that pass through the silicon and are stopped in the scintillator more efficiently, although they produce lower amplitude signals. The second line instead has a much smaller amount of counts because it represents the small fraction of 60 keV photons that silicon has stopped. This can demonstrate the power of the SISWICH method, because the low energy peaks obtained above channel 100 can be better represented by using the X branch, which is less noisy.

The Americium peaks in the X-ray energy range have been fitted and used for calibration purposes. The 60 keV peak from scintillator was also fitted to find the Light Output (Fig. 3.26 and Tab. 3.7).
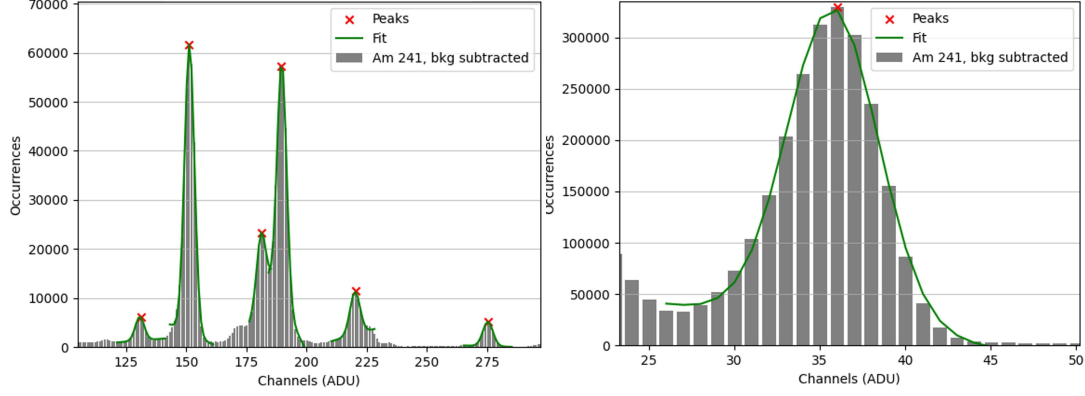
Gain and *Offset* from the calibration of the X-ray peaks have been obtained for both the spectra by placing the source in front of the Top and Bottom SDDs. They are expressed in terms on electrons instead of keV, for later Light Output

71

calculation:

$$Gain_T = (27.28 \pm 0.13) \text{ e}^-/\text{ADU} \; ; \; Offset_T = (-320 \pm 26) \text{ e}^- \qquad (3.9)$$

$$Gain_B = (29.99 \pm 0.19) \text{ e}^-/\text{ADU} \; ; \; Offset_B = (183 \pm 31) \text{ e}^- \qquad (3.10)$$

Figure 3.26: *Gaussian + Linear fit of the* ^{241}Am *peaks: fit of X-ray emission lines (left) and of 60 keV emission line seen by the scintillator bar of Pixel 0 (right).*

Table 3.7: *Fit parameters of* ^{241}Am *emission lines, with the source placed in front of the Top and Bottom SDDs. The 59.5 keV emission line is the one detected by the CsI(Tl), while the other lines have been detected by the SDD.*

	Emission line (keV)	Centroids (ADU)	FWHM (ADU)	Amplitude (ADU)
	11.9	130.63 ± 0.03	4.37 ± 0.08	22642 ± 443
	13.9	151.30 ± 0.03	4.82 ± 0.07	302705 ± 4899
	16.8	181.06 ± 0.06	4.23 ± 0.19	58095 ± 3769
Top SDD	17.7	189.70 ± 0.03	4.59 ± 0.08	240770 ± 5350
	20.7	220.09 ± 0.08	4.9 ± 0.2	45512 ± 2145
	26.3	275.32 ± 0.02	4.90 ± 0.04	26086 ± 232
	59.5	35.77 ± 0.05	6.26 ± 0.13	$(207 \pm 5) \cdot 10^4$
	11.9	102.07 ± 0.16	4.6 ± 0.4	2314 ± 234
	13.9	120.81 ± 0.07	5.6 ± 0.2	49196 ± 1950
	16.8	147.78 ± 0.05	5.1 ± 0.3	6195 ± 648
Bottom SDD	17.7	155.74 ± 0.08	5.0 ± 0.3	28712 ± 2382
	20.7	183.91 ± 0.12	7.2 ± 0.3	7135 ± 425
	26.3	233.48 ± 0.05	5.18 ± 0.12	2153 ± 56
	59.5	15.5 ± 0.4	9.8 ± 1.3	$(41 \pm 8) \cdot 10^5$

3.4.10 CsI(Tl) Light Output

As already mentioned, the Light Output is a characteristic of the scintillator crystal and is defined as the photoelectrons produced per unit energy deposited in the crystal. Hence, with the values of $Gain$ and $Offset$ obtained from the calibrations (eq. 3.9 and eq. 3.10), it is possible to obtain the number of photoelectrons produced in the interaction within the crystal, then divide by the energy of the emission line in order to obtain the Light Output.

In Tab. 3.8 the calculated values of LO are presented, referring to the 661.7 keV and 59.5 keV emission lines of all the spectra fitted. The typical value of LO assumed for CsI(Tl) is ~15 e$^-$/keV: the LO values calculated clearly differ from it. The nature of this difference can be related to a poorly done optical coupling, highlighting the importance of avoiding light loss in between the components.

Table 3.8: *Light output measured for 59.5 keV and 661.7 keV emission lines. Positions with value ±15 mm means that the radioactive source was placed in front of the SDDs (positive for the Top and negative for the Bottom).*

	Emission line (keV)	n_e	Position (mm)	LO (e$^-$/keV)
	59.5	655	+15	10.9
		649	-15	10.8
Top SDD	661.7	6970	+12	10.8
		5760	0	8.7
		3968	-12	6.0
Bottom SDD	661.7	4154	+12	6.3
		5623	0	8.5
		7474	-12	11.3

The silicone pad was removed and substituted with optical grease. Also four springs pressing down the Pixels were added to overcome the issue of a too flattened layer of grease. In fact, with the time passing by, the grease relax and forms an homogeneous layer between SDDs and scintillators, that may cause poor optical coupling if it happens to not touch anymore the components.

Then, acquisitions with ^{241}Am were taken again (Tab. 3.9), calibrations done and LO calculated again: $LO = 15.5$ e$^-$/keV for the source placed in front of Top SDD, instead $LO = 15.2$ e$^-$/keV for the source placed in front of Bottom SDD. These values are compatible with the standard LO assumed for CsI(Tl) scintillator crystal. Acquisitions with ^{137}Cs have not been taken, because tests

including a more precise procedure are developing.

$$Gain_T = (27.34 \pm 0.17) \text{ e}^-/\text{ADU} \; ; \; Offset_T = (-191 \pm 32) \text{ e}^- \qquad (3.11)$$

$$Gain_B = (30, 15 \pm 0.15) \text{ e}^-/\text{ADU} \; ; \; Offset_B = (-309 \pm 26) \text{ e}^- \qquad (3.12)$$

Table 3.9: *Fit parameters of ^{241}Am emission lines, with the source placed in front of the Top and Bottom SDDs. The 59.5 keV emission line is the one detected by the CsI(Tl), while the other lines have been detected by the SDD. The optical coupling has been made with grease.*

	Emission line (keV)	Centroids (ADU)	FWHM (ADU)	Amplitude (ADU)
Top SDD	11.9	125.50 ± 0.09	4.2 ± 0.2	4980 ± 278
	13.9	146.11 ± 0.03	5.19 ± 0.08	90613 ± 1560
	16.8	176.1 ± 0.3	5.3 ± 0.8	25537 ± 9604
	17.7	184.41 ± 0.03	4.9 ± 0.1	75856 ± 2155
	20.7	214.9 ± 0.2	6.5 ± 0.5	18985 ± 1650
	26.3	269.76 ± 0.03	5.19 ± 0.09	8691 ± 158
	59.5	41.01 ± 0.09	7.6 ± 0.3	$(82 \pm 4) \cdot 10^4$
Bottom SDD	11.9	117.86 ± 0.11	3.7 ± 0.3	620 ± 48
	13.9	136.49 ± 0.03	4.75 ± 0.07	15074 ± 251
	16.8	163.4 ± 0.2	4.6 ± 0.9	3177 ± 1215
	17.7	171.23 ± 0.04	4.3 ± 0.1	28713 ± 508
	20.7	198.87 ± 0.15	5.7 ± 0.4	3533 ± 278
	26.3	248.70 ± 0.03	4.70 ± 0.09	1695 ± 33
	59.5	40.60 ± 0.06	6.7 ± 0.2	$(162 \pm 5) \cdot 10^3$

3.4.11   Position dependent relation

A position dependent relation has been found, noticing the behaviour of ^{137}Cs peaks by collimating the source in different positions with respect to the center of the scintillator bar. The value of LO depends on that placement, so the goal of this calculation is to find the peak centroid (channel, ch), depending on position of interaction in the scintillator crystal (x), the energy of the peak (E) and the Light Output (LO). Taking as reference the γ-Top processor, the behaviour of the LO as been assumed linear : $LO_T(x) = A + Bx$.

In the calculations made to fill Tab. 3.8, the Light Output has been obtained dividing the number of photoelectrons by the energy of the emission line, so it is

possible to equal these two definition. Recalling eq. 3.9,

$$\frac{ch_T(x) \cdot Gain_T + Offset_T}{E} = A + Bx \qquad (3.13)$$

The boundary condition can be taken from Tab. 3.6: the centroid of the peak at position 0 mm is known and by setting $x = 0$ a variable is removed.

$$ch_T(0) \cdot Gain_T + Offset_T = E \cdot A \qquad \text{for } x = 0 \qquad (3.14)$$

The last equation gives an expression for $E \cdot A$, that can be substituted in eq. 3.13, giving:

$$ch_T(x) = ch_T(0) + \frac{EBx}{Gain_T} \qquad (3.15)$$

B has been determined by assuming a linear relation between x and LO: $B = 2.27$ e$^-$/(keV·mm), thus

$$ch_T(x) = 223 + 55 \cdot x \qquad (3.16)$$

The same calculation have been made for the Bottom processor, giving

$$ch_B(x) = 181 - 55 \cdot x \qquad (3.17)$$

These two equations give predictions about the position of the peak centroid by the knowledge of the collimated incident radiation position on the bars.

3.4.12 Temperature tests

An environmental test is presented for last. This kind of tests are important for instrumentation going into space: abrupt temperature variations, vibrations during the spacecraft launch and particle bombardment can severely affect the performances or damage the instrument. Thus, testing some critique environmental conditions is necessary. Furthermore, the operative range in which XGIS should not vary its performances is [-20, +20]°C and it is required to operate between [-15, 0]°C during the orbit.

The test presented in this section concerns the effects of different temperature values on the correct functioning of ORION IV, receiving and processing event signals from the 4-pixel XGIS prototype without scintillator bars. The X events have been produced using two radioactive sources placed in front of the Top SDDs: ^{55}Fe, emitting spectral lines at [5.9, 6.5] keV, and ^{241}Am, emitting at [11.9, 13.9, 16.8, 17.7, 20.7, 26.3] keV. The sources were needed in order to produce energy spectra across a certain temperature range.

The Test Equipment now comprehends also a Climatic Chamber (CC), inside which the prototype board and one source at time were placed. The temperature

range spanned from +20°C to -20°C, with data acquisitions every 10°C. A constant nitrogen flux ensured a dry environment during the measurements at low temperature, in order to avoid damaging of the electronics due to condensation. It is important to mention that the temperature variations were done slowly (< 10°C/h) and, once reached the value chosen for the acquisition, ∼30 minutes were left for stabilization of both the CC and the prototype, in order to obtain uniform temperature, to avoid stress on the PCB layers and damage of the board. Hence, this test procedure was time consuming, reflecting into data acquisitions done over several days.
The test succeeded because no physical damage was produced.

Instead, a still unresolved electronic issue was observed: the current consumption of the board was anomalous if the power supply of the board was turned on at any temperature different from T = 25°C. To avoid this malfunction, the power supply was turned on always at room temperature and never switched off during the descent toward different temperature values, in order to not influence the subsequent acquisitions. This behaviour is not addressed to specific circuital components yet and still needs to be solved.
Using this temporary expedient, spectral acquisition of ^{55}Fe and ^{241}Am were taken and analyzed. It is important to remember that the acquisitions were done only with Pixel 0 enabled, considering just the Top SDD (the energy of the spectral lines is in the X-ray energy band).

The acquisitions were done in stretching mode and lasted ∼30-40 minutes each; spectra have been created from the digital data words in output from the ORION-BE.
^{241}Am spectra were plotted using the `MESCAL` pipeline, while ^{55}Fe not, in order to overcome the limit of minimum number of spectral peaks required.

An analysis of the spectroscopic resolution and of the electronic noise depending on the temperature has been done. The fit parameter that gives a quantitative estimate of the spectral resolution is the FWHM, i.e. the width taken at half of the height of the spectral line. Knowing that the energy resolution of silicon detectors at X-ray energies is limited by the electronic noise and by the statistical spread on photon-electron conversion inside the photodetector itself (Perotti & Fiorini, 1999), at a first approximation the measured energy resolution can be expressed by:

$$FWHM^2 = R_{el}^2 + R_{stat}^2 \ , \tag{3.18}$$

where R_{el} is the electronic noise contribution and $R_{stat} = \sqrt{F \cdot n}$ is the statistical spread, expressed as the Poissonian noise (depending on the number of electrons n produced by the interaction of the silicon with an incoming X-ray photon of a certain energy) multiplied by a coefficient specific for the material called Fano

factor (F). For silicon, the typical value of the Fano factor is $F = 0.1$ (Perotti & Fiorini, 1999).

For the calculation, it is sufficient to take just one spectral line as a reference: the choice fell on ^{241}Am 13.9 keV line, because it is well isolated from other lines and is well populated, allowing better fitting. The FWHM is directly estimated by the spectral line fitting at different temperatures, but a conversion of the FWMH from ADU to e$^-$ is necessary, using the $Gain$ obtained from the X branch calibration (eq. 3.2) and the typical silicon value of charge per unit energy deposited ($W = 3.65$ eV/e$^-$). Then, the spectral resolution (σ) was calculated by using the relation between FWHM and standard deviation:

$$FWHM[e^-] = \frac{FWHM \cdot 10^3}{Gain} \cdot W^{-1} \quad ; \quad \sigma[e^-] = \frac{FWHM}{2.355} \tag{3.19}$$

The derivation of the electronic noise is just the application of the inverse formula of eq. 3.18: $R^2_{stat} = 381$ e$^-$, because $n = 13.9 \cdot 10^3 / W = 3808$ e$^-$. In Tab. 3.10 the spectral resolution and the electronic noise at different temperatures, calculated for the Top SDD of Pixel 0, are given. It is not surprising that both the standard deviation and the electronic noise decrease with decreasing temperature: the motivation resides into the fact that electrons use also thermal energy for transitioning from valence to conduction band, producing dark current. For this reason, the most effective way to reduce dark current (noise) is to cool the photodetector.

Table 3.10: *Values of spectral resolution σ and electronic noise R_{el} calculated for ^{241}Am 13.9 keV line, taking into account only the events from Top SDD in acquisitions at different temperatures for Pixel 0.*

Temperature (°C)	σ (e$^-$)	R_{el} (e$^-$)
$+20.0 \pm 0.1$	53 ± 1	49 ± 1
$+10.0 \pm 0.1$	44 ± 1	39 ± 1
0.0 ± 0.1	40 ± 1	35 ± 1
-10.0 ± 0.1	41 ± 1	36 ± 1
-20.0 ± 0.1	40 ± 1	35 ± 1

^{241}Am and ^{55}Fe spectra at T $= \pm$ 20°C are presented in Fig. 3.27 and Fig. 3.28. Knowing that σ decreases as the temperature becomes lower (from Tab. 3.10), the effect expected on spectra taken at progressively lower temperatures is to have a reduction of the FWHM, reflecting into slimmer spectral peaks. Moreover, in case of spectral doublets (i.e. lines at near energies that usually are classified as a line of intermediate energy), a larger separation of the peaks is evident, resulting in cleaner spectra.
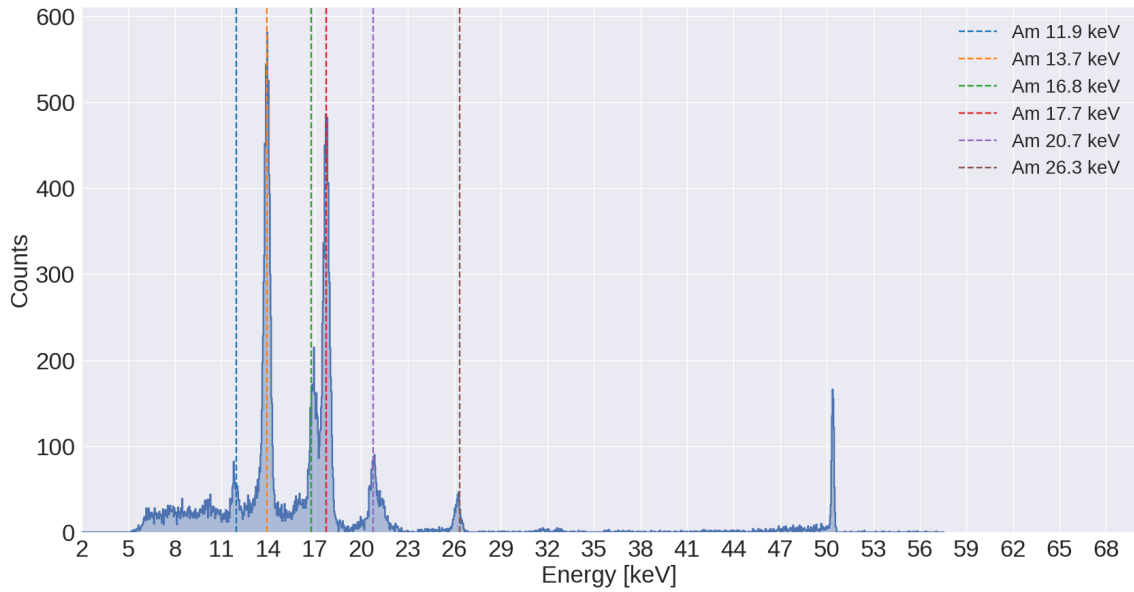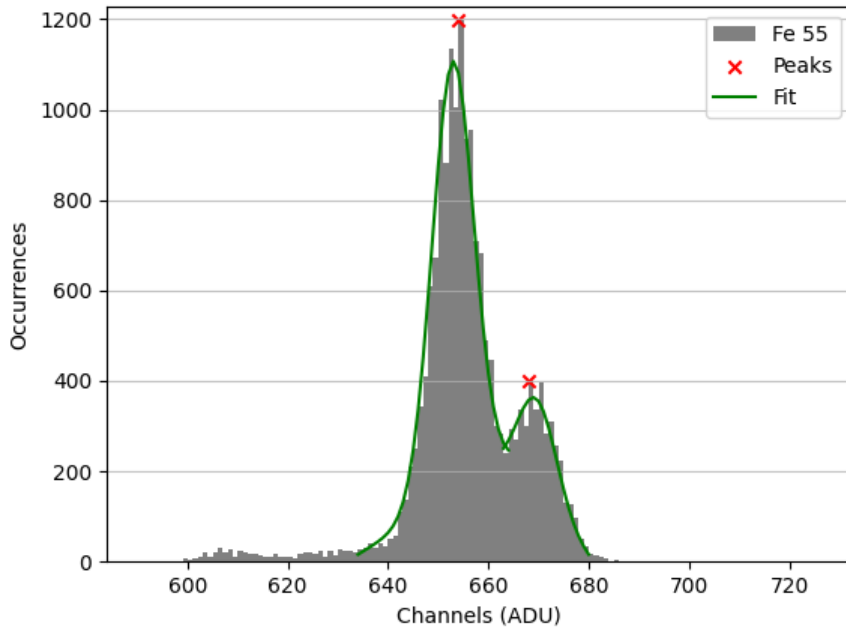
**(a)** *Multichannel spectrum of* ^{241}Am *produced with* `MESCAL`*, at* $T = +20°C$.
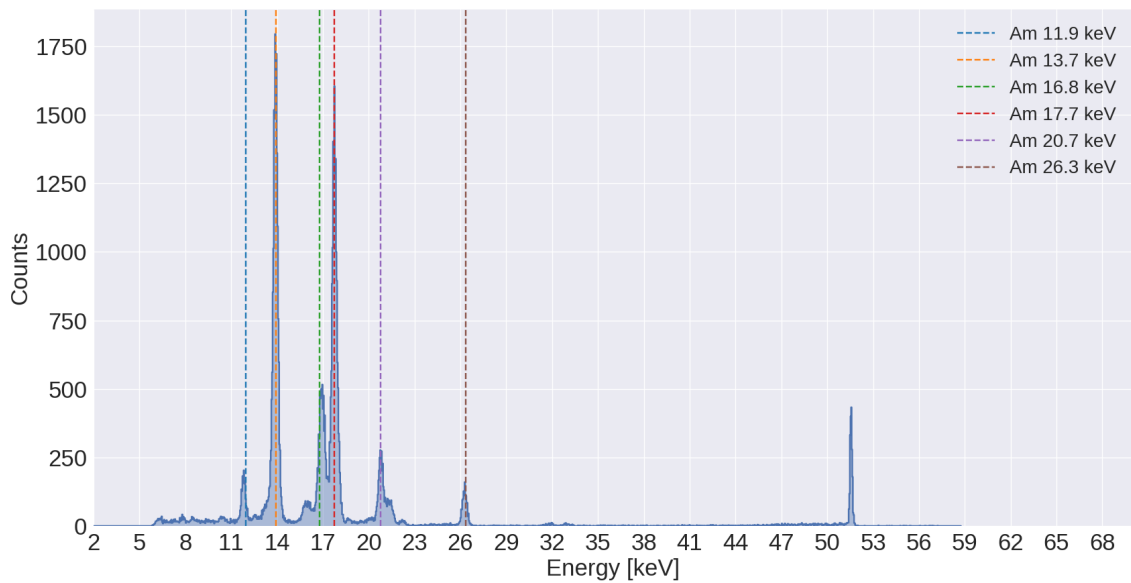
(b) *Multichannel spectrum of* ^{241}Am *produced with* `MESCAL`*, at* $T = -20°C$.

Figure 3.27: *Multichannel spectra of* ^{241}Am *(Top SDD) at different temperatures, acquired with only Pixel 0 enabled. The spectral lines have energies of [11.9, 13.9, 16.8, 17.7, 20.7, 26.3] keV. The last line has an energy of 60 keV, so it was not taken into account for this calculations, because it implies signal processing by γ branch. Notice how the spectrum at lower temperature appears much cleaner.*

(a) Multichannel spectrum of ^{55}Fe at $T = +20°C$.
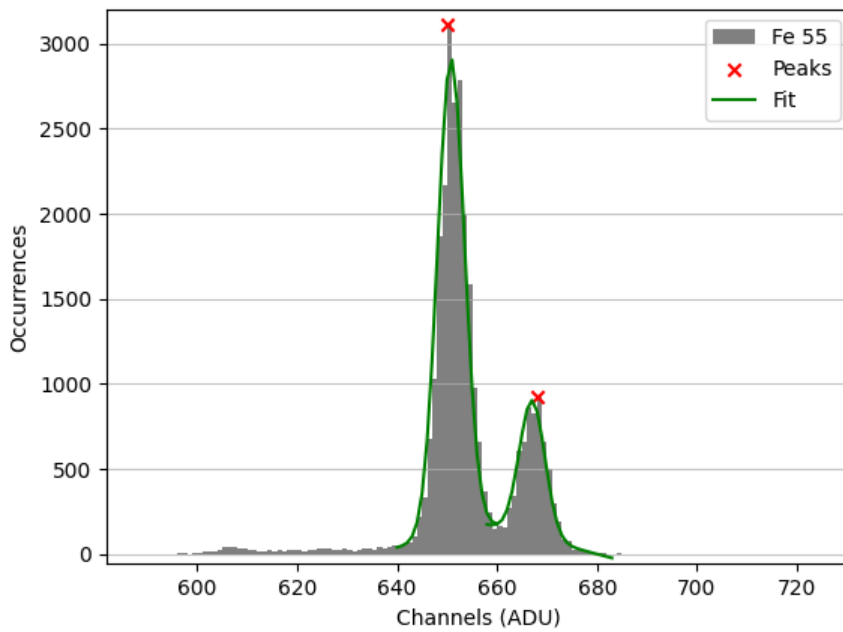
(b) Multichannel spectrum of ^{55}Fe at $T = -20°C$.

Figure 3.28: *Multichannel spectra of ^{55}Fe (Top SDD) at different temperatures, acquired with only Pixel 0 enabled. The spectral lines have energies of [5.9, 6.5] keV. The x-axis is in Analog Digital Units and not in keV, because the Python software does not perform the energy calibration. Notice how the spectrum at lower temperature presents a wider separation between the two peaks.*

Finally, the spectral resolution has been evaluated also for the 5.9 keV ^{55}Fe emission line at T $= +20°$C, obtaining $\sigma = (160 \pm 12)$ eV (corresponding to a $FWHM = 378$ eV), better than what expected in the scientific requirements of XGIS ($FWHM = 1200$ eV).

Chapter 4

Simulation of an alternative XGIS configuration

Having an instrument made by unitary detection elements leads to the possibility of customization. This freedom in deciding how to build your own detector translates into numerous configurations to explore. Of course, there are limited resources and not every imaginable detector configuration can be realized, so a less expensive way to test the performances and knowing what can best suit the scientific goals of a space mission is through simulations.

Due to the unique combination of energetic bands (from hard X-ray to soft γ-ray), XGIS becomes interesting for other space mission opportunities.

Thus, in this chapter XGIS is considered as "base detector" (same working principle and constituents described in Chapter 3), from which new configurations are examined and discussed. The aim of this study is not related to imaging due to the lack of the coded mask component, but is to show how the performances of an alternative-XGIS configuration, *aXGIS*, are affected by varying the instrumental setup of the detector. Hence, an estimate of the GRB rate is given, with a dedicated part of the code to localization of the bursts.

4.1 Instrumental setup

aXGIS instrument is made by six X/Gamma-ray cameras, placed along the perimeter of the surface of the telescope and equally spaced from each other.

A single detection element consists of CsI(Tl) scintillator bars (3 cm long), coupled at the top and at the bottom to square SDD detectors (5×5 mm^2).

The unitary detection element of aXGIS is the *module*, and an array of modules makes a *super-module* (Fig. 4.1): the configuration that has been studied implies a module made of 10×10 detection elements (of size 5×5 cm^2) and a super-
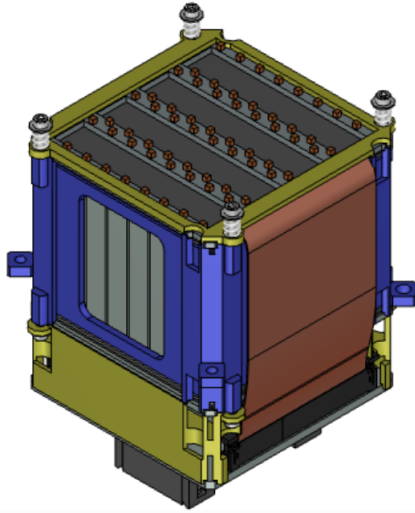
(a) *Design of an aXGIS module: different colors represents different mechanical and structural part of the detector (ESA-THESEUS, 2021).*
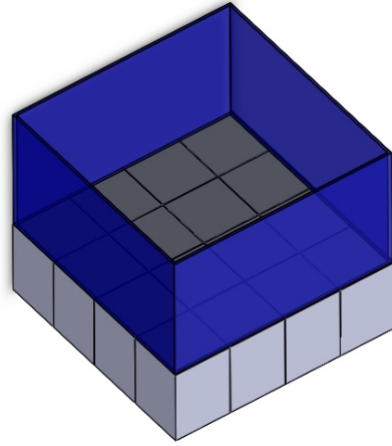
(b) *Design of an aXGIS camera: a collimator (blue) surrounds the super-module (grey). Notice that the super-module is formed by 4×4 modules (grey cubes). Courtesy of Enrico Virgilli.*

Figure 4.1: *Design of a module (left) and a camera (right) of aXGIS.*
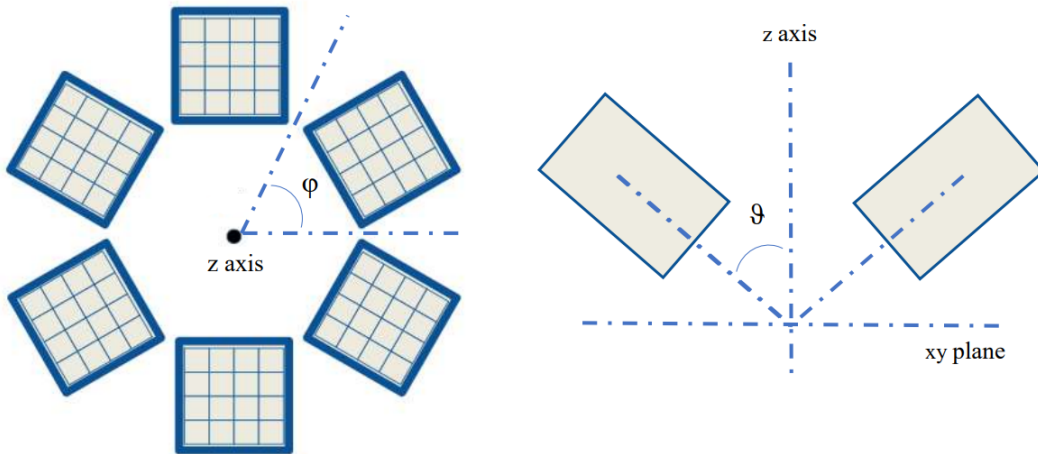

Figure 4.2: *Angular separation among cameras: polar view (left) and lateral view (right) in order to visualize φ and ϑ. Courtesy of Enrico Virgilli.*

module of 4×4 modules (of size 20×20 cm^2). Adding a tungsten collimator to a super-module produces a camera : the height of the collimator, $h_{collimator}$, is a variable, so different values can be assigned.

The angular distance in the xy plane between adjacent cameras is $\varphi = 60°$ and each camera can be misaligned from the z axis of an arbitrary ϑ (Fig. 4.2), providing a single camera Field of View that depends on the value assigned to the collimator height and a total instrument FoV that depends both on collimator height and ϑ.

In Table 4.1 some configurations are reported, keeping fixed module and super-module sizes, with a particular emphasis on the components mass. Obviously, an increase in height of the collimator implies an increase in weight of the cameras, that reflects into a general increase of mass of the entire instrument.

Table 4.1: *Study of aXGIS instrument mass budget: the configuration taken in exam includes 6 cameras and different values of $h_{collimator}$ are provided. This results into an increase of the mass of each single camera, which leads to an increase of mass for the entire instrument.*

$h_{collimator}$ (cm)	$m_{collimator}$ (kg)	m_{SM} (kg)	$m_{SM+collimator}$ (kg)	m_{aXGIS} (kg)
10	1.00	7.15	8.15	48.92
15	1.50	7.15	8.65	51.92
20	2.00	7.15	9.15	54.93
25	2.50	7.15	9.66	57.93

Table 4.2: *Study of the variation of aXGIS FoV, depending on $h_{collimator}$ and ϑ: first, ϑ is kept fixed at 45°, letting $h_{collimator}$ free to vary; then $h_{collimator}$ is kept fixed at 15 cm and ϑ varies. Two opposite behaviours of the FoV are obtained.*

$h_{collimator}$ (cm)	ϑ (deg)	FoV_{camera} (sr)	FoV_{aXGIS} (sr)
10	45	4.9	9.5
15	45	3.4	8.3
20	45	2.5	7.3
25	45	1.8	6.3
15	35	3.4	7.5
15	45	3.4	8.3
15	55	3.4	9.3

In Table 4.2 some configurations for different values of collimator height and ϑ are reported, keeping fixed module and super-module sizes, putting focus on the FoV of the instrument. It is evident that when ϑ is kept fixed, the increase in collimator height produces a decrease of aXGIS FoV, due to the FoV decrease for each camera; instead, keeping fixed the collimator height and letting vary the angle of the cameras results into an increase of the FoV, due to the fact that there is less common area among the cameras. The configurations reported in Tab. 4.2 are all plotted Appendix A, showing the relation between $h_{collimator}$, ϑ and the instrument FoV.

In the simulation, every instrument characteristic can be arbitrarily modified and set up through a dynamic Graphic User Interface (Fig. 4.3).
From the GUI, it is possible to set also the number of synthetic GRBs generated, their type (long or short) and a threshold for the significance of the detected events, where the choice for the threshold value is 7 by default.
By using the button "*set parameters*", every entry of the GUI is read and stored in order to be used in the simulation, that starts when "*start simulation*" is pressed.

The chosen energy band is written manually when running the software, knowing that aXGIS can cover a wide energy range (2 keV - 10 MeV). To perform the simulation in aXGIS total energy band, two ARF files, one in X and the other in S mode, have been combined. The Ancillary Response Files, which contain all the information on the capability of the instrument in terms of collecting area and sensitivity, provide a unique effective area vs. energy relation, used to modify the response of the detector (Fig. 4.4). The X and S mode ARF file are related to the efficiency of the SDD and of the scintillator employed.

Hence, the camera response to the detected event is not constant and also depends on the dimensions of the super-module and on the orientation of the camera itself (keeping fixed the direction of the incident GRB photons).
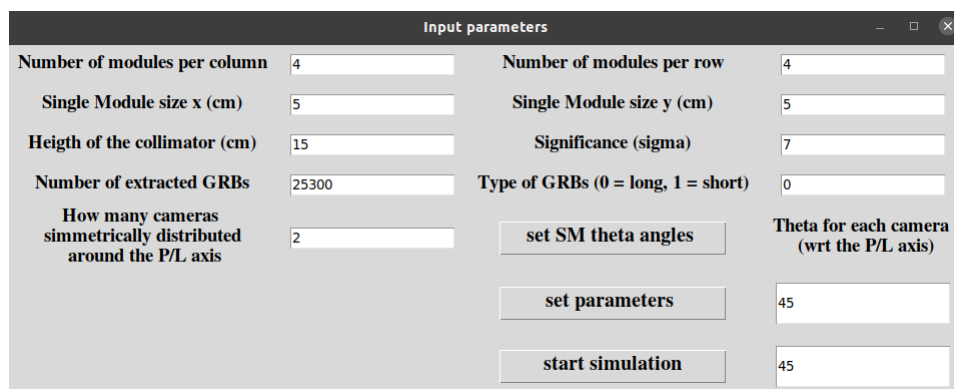
Figure 4.3: *Design of the Graphic User Interface: every parameter can be arbitrarily modified just by editing the text boxes.*

84
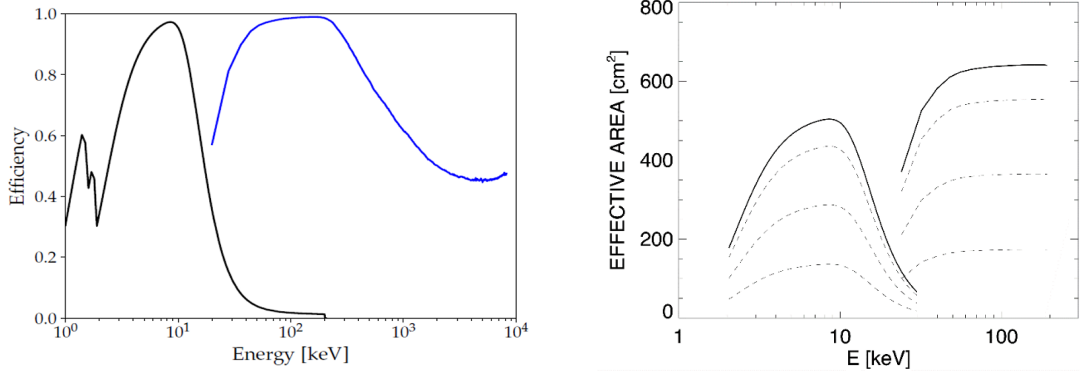
(a) *Normalized effective area (efficiency) for X mode (direct X-ray absorption in SDD, black curve) and S mode (scintillation light readout).*

(b) *Detail of the effective area in the 2-200 keV energy range. Solid line corresponds to FoV effective area with off-axis angles < 5°, dashed curves corresponds to increasing off-axis angles of 10°, 20°, and 30°.*

Figure 4.4: *Efficiency of XGIS detector plane in all the instrument working energy range (left); detail in the energy range 2-200 keV with varying off-axis angles (right). From Amati et al. (2021).*

It is important to consider this geometric-dependent behavior to produce values of S/N not overestimated: to do so, the area of the detector must be modified by a multiplicative factor $R(\vartheta, \varphi)$, strongly dependent also on $h_{collimator}$ and the sizes a and b of the super-module (Fig. 4.5, Orlandini et al., 2009).

$$R(\vartheta, \varphi) = \left[1 - \frac{h_{collimator}}{a} \tan \vartheta \ \sin \varphi\right] \cdot \left[1 - \frac{h_{collimator}}{b} \tan \vartheta \ \cos \varphi\right] \quad (4.1)$$
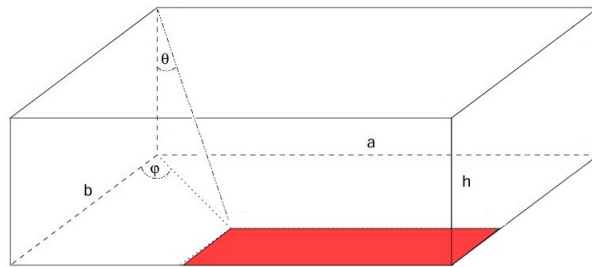
Figure 4.5: *The collimator blocks part of the incident radiation, shadowing the detection plane. The surface that collects the incoming photons from a certain direction is highligted in red (Orlandini et al., 2009).*

85

4.2 Synthetic GRB population

The simulated GRBs are extracted from a synthetic GRBs population, based on a population model that reproduces the observed properties of GRBs detected by *Swift*, *Fermi* and *CGRO* in the hard X-ray and γ-ray bands. At each simulated event corresponds a value of the peak energy and a redshift from the assumed distributions. Through the peak energy-isotropic luminosity and the peak energy-isotropic energy correlations (Fig. 1.10), L_{iso} and E_{iso} are respectively assigned to each simulated burst. The fluence and peak flux of the bursts are obtained by assuming a Band spectral shape with low and high energy spectral slopes randomly extracted based on their observed distributions (Ghirlanda et al., 2021).

The population contains $2\,018\,428$ events and corresponds to 78.9 years of detection of GRBs distributed over the whole sky. Each event is identified by a flag as long ($N_{long\ GRBs} = 2\,000\,000$) or short ($N_{short\ GRBs} = 18\,428$). Every burst has a list of parameters, shown in Table 4.3.

Table 4.3: *Parameters associated to every GRB of the synthetic population.*

Parameter	Symbol	Description
Fluence	$s\ [ph \cdot cm^{-2}]$	Photon fluence (10 keV - 1 MeV)
Peak flux	$F_P\ [ph \cdot cm^{-2} \cdot s^{-1}]$	Peak flux (10 keV - 1 MeV, 1 s integration)
α	/	Photon index of Band spectrum at low energies
β	/	Photon index of Band spectrum at high energies
Peak energy	$E_P\ [keV]$	Observed peak energy in Band spectrum
Duration	$T_{eff}\ [s]$	Effective duration (time necessary to collect the total fluence of the burst)
Redshift	z	Redshift
Flag	f	=1 for short GRB; =0 for long GRB
J flux	$F_{J500}\ [mJy]$	Infrared flux in J band after 500 s

α, β and E_P are parameters of the Band spectrum, described by eq. 1.1 (Section 1.3).

Hence, in each run of the simulation, a random burst of the synthetic population is chosen. Moreover, the time of occurrence and sky coordinates (θ_{GRB}, ϕ_{GRB}) must be generated randomly for every selected event. When a burst is detected, all the associated parameters, as well as the randomly generated ones, are extracted.

4.3 GRB detection and localization

After the extraction of GRBs parameters from the synthetic table, angles θ_{GRB} and ϕ_{GRB} are known data.

In reality, the location in the sky of the detected GRBs is unknown, so θ_{GRB} and ϕ_{GRB} must be estimated.

The logic of the code, used to mimic the detection of the events in the sky, is based on the counts registered from the instrument: ideally, if a camera shows 0 counts, then the GRB was not in the FoV of that single camera; if more than one camera registered different values of counts, then the GRB was in the common area seen from the cameras, i.e. the intersection of the FoVs. Practically, what aXGIS registers is the signal to noise ratio for each camera, calculated as the ratio between the integrated signal and the integrated background. Hence, six values of S/N (one for each camera) are stored into an array and only the events with a S/N > 7 in at least one camera are flagged as GRBs (otherwise we are dealing with background).

Knowing which and how many cameras detected the burst can give a rough idea of the area from which the GRB is observed, but a more precise information about the GRB direction is obtained if the GRB was detected by three cameras at least (triangulation): therefore, a minimum of three values of S/N > 7 is required to perform the localization.

The localization algorithm is based on a simple χ^2 test, a quantitative way to perform a comparison between data and model, the latter identified by an *efficiency matrix*.

The efficiency matrix is built knowing that the response of the super-module depends on the events direction in the sky, keeping fixed the orientation of each camera. However, GRBs can come from any direction, hence it is useful to associate the response of the instrument to every possible direction in the sky, i.e. every couple $(\theta_{sky}, \phi_{sky})$.

Thus, the sky has been mapped using an angular step of 1° in θ_{sky} and ϕ_{sky}, resulting into a grid of $180 \times 360 = 64\,800$ points. Then, the mean effective area (expressed as a fraction of the geometrical area, A_{geom}) has been calculated for each direction and for each camera i (eq. 4.2), obtaining an array $\overline{A_{eff}}(\theta, \phi)$ of six values of area (one for each camera) associated with every point of the grid.

$$\overline{A_{eff,i}}(\theta, \phi) = \frac{R_i(\theta, \phi) \int_{E_{min}}^{E_{max}} A_{arf}(E)\, dE}{A_{geom} \cdot \Delta E} \tag{4.2}$$

In eq. 4.2, $R_i(\theta, \phi)$ is the geometric-dependent factor depending on the orientation of the ith-camera, $\Delta E = E_{max} - E_{min}$ is the chosen energy band and $A_{arf}(E)$ is the area depending on energy, obtained from the ARF file. Moreover, θ and ϕ

have been obtained considering a change of reference frame: they are defined as the grid point sky coordinates seen by every camera as if its center were pointing in the polar direction. This change of reference will be applied also to the proper bursts when computing their S/N (Fig. 4.6). First, a rotation around z axis is performed, then it is followed by a rotation around x axis, as eq. 4.3 and 4.4 show.

$$(x', y', z') = \begin{pmatrix} \cos\varphi & -\sin\varphi & 0 \\ \sin\varphi & \cos\varphi & 0 \\ 0 & 0 & 1 \end{pmatrix} \cdot \begin{pmatrix} \sin\theta_{sky} \cdot \cos\varphi_{sky} \\ \sin\theta_{sky} \cdot \sin\varphi_{sky} \\ \cos\theta_{sky} \end{pmatrix} \tag{4.3}$$

$$(x, y, z) = \begin{pmatrix} 1 & 0 & 0 \\ 0 & \cos\vartheta & -\sin\vartheta \\ 0 & \sin\vartheta & \cos\vartheta \end{pmatrix} \cdot \begin{pmatrix} x' \\ y' \\ z' \end{pmatrix} \tag{4.4}$$

$$\begin{cases} \theta = \arctan(\sqrt{x^2 + y^2}/z) \\ \phi = \arctan(y/x) \end{cases} \tag{4.5}$$
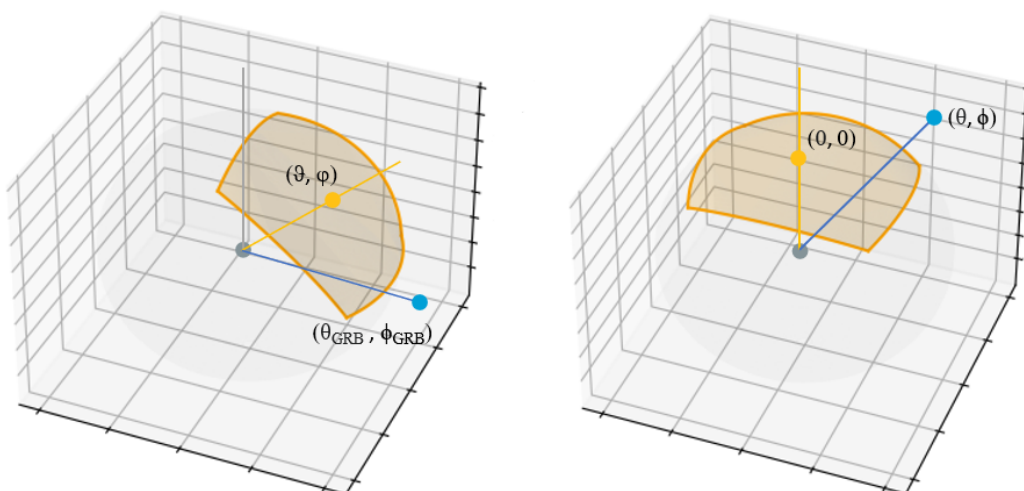
Figure 4.6: *Graphical representation of the change of reference frame explained by eq. 4.3, 4.4 and 4.5, applied to the sky coordinates of a GRB. It is valid also if applied to the coordinates of the sky grid points.*

The values of effective area have been normalized to the maximum effective area for each direction, in order to work with adimensional quantities, i.e. defining an efficiency array $\epsilon(\theta, \phi)$ given the direction in the sky:

$$\epsilon(\theta, \phi) = \frac{\overline{A_{eff}}(\theta, \phi)}{max(\overline{A_{eff}}(\theta, \phi))} \tag{4.6}$$

88

In the end, the efficiency matrix (ε) is given by all $64\,800{\times}6$ values of efficiency:

$$\varepsilon = \begin{bmatrix} \epsilon_1 \\ \vdots \\ \epsilon_{64800} \end{bmatrix} = \begin{bmatrix} \epsilon_{1,1} & \cdots & \epsilon_{1,6} \\ \vdots & & \vdots \\ \epsilon_{64800,1} & \cdots & \epsilon_{64800,6} \end{bmatrix} \tag{4.7}$$

The sum of the six values $\overline{A_{eff,i}}$ (eq. 4.2) has been performed for each grid point, providing the total effective area $\overline{A_{eff,TOTAL}}$ due to the combination of efficiencies of each camera; $\overline{A_{eff,TOTAL}}$ (expressed as a fraction of the geometrical area) has been plot in the 100 - 150 keV energy band, with $\vartheta = 45°$, for different values of collimator height (Fig. 4.7). Bright colors define areas of the sky with high efficiencies, i.e. areas perpendicular to the centre of a given camera, whereas dark colors define low efficiency areas.

The choice of the collimator height impacts significantly on the efficiency, making evident that higher collimators reduce camera FoV by producing a "hole" in direction ($\theta_{sky} \sim 0$, ϕ_{sky}). Dark colors in that region are reflecting an uncovered area or simply the effect of being on the edge of the cameras FoV (i.e. far from the centre).

The data vector, instead, identified by one S/N array for each extracted GRB, is built by using the parameters associated to the latter.

The signal is calculated for each camera i by:

$$S_i = S_{GRB,i}(\theta, \phi) \cdot \overline{A_{eff,i}}(\theta, \phi) \tag{4.8}$$

where $\overline{A_{eff,i}}(\theta, \phi)$ is defined in eq. 4.2, θ and ϕ are obtained through eq. 4.3, 4.4, 4.5 substituting the grid point sky coordinates (θ_{sky}, ϕ_{sky}) with the generated GRB sky coordinates (θ_{GRB}, ϕ_{GRB}).

$S_{GRB,i}(\theta, \phi)$ is the fluence of the GRB in the energy band considered for the ith-camera and is defined by:

$$S_{GRB,i}(\theta, \phi) = T_{eff} \cdot R_i(\theta, \phi) \cdot \int_0^{\Delta E} N_E(E) \cdot A_{arf}(E)\, dE \tag{4.9}$$

The calculation for the background depends on the type of GRB extracted. For long GRBs, the integration time is T_{eff} (defined in Tab. 4.3): this is reduced to 64 ms for short GRBs (Horstman et al., 1975 and Mereghetti, 2023). Finally, the S/N array is given by

$$S/N = \left[\frac{S_i}{\sqrt{N_i}} \right]_{i=0\ldots6} \tag{4.10}$$

Now that model and data vector are obtained, a χ^2 test can be performed. First of all, the S/N array (the data vector) is normalized to the maximum value
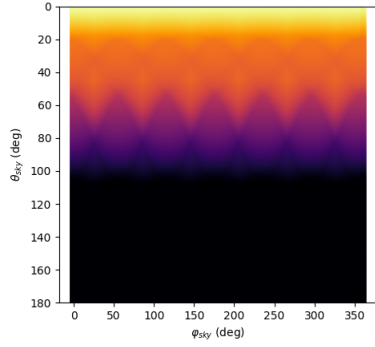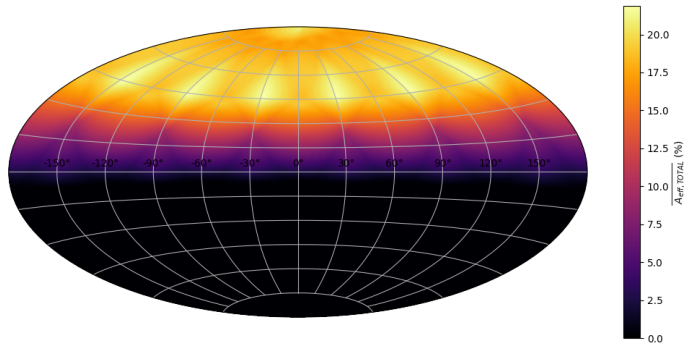
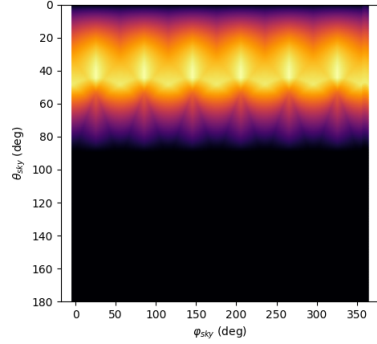**(a)** *Efficiency matrix sky map: planar view of the efficiency values for configuration $h_{collimator} = 10$ cm.*
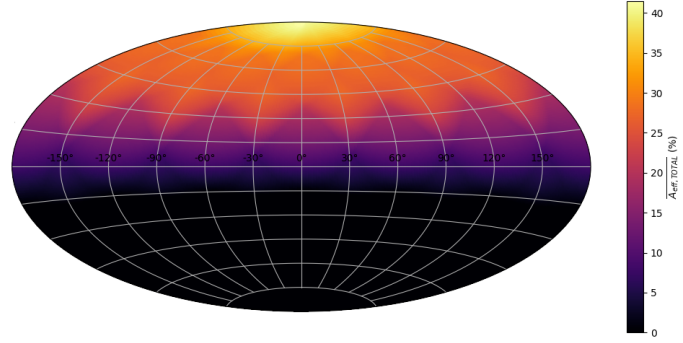
(b) *Efficiency matrix sky map: sky-projected view of the efficiency values for configuration $h_{collimator} = 10$ cm.*
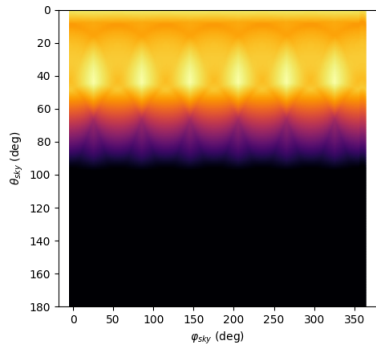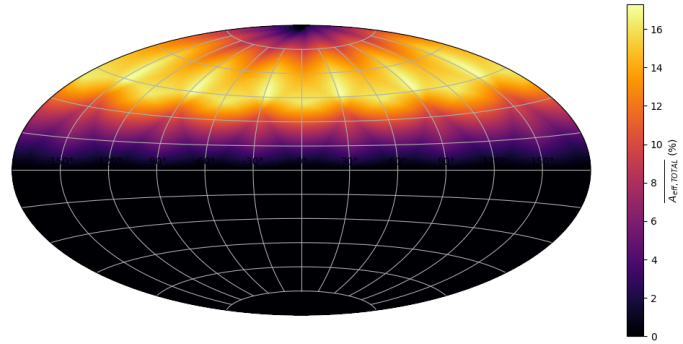
(c) *Efficiency matrix sky map: planar view of the efficiency values for configuration $h_{collimator} = 15$ cm.*
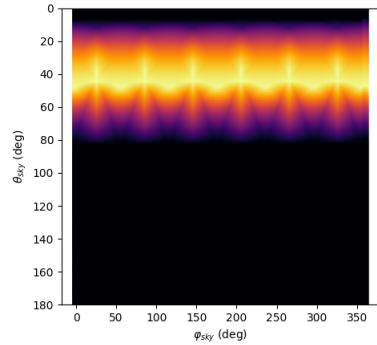
(d) *Efficiency matrix sky map: sky-projected view of the efficiency values for configuration $h_{collimator} = 15$ cm.*

(e) *Efficiency matrix sky map: planar view of the efficiency values for configuration $h_{collimator} = 20$ cm.*

(f) *Efficiency matrix sky map: sky-projected view of the efficiency values for configuration $h_{collimator} = 20$ cm.*
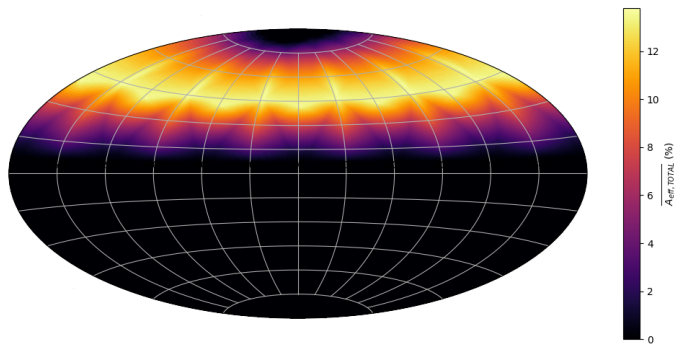

(g) *Efficiency matrix sky map: planar view of the efficiency values for configuration $h_{collimator} = 25$ cm.*

(h) *Efficiency matrix sky map: sky-projected view of the efficiency values for configuration $h_{collimator} = 25$ cm.*

Figure 4.7: *Efficiency matrix sky map: planar (left) and sky-projected (right) view of the efficiency values for each point of the sky grid. The plotted configurations imply an energy band of 100-150 keV, $\vartheta = 45°$ and a variable $h_{collimator}$.*

of S/N, i.e. we are defining a reference camera.

$$S/N_{ref} = \frac{S/N}{max(S/N)} \tag{4.11}$$

This allows us to find the proportions of counts between the reference camera and the other cameras and to have adimensional quantities that can be compared to the line-vectors ϵ_j of the efficiency matrix.

Then the code searches for the zeros placed at the same element position both in data and model vector: this translates into focusing only in areas that are intersection of multiple camera FoVs which detected a burst. Hence, in that intersection area, the χ^2 test is done:[1]

$$\chi_j^2 = \sum_{i=1}^{6} \frac{(S/N_{ref,i} - \epsilon_{ji})^2}{\epsilon_{ji}} = \chi^2(\theta, \phi) \tag{4.12}$$

Then a minimization is performed: the minimum $\chi^2(\theta, \phi)$ is a direct estimation for the GRB direction, because in that grid point the data best match the model, from which we can extrapolate the sky coordinates θ and ϕ.

Maps color-coded by values of χ^2 are reported in Fig. 4.8: the green cross represents the "true" direction $(\theta_{GRB}, \phi_{GRB})$ from which the burst arrives, the red cross instead is where the minimum χ^2 is placed, from which an estimation of the GRB direction can be obtained. The shape of the maps reflects the common area between the cameras that detected the burst, so an initial guess about how many cameras have seen the event can be made from the analysis of the map shape. Notice how the same pattern are visible from the efficiency maps.

4.4 Estimation of GRB rate

This simulation aims at providing an estimation of the GRBs rate, so every GRB that has been detected and located is registered into a log file.

The information in the log file include a recap of the input parameters from the GUI, the derived FoVs, sizes and masses of single camera and instrument and, finally, a list with the detected and localized GRBs.

In the list, each event is flagged as long or short, the array of S/N is given as well as the parameters for the Band function, the redshift and the generated angles θ_{GRB} and ϕ_{GRB}.

Thanks to the use of six counters (each one is associated with a camera and registers when the camera has a S/N > 7), it is possible to make an estimation of the

---

[1]The definition of χ^2 considered is based on the quadratic deviation weighted by the expected value from the theoretical model.
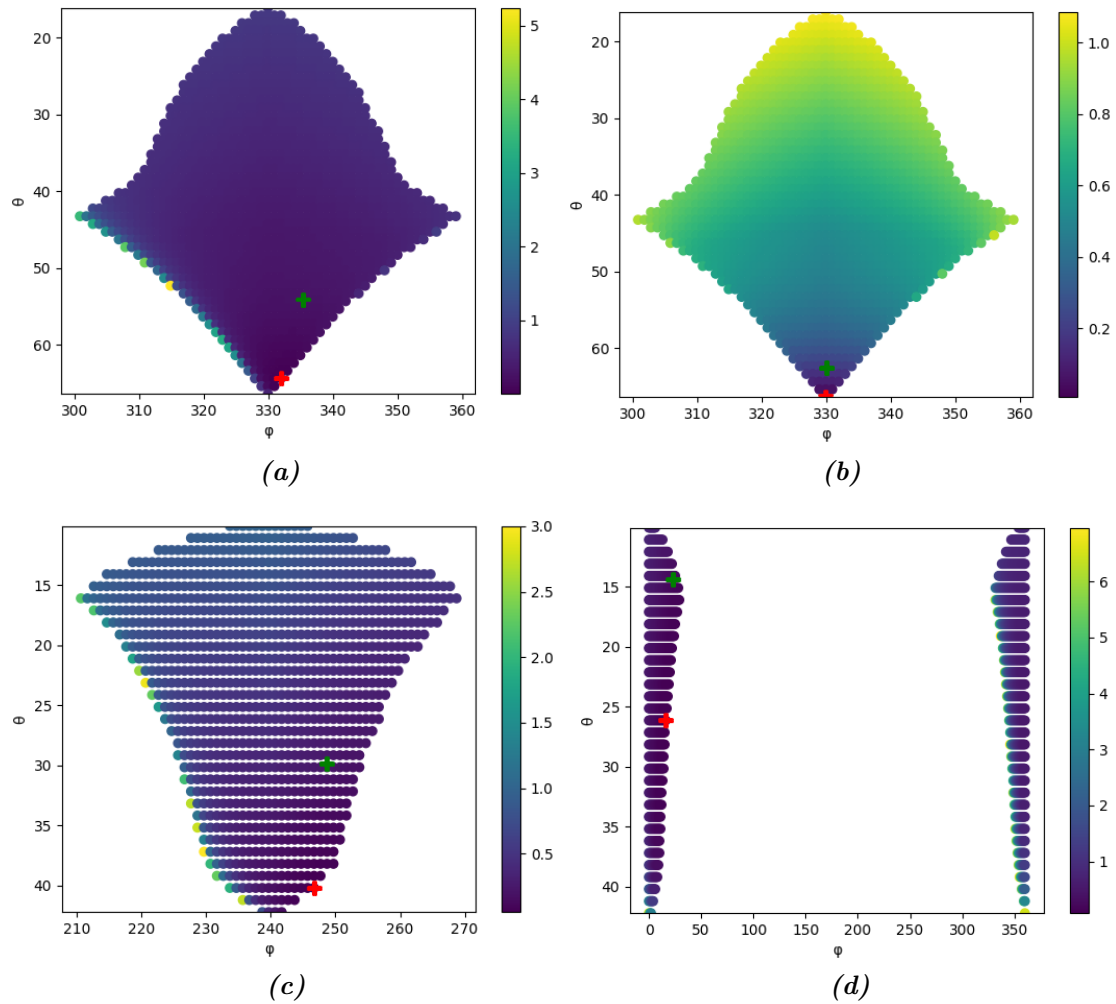
Figure 4.8: *Different localization maps, color-coded by value of χ^2. The shapes of the maps are due to cut on values of $\chi^2 > 7$ and to the area enclose by the overlap of FoV of minimum 3 cameras. Green cross represents the randomly assigned direction of the detected GRB, while red cross represents the direction estimated through the algorithm.*

GRBs rate: the counts are multiplied by a factor k (eq. 4.14), that is calculated taking into account the annual rate and the number of GRBs generated in the simulation (per year, i.e. it is taken already as a rate), accordingly to a specific redshift subsample; the annual rate (K) depends on the total amount ($N_{L/S}$) of long and short events in the synthetic table (collected in 78.9 years), which are respectively 2 000 000 and 18 428, instead the number of generated GRBs in a specific redshift range ($N_{GRB,z}$) is calculated from the synthetic population (eq. 4.13).

$$K = \frac{N_{L/S}}{78.9 \text{ yr}} \quad ; \quad f = \frac{N_{GRB,z}}{N_{L/S}} \tag{4.13}$$

$$k = \frac{N_{GRB}/\text{yr}}{Kf} = \frac{N_{GRB}/\text{yr}}{N_{GRB,z}/78.9 \text{ yr}} \tag{4.14}$$

The rate increases if, instead of considering only GRBs that can be located, we also consider events detected by one and two cameras. The GRBs that can be detected and localized are $\sim 1/2$ of the events seen by any camera of the instrument.

Some simulation results regarding only long GRBs are shown in Tab. 4.4: the cameras are six and the population of synthetic long GRBs extracted is kept fixed ($N_{GRB} = 3\,000$), so by modifying the initial instrumental set up it is possible to see how the estimation of the GRB rate changes accordingly in an energy band of 100 - 150 keV, considering all redshifts.

Then, collimator height and camera angle were kept fixed at 15 cm and 45° respectively (producing an intrument FoV of 8.5 sr), in order to consider now a sample of 25 300 long GRBs at every redshift, but varying the energy bands (Tab. 4.5).

A numerical comparison with the Fermi Gamma-Ray Burst Monitor (GBM) is possible and is shown in Table 4.6. aXGIS has better performances under the main aspects that contribute to the computation of GRB annual rate: in an energy band of 50 - 300 keV, GBM can detect about 240 bursts (Connaughton et al., 2015), instead aXGIS can localize about 380 bursts. The difference between detection and localization depends on the number of cameras that detected the burst, leading to a triangulation of the event if at least three cameras have observed it. Therefore, the number of GRBs per year increases if aXGIS rate is computer for detected burst.

Table 4.4: *GRB rates at all redshifts for different camera angles and collimator heights, given a fixed population of 3000 long GRBs, in the energy band 100 - 150 keV.*

		Energy band: 100-150 keV	
$h_{collimator}(cm)$	ϑ	FoV_{aXGIS} (sr)	GRB rate (GRBs/yr)
10	35°	8.5	414
	45°	9.6	430
	55°	10.4	363
15	35°	7.4	422
	45°	8.4	363
	55°	9.3	219
20	35°	6.3	337
	45°	7.4	261
	55°	8.2	76
25	35°	5.3	295
	45°	6.4	118
	55°	7.4	0

Table 4.5: *GRB rates at all redshifts for h = 15 cm and ϑ = 45°, given a fixed population of 25300 long GRBs, for different energy bands.*

$h_{collimator}$ (cm)	ϑ	Energy band (keV)	GRB rate (GRBs/yr)
15	45°	2 - 30	79
	45°	30 - 150	179
	45°	50 - 300	384

Table 4.6: *Comparison between Fermi GBM and aXGIS GRB detection rate, estimated in the energy band 50 - 300 keV for both instruments.*

	GBM	aXGIS
Geometrical area (cm^2)	1745	2400
Scintillator length (cm)	1.27	3
Instrument FoV (sr)	~ 7	$\sim > 7$
GRB detection rate[a]	~ 240 (detected)	~ 380 (localized)

[a] energy band 50 - 300 keV.

Chapter 5

Conclusions and future perspectives

Gamma-Ray Bursts are intense bursts of high-energy photons which, in a duration of tens of seconds, outshine all other γ-ray emitters in the sky. Thanks to their luminosity, GRBs are interesting not only as high-energy events, but also as cosmological tools, since they can be used as probes for the high redshift Universe. Indeed, they allow to characterize the gas in the interstellar medium (ISM) at very high redshifts by studying the absorption lines present in the afterglow spectra. Moreover, the fading nature of GRBs and the precise localization of the afterglow allow a detailed investigation of the emission properties of the GRB host galaxy once the afterglow has vanished. GRBs therefore constitute a unique tool to understand the link between the properties of the ISM in the galaxy and the star formation activity at any redshift. Thus, GRBs are phenomena that enable the exploration of the Early Universe and, at the same time, are the cornerstone of Multi-Messenger and Time-Domain Astrophysics.

The importance of these events has pushed the High-Energy Astrophysics community to propose new mission concepts over the past decade. These missions, including HiZ-GUNDAM (JAXA), Gamow (NASA), and THESEUS (ESA), feature different payload configurations, but share similar objectives. Their goal is to take a significant step forward in the detection of events, especially those at high redshifts, surpassing all previous missions dedicated to GRBs.

Mission concepts like those above mentioned, in order to be selected and adopted by the respective space agencies, must demonstrate their effective scientific impact through their performance in detecting and characterizing a high number of GRBs.

Thus, R&D activities must be carried out in order to reach the required technological readiness of an instrument and, consequently, to increase its estimated performances. To this goal, simulations based on such instrument performances, coupled with astronomical models of GRBs, must be performed to extrapolate the scientific outcome of the adoption of an instrument within a specific payload

configuration.

The THESEUS mission concept aligns with this guideline, resulting in a very competitive mission, demonstrated by the fact that it successfully completed the ESA M5 Phase A. The subsequent selection for a further Phase A (2023 - 2026) for the ESA M7 confirms the high scientific level of the project.

In this Thesis, the case of THESEUS has been examined in details, with particular attention on the onboard high-energy monitor X/Gamma-ray Imaging Spectrometer (XGIS). The XGIS basic detection element is made by a CsI(Tl) scintillator crystal coupled to two Silicon Drift Detectors (SDDs), connected at both ends of the crystal bar. Each of these elements is a 5×5 mm^2 *pixel* of the XGIS monitor.

The combination between silicon detector and scintillator crystal offers an unprecedented capability of detecting photons with energies from soft X-rays to γ-rays (2 keV - 10 MeV). The interaction of the photons with the detector produces an electric signal, which is read by a dedicated Application Specific Integrated Circuit (ASIC) called ORION. The reading of the signal is based on the "SISWICH principle", being able to combine the information received by silicon detectors and scintillator.

For a direct detection of an X event (i.e for a soft X-ray photon), ORION must read and properly elaborate the signal coming from a single SDD. Instead, photons with energies above a few tens of keV pass through the SDD and interact within the scintillator bar. In this case the scintillation light, produced after the interaction of γ photons with CsI(Tl), is collected by both SDD simultaneously, resulting in the detection of a γ event. The ASIC readout electronics distinguishes if the interaction occurs directly in the SDD or in the scintillator, through the pulse discriminator.

An experimental characterization of XGIS detection plane has been performed in my Thesis work by doing functional, performance and environmental tests for specific requirements expected from the instrument, in order to satisfy the science objectives of THESEUS space mission. The tested requirements concerned:

- the science data production, by characterizing the ASIC (in particular the ORION Back-End);

- the energy range, producing spectral acquisitions of radioactive sources and test impulses;

- the energy resolution, by doing an analysis of the noise affecting the spectral acquisitions.

The key point about the science data production is to have digital data words in output from ORION-BE, containing the necessary information to be processed

from the software. The output data words stored include information about position (i.e. the pixels which have detected the events), timing, event type and energy. The first encountered issue regarded the correct simultaneous processing of data coming from all the pixels of the demonstration module. To tackle this problem, the redesign of the ORION-BE is necessary and has already been discussed and planned. Instead of having a multichannel Back-End, a single channel Back-End is preferred, in order to avoid glitches between the logic blocks of multiple pixels. Therefore, the data acquisitions discussed in this Thesis were taken only for Pixel 0, out of four pixels that can be managed by ORION-BE 4-channel system.

To correctly interpret and elaborate the outputs (i.e. event signals) of the prototype and to obtain energy spectra from the acquisitions, calibrations of the X and γ processors were performed. This allowed us to verify the full scale energy range of XGIS, by using test impulses of different voltage amplitudes, X and γ radioactive sources (^{55}Fe, ^{241}Am and ^{137}Cs), mimicking the arrival of high-energy photons as in the spacecraft configuration of XGIS.

For the first time, CsI(Tl) scintillator bars were introduced in the prototype, revealing the necessity of further testing the functioning of the pulse discriminator. The pulse discriminator distinguishes between X and γ events, by comparing the amplitude of the event signals with a threshold level set internally in the ASIC; the threshold has a value which is in common for both X and γ branches. However, the gain of the X branch is higher than the gain of γ branch, resulting into an incompatible value of threshold set for the latter. This lack of separate settings for the discriminator level prevent to exploit the full γ branch spectral energy range capability. In fact, by processing signals separately, the two spectra of the branch (one from γ-Top and one from γ-Bottom) have a low-energy threshold of $\sim$400 keV, instead of 20 keV as required. This results into the demonstration module for XGIS not being capable to detect soft γ-ray emission lines (e.g. the 60 keV line produced by ^{241}Am). The discriminator issue should be solved if applied to the sum of the two γ processed event signals, so further testing is ongoing.

The correct functioning of the demonstration module was verified also through an environmental test. Data acquisitions of radioactive sources were taken by varying the temperature in the operative range T = [-20, +20] °C, since XGIS is required to operate between [-15, 0] °C during the orbit. In spectra acquired at lower temperatures, a visible reduction of the FWHM was observed, reflecting into narrower spectral peaks, which also resulted in a better separation of the peaks in case of spectral doublets.

Finally, the derive energy resolution at 5.9 keV obtained with the ^{55}Fe emission line is $FWHM = (378\pm27)$ eV, which is better than the expected energy resolution of $FWHM = 1200$ eV at 6 keV. This confirms the excellent performance of energy resolution achievable with the combination of an SDD coupled with a dedicated

low-noise distributed readout electronics.

Due to the unique combination of energetic bands (from hard X-ray to soft γ-ray) and its low-noise technology, the XGIS configuration is very intriguing also for other space mission opportunities. The exploratory simulations presented in Chapter 4 shows promising results concerning GRB rate estimation capability with a configuration of six GRB monitors distributed around a common axis and tilted of a given quantity, in order to increase the FoV of the overall instrument. The foreseen configuration has moderate size and weight and is compatible with a small mission. A triangulation algorithm based on the different S/N detected by different cameras has been implemented. Although it requires further refinement for a more accurate localization capability, it showed the possibility of estimating the position of the detected bursts. A comparison with *Fermi*-GBM showed an increase of the GRB rate: aXGIS detects and localizes ~ 380 bursts per year, with respect to the ~ 240 events only detected by GBM.

Combining these localization results with other facilities can lead to scientific progress in the high-energy transient Astrophysics domain.
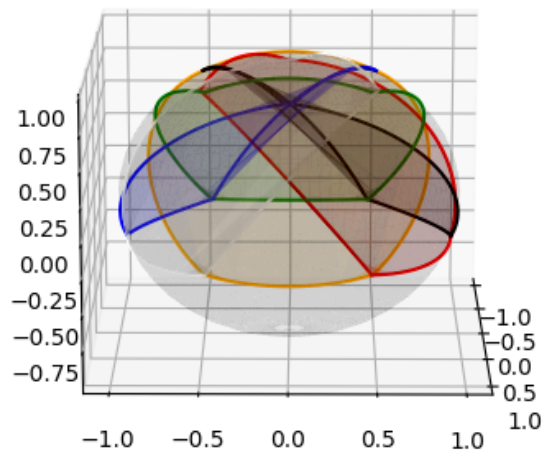
Appendix A

Plots of FoV configurations (Tab. 4.2 in Chapter 4) for different values of $h_{collimator}$ and ϑ are reported, keeping module and super-module sizes fixed.
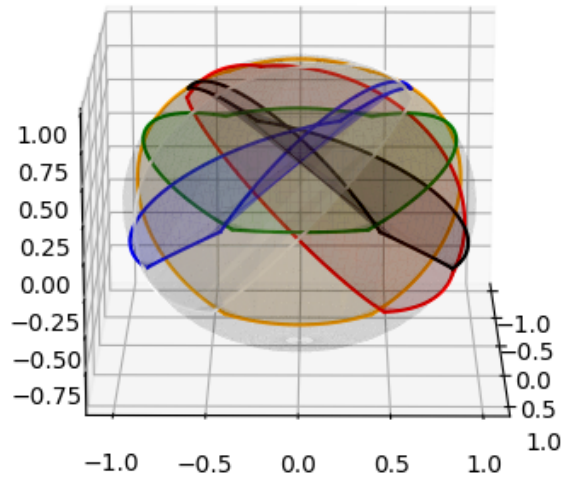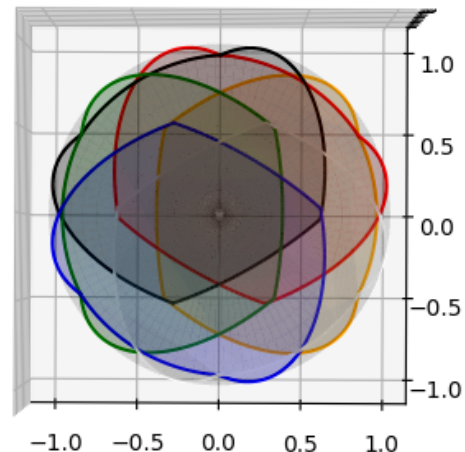

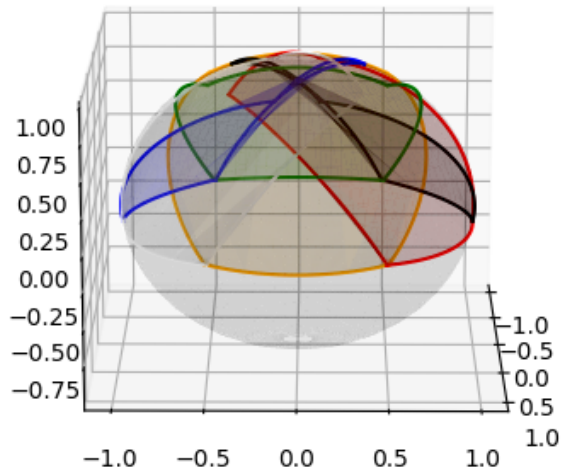**(a)** *3D model of aXGIS FoV: lateral view of configuration $h_{collimator} = 10$ cm and $\vartheta = 45°$.*
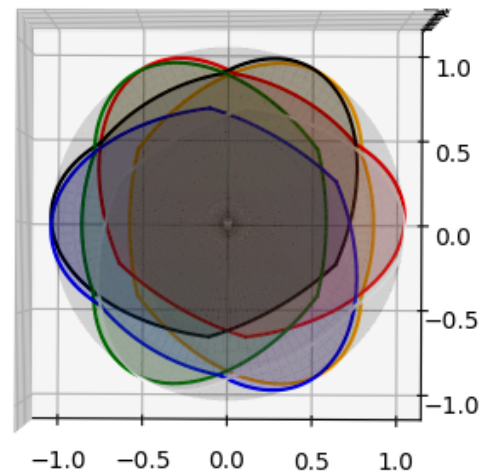
(b) *3D model of aXGIS FoV: polar view of configuration $h_{collimator} = 10$ cm and $\vartheta = 45°$.*
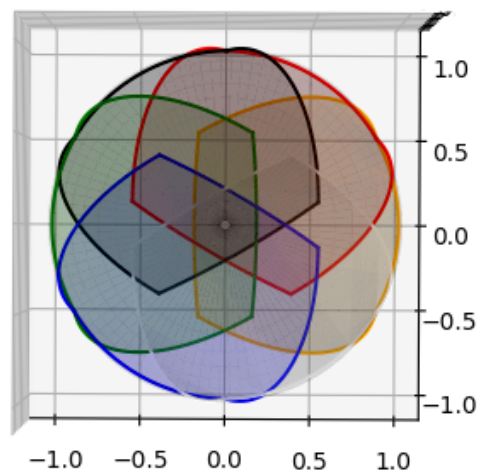

(c) *3D model of aXGIS FoV: lateral view of configuration $h_{collimator} = 15$ cm and $\vartheta = 45°$.*
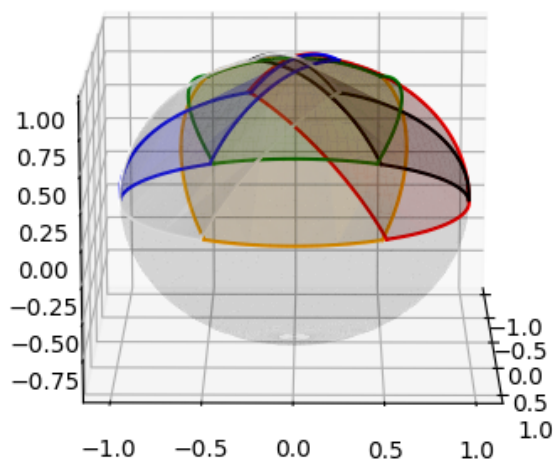

(d) *3D model of aXGIS FoV: polar view of configuration $h_{collimator} = 15$ cm and $\vartheta = 45°$.*

(e) *3D model of aXGIS FoV: lateral view of configuration $h_{collimator} = 20$ cm and $\vartheta = 45°$.*

(f) *3D model of aXGIS FoV: polar view of configuration $h_{collimator} = 20$ cm and $\vartheta = 45°$.*

(g) *3D model of aXGIS FoV: lateral view of configuration $h_{collimator} = 25$ cm and $\vartheta = 45°$.*

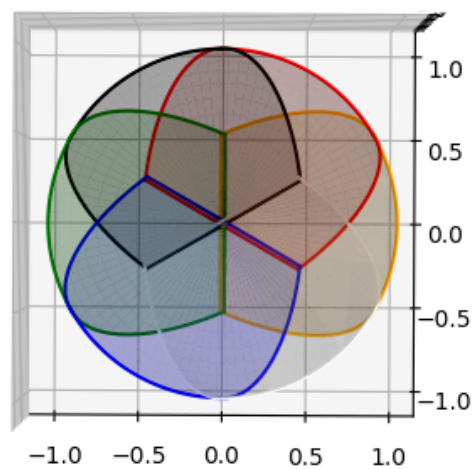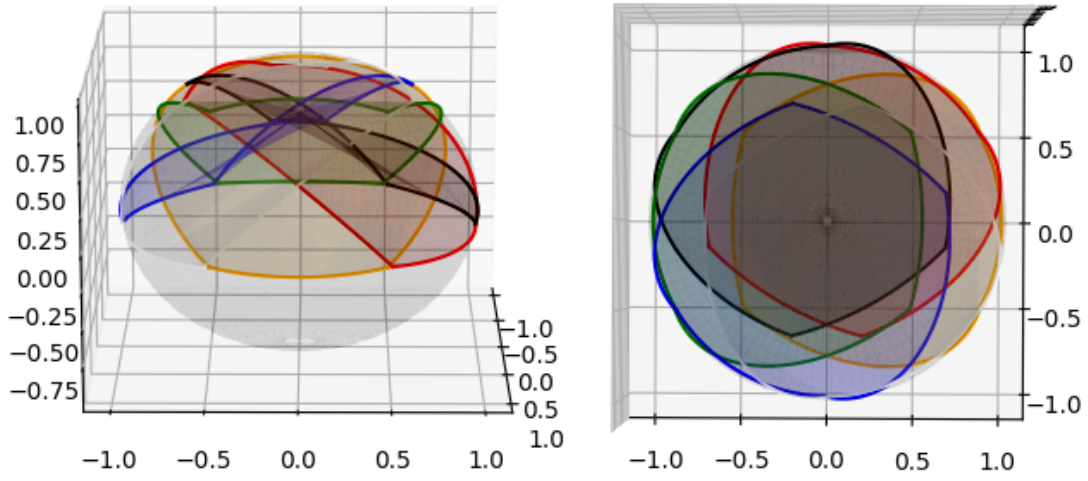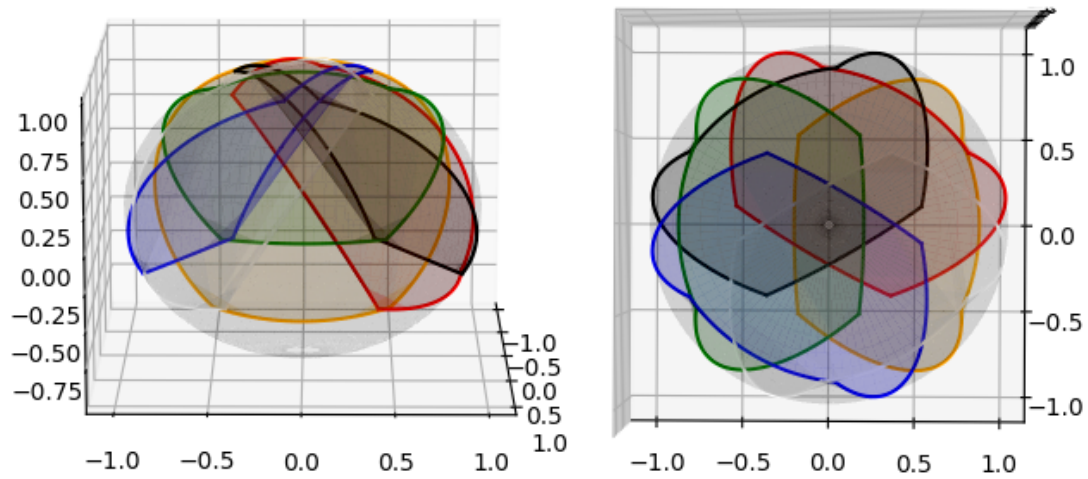**(h)** *3D model of aXGIS FoV: polar view of configuration $h_{collimator} = 25$ cm and $\vartheta = 45°$.*

(i) *3D model of aXGIS FoV: lateral view of config-* **(j)** *3D model of aXGIS FoV: polar view of*
uration $h_{collimator} = 15$ cm and $\vartheta = 35°$.   *configuration $h_{collimator} = 15$ cm and*
                                                         $\vartheta = 35°$.

(k) *3D model of aXGIS FoV: lateral view of config-* **(l)** *3D model of aXGIS FoV: polar view of*
uration $h_{collimator} = 15$ cm and $\vartheta = 55°$.   *configuration $h_{collimator} = 15$ cm and*
                                                         $\vartheta = 55°$.

Figure 5.1: *3D models of aXGIS FoV, with particular focus on each camera FoV (colored ar-*
eas). There are two plots for each configuration in Tab. 4.2, the first one shows
the lateral extension of the FoVs on the sky surface, the second one shows the ex-
tension on the common area among all cameras, viewing the sky surface from polar
direction. In collaboration with Enrico Virgilli.

Bibliography

Abbott B., et al., 2017, *Gravitational Waves and Gamma-Rays from a Binary Neutron Star Merger: GW170817 and GRB 170817A*, The Astrophysical Journal Letters

Acciari V., 2019, *Teraelectronvolt emission from the γ-ray burst GRB190114C*, Nature, 575, 455

Amati L., et al., 2002, *Intrinsic spectra and energetics of BeppoSAX Gamma-Ray Bursts with known redshifts*, Astronomy & Astrophysics

Amati L., et al., 2018, *The THESEUS Space Mission Concept: Science Case, Design and Expected Performances*, Advances in Space Research, 62, 191–244

Amati L., et al., 2021, *The THESEUS space mission: science goals, requirements and mission concept*, Experimental Astronomy, 52, 183

Ascenzi S., et al., 2021, *Electromagnetic counterparts of compact bynary mergers*, Journal of Plasma Physics, 87

Band D., et al., 1993, *BATSE observations of Gamma-ray burst spectra. I. Spectral diversity*, The Astrophysical Journal, 413, 281–292

Bloom J., et al., 2002, *The observed offset distribution of Gamma-Ray Bursts from their host galaxies: a robust clue to the nature of the progenitors*, The Astronomical Journal, 123, 1111–1148

Borciani E., 2023, *The THESEUS mission and the XGIS instrument: verification of the scientific requirements with testing of the first ORION front-end electronics prototypes.*

Castoldi A., Guazzoni C., 2012, *Sideward depletion: a novel detector family pushes the performance of the integrated front end to new hights.*, IEEE Solid-State Circuits Magazine, 4, 46–54

103

Ciolfi R., et al., 2021, *Multi-messenger astrophysics with THESEUS in the 2030s*, Experimental Astronomy, 52, 245–275

Connaughton V., et al., 2015, *Localization of Gamma-Ray Bursts using the Fermi Gamma-Ray Burst Monitor*, The Astrophysical Journal, 216, 32

Costa E., et al., 1997, *Discovery of the X-Ray Afterglow of the Gamma-Ray Burst of February 28 1997*, Nature, 387, 783

Daisuke Y., et al., 2020, *High-redshift gamma-ray burst for unraveling the Dark Ages Mission: HiZ-GUNDAM*, Proceeding of SPIE, 12444

Dilillo G., et al., 2024, *The HERMES Calibration Pipeline: MESCAL*, Astronomy & Computing

ESA-THESEUS 2021, *THESEUS Assessment Study Report (Yellow Book)*, ESA/SCI(2020)2

Fan Y., Piran T., 2008, *High energy γ-ray emission from Gamma-Ray Bursts - before GLAST*, Frontiers of Physics in China

Gatti E., Rehak P., 1984, *Semiconductor drift chamber — An application of a novel charge transport scheme*, Nuclear Instruments and Methods in Physics Research, 225, 608

Gehrels N., et al., 2009, *Gamma-Ray Bursts in the Swift Era*, Annual Review of Astronomy and Astrophysics

Ghirlanda G., et al., 2021, *Gamma-Ray Burst studies with THESEUS*, Experimental Astronomy, 52, 277

Gotz D., et al., 2021, *The Infra-Red Telescope (IRT) on board the THESEUS mission*, Proceeding of SPIE, 11444

Grassi M., Gemelli A., et al., 2022, *Experimental Characterization of the ORION ASIC: The Read-Out Circuit for X-γ-Ray Detection of the THESEUS Mission Spectrometer*, 2022 IEEE I2MTC, pp 1–6

Horstman H., et al., 1975, *The X and γ diffuse background*, Rivista del Nuovo Cimento

Iwamoto K., et al., 1998, *A hypernova model for the supernova associated with the γ-ray burst of 25 April 1998*, Nature, pp 672–674

Iyudin A., et al., 2023, *Handbook of X-ray and Gamma-ray Astrophysics - Scintillation Detectors in Gamma-Ray Astronomy*. Springer

Knoll G., 2010, *Radiation Detection and Measurement*. John Wiley & Sons, Inc.

Labanti C., et al., 2021, *The X/Gamma-ray Imaging Spectrometer (XGIS) on-board THESEUS: design, main characteristics and concept of operation*, Proceeding of SPIE, 62

Longair M., 2011, *High Energy Astrophysics*. Cambridge University Press

Lyutikov M., Blandford R., 2003, *Gamma-Ray Bursts as Electromagnetic Outflows*, doi:10.48550/arXiv.astro-ph/0312347

Macchia M., 2015, *The design of a compact and portable system for combined XRF and Raman measurements*, doi:10.13140/RG.2.1.4723.1208

Marisaldi M., Labanti C., et al., 2005, *X and gamma-ray detection with a silicon drift detector coupled to a CsI(Tl) scintillator operated with pulse shape discrimination technique*, IEEE Transactions on Nuclear Science, 52, 1842

Mele F., et al., 2021, *ORION, a Multichip Readout Electronics for Satellite Wide Energy Range X-/γ-Ray Imaging Spectroscopy: Design and Characterization of the Analog Section*, IEEE Trans. Nucl. Sci., 68, 2801

Mereghetti S., 2023, *Technical notes - Internal Report*

Mereghetti S., et al., 2021, *Time Domain Astronomy with the THESEUS Satellite*, Experimental Astronomy

Meszaros P., 2019, *Gamma-ray Bursts: Theoretical Isssues and Developments*, Astronomy & Astrophysics

Meszaros P., Rees M., 1993, *Relativistic fireballs and their impact on external matter: models for cosmological*, The Astrophysical Journal, 405, 278–284

Nicholson P., 1974, *Nuclear electronics*

O'Brien P., et al., 2021, *The Soft X-ray Imager on THESEUS: the transient high-energy survey and early universe surveyor*, Proceeding of SPIE, 11444

Orlandini M., et al., 2009, *The angular response of a rectangular mechanical collimator. The case of the HXMT collimators*, Internal Report

Perotti F., Fiorini C., 1999, *Observed energy dependence of Fano factor in silicon at hard X-ray energies*, Nuclear Instruments and Methods in Physics Research, 423, 356

Poolakkil S., et al., 2021, *The Fermi-GBM Gamma-Ray Burst Spectral Catalog: 10 yr of Data*, The Astrophysical Journal, 913, 60

Srivastava S., et al., 2023, *The XGIS instrument on-board THESEUS: Detector Principle and Read-out Electronics*, Journal of Instrumentation

Stratta G., Ciolfi R., et al., 2018, *THESEUS: A Key Space Mission Concept for Multi-Messenger Astrophysics*, Advances in Space Research, 62, 662–682

Talia M., et al., 2021, *Illuminating the Dark Side of Cosmic Star Formation Two Billion Years after the Big Bang*, The Astrophysical Journal, 909, 23

Tanvir N., et al., 2021, *Exploration of the high-redshift universe enabled by THESEUS*, Experimental Astronomy, 52, 219–244

Tsvetkova A., et al., 2021, *The Konus–Wind Catalog of Gamma-Ray Bursts with Known Redshifts. Waiting-Mode Bursts Simultaneously Detected by Swift/BAT*, The Astrophysical Journal, 908, 83

Vedrenne G., Atteia J., 2009, *Gamma-ray bursts, the brightest explosions in the Universe.* Springer

White N., et al., 2021, *The Gamow Explorer: A gamma-ray burst observatory to study the high redshift universe and enable multi-messenger astrophysics*, Proceeding of SPIE, 11821

Zhang B., et al., 2006, *Physical processes shaping Gamma-ray Burst X-ray afterglow light curves: theoretical implications from the Swift X-ray Telescope observations*, The Astrophysical Journal, 642, 354–370